MODELING CO_2 SEQUESTRATION IN DEPLETED GAS RESERVOIRS CONSIDERING THE MUTUAL SOLUBILITIES IN CO_2-HYDROCARBON GAS-BRINE SYSTEMS

by

Xinrui Zhao

A thesis submitted to the Faculty and the Board of Trustees of the Colorado School of Mines in partial fulfillment of the requirements for the degree of Doctor of Philosophy (Petroleum Engineering).

Golden, Colorado

Date _____

Signed: _____
Xinrui Zhao

Signed: _____
Dr. Yu-Shu Wu
Thesis Advisor

Golden, Colorado

Date _____

Signed: _____
Dr. Jennifer L. Miskimins
Department Head and Professor
Department of Petroleum

ABSTRACT

Over the past two decades, researchers have devoted enormous efforts into developing numerical models for CO_2 geo-sequestrations. Due to the large temporal and spatial scales associated with such processes, numerical modeling has proven to be the most effective and cost-effective to evaluate them. presently, the majority of the existing models were developed for CO_2 sequestration in saline aquifers. In contrast, the number of models for depleted gas reservoirs is relatively small, and only a fraction of them have the capability to consider geomechanical coupling or complicated natural gas compositions.

CO_2 sequestration in depleted gas reservoirs is considered a promising technique for combating global warming. The use of depleted gas reservoirs has several advantages over saline aquifers, such as the availability of existing facilities and the proven capacity and stability of gas storage. It is believed that CO_2 storage in depleted petroleum reservoirs can provide intermediate-scale storage until large-scale storage in saline aquifers becomes mature.

Here we propose an Equation of State (EOS) module for CO_2 sequestration in depleted gas reservoirs or CO_2-enhanced gas recovery. It takes into consideration the mutual solubilities in the CO_2-hydrocarbon gas-brine system based on the equality of the chemical potentials of the aqueous and non-aqueous phases. In such a way, it can properly address CO_2 dissolution into brine when hydrocarbon gas is present. Hydrocarbon gas includes methane, ethane, and propane. It employs well-recognized approaches to calculate the thermodynamic properties of the gaseous and aqueous phases. This EOS module has been applied to our in-house simulator, TOUGH2-CSM, to enable thermo-hydrological-mechanical modeling. Our research could fill the gap and provide a reference for future studies in this regard.

TABLE OF CONTENTS

LIST OF FIGURES

LIST OF TABLES

ACKNOWLEDGEMENTS

I would like to thank my supervisor, Professor Yu-Shu Wu, for bringing the weight of his considerable knowledge to this work, for the endless support and encouragement during my Ph.D. study, and most importantly, for letting me join the group.

My heartfelt gratitude also goes to the four committee members, Dr. Illangasekare, Dr. Winterfeld, Dr. Yin, and Dr. Miskimins who provide me with valuable suggestions from different perspectives.

Thanks also to my colleagues, Shihao Wang, Xiangyu Yu, Bowen Yao, Ye Tian, Chi Zhang, Jing Fu, and Jiarong Li.

Finally, I would like to give the biggest credit to my parents for their unconditional love and especially the financial support over all those years. Without them, this day would not have been possible.

NOMENCLATURE

A_{nm}	interface area for the connection between volume n and m
C_p	Heat capacity
C_s	Specific heat of solid
CSEGR	CO_2 storage and enhanced gas recovery
$\overline{D_\beta^k}$	Hydrodynamic dispersion tensor
e	Internal energy
EGR	Enhanced gas recovery
EOS	Equation of state
F_{dis}^k	Diffusive flux
h_i	Specific enthalpy
$\mathbf{i}_m^h$	Diffusive or conductive heat conduction
K_i	Thermodynamic equilibrium ratio
$k_{r\beta}$	Relative permeability
MW	Molar mass
M^k, F^k, q^k	Accumulation term, flow term, and sink/source term
P_{fc}, P_{sc}	Critical pressure for fracturing and slips
q^h	Energy-flux density
Q^h	Heat source term
r_n	Kinetic rate for chemical reactions
S_b, S_w	Solubility in brine-gas and water-gas systems

NOMENCLATURE (Cont.)

TH	Thermo-hydrological
THM	Thermo-hydrological-mechanical
u	Darcy velocity
λ_m	Apparent macroscopic thermal conductivity
λ_{i-Na},	Second-order and third-order interaction parameter for activity
μ	Dynamic viscosity
μ^*	Viscosity of gas mixture at low pressure
μ^{AQ}, μ^{NAQ}	Chemical potential of the aqueous and non-aqueous phase
γ	Activity coefficient
∇X_β^k	Concentration gradient
ω_j	Multi-porosity continuum volume fraction

CHAPTER 1

INTRODUCTION

1.1 Emission and Global Climate Change

Although the Earth has undergone climate changes in the past, the current global temperature rise is unprecedentedly rapid, largely due to human activities. As reported in 2022, the global temperature has risen by 1.60°F compared to the 20th century average of 53.6°F (Paksoy 2022). This rise is causing a range of environmental impacts, including sea ice loss, accelerated sea level rise, and extreme temperatures that leave many families living in poverty with less food and clean water. The primary cause of global climate change is the emission of CO_2, which has increased dramatically in recent decades due to the growing demand for fossil fuels. In fact, as shown in Figure 1.1, we now emit over 34 billion tons of CO_2 each year, which is five times higher than the CO_2 emission in 1950 (Kelemen et al. 2019). Approximately half of the emitted CO_2 is naturally removed by uptake in the ocean and the terrestrial biosphere, but the remainder accumulates in the atmosphere, worsening global warming. To address this issue, the Paris Agreement has recommended limiting the average warming of the atmosphere to less than 2°C, and preferably less than 1.5°C (Hoad 2015). To achieve this goal, negative emission technologies must be implemented to remove tens of Gt CO_2 per year (IPCC 2018), reduce emissions, and capture CO_2 directly from point sources, such as coal-burning power plants.

1.2 Carbon Capture, Utilization, and Storage (CCUS) Methods

Various approaches have been proposed by researchers to mitigate climate change caused by atmospheric CO_2 emissions. Some of these methods have been tested in field pilots worldwide. Terrestrial sequestration involves capturing CO_2 and storing it in soils and vegetation through photosynthesis.

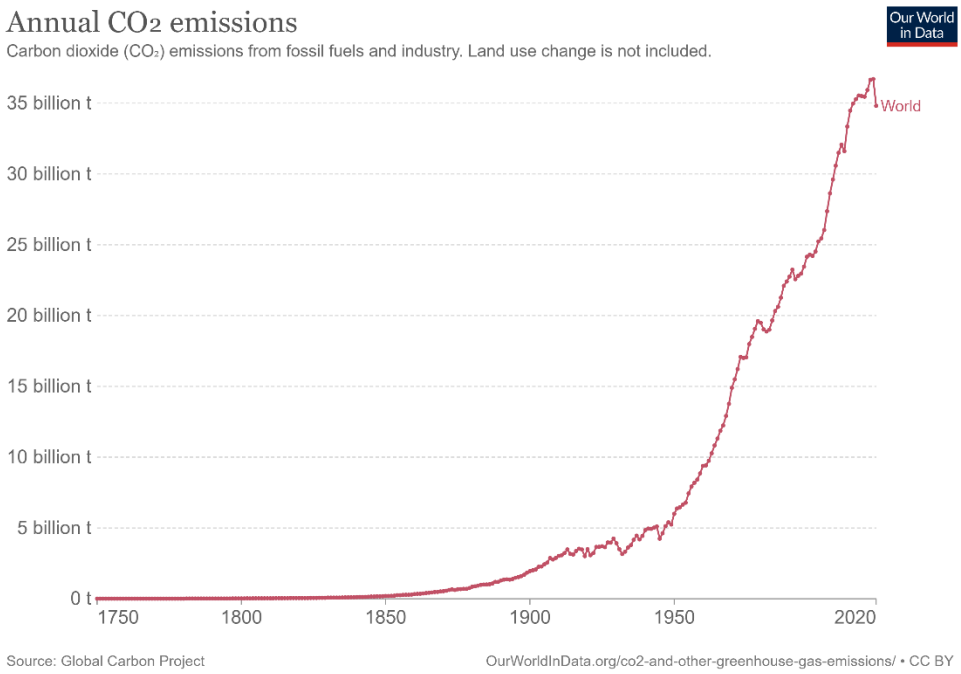

Figure 1.1 Global annual CO_2 emissions from fossil fuel and industry since 1750 (Ritchie 2022)

Ocean sequestration, which injects CO_2 into the water body, has the potential to store over 90% of current CO_2 emissions, but it is still in the research phase due to concerns about its impact on marine life. On the other hand, geological sequestration is the most promising and widely used method, which involves storing CO_2 in underground geological structures. The main storage sites include saline aquifers, depleted oil and gas reservoirs, and deep unmineable coal seams. These sites are discussed in detail below (Michael et al. 2009):

I. *Saline aquifers*: Saline aquifers are a highly effective site for CO_2 storage among all geological storage options due to their large storage capacity and global distribution. Saline aquifers are particularly advantageous as the abundance of water resources enhances the solubility trapping and mineral reactions that permanently sequester

CO_2. As a result, saline aquifers are a preferred site for large-scale CO_2 storage (Celia et al. 2015).

II. *Depleted oil and gas reservoirs*: Depleted oil and gas reservoirs are another potential site for CO_2 storage, but they may only provide intermediate-scale storage. One advantage of these reservoirs is that they have established caprocks that can trap the injected CO_2, and their characteristics are well known. Another benefit is that some of the existing infrastructure can be utilized for CO_2 injection, which can significantly reduce costs. However, it is essential to take precautions since the storage efficiency may decrease if the wells are leaky. CO_2 storage during and after enhanced oil recovery (EOR) has also become a topic of interest due to favorable economic conditions.

III. *Deep unmineable coal beds:* CO_2 has been employed to recover methane from coal seams during the enhanced coal bed methane (ECBM) recovery process. Coal beds have vast fracture networks through which gas molecules can diffuse into the matrix and desorb tightly adsorbed methane.

To assess the suitability of a storage site, important factors to consider include its storage capacity, injectivity, trapping mechanisms, and containment, as highlighted by Raza and Gholami (2019). The storage of CO_2 in saline aquifers involves several key mechanisms, including: (1) structural trapping, which occurs when CO_2 is in a mobile "gas" phase and is trapped in the geological structure of the aquifer; (2) residual gas trapping, which occurs when CO_2 becomes an immobile "gas" phase and is trapped in small pores and spaces within the aquifer; (3) solubility trapping, which involves the dissolution of CO_2 into brine to become a soluble component; and (4) mineral trapping, which involves the conversion of CO_2 into carbonate minerals through various chemical processes.

Depleted oil and gas reservoirs may have similar trapping mechanisms to saline aquifers, but they may be more complex due to the presence of oil and/or natural gas in the reservoirs. In general, the miscibility between CO_2 and crude oil should be achieved when CO_2 is stored within those oil or gas reservoirs. There may be a three-phase condition and, more likely, two phases: mixed CO_2-rich or hydrocarbon-rich fluid, and brine, once the fully miscible state between CO_2 and crude oil is achieved, or CO_2 becomes supercritical. Then, structure trapping and residual saturation trapping are related to CO_2-hydrocarbon mixing fluids. In addition, CO_2 adsorption on solids should be much stronger in oil/gas reservoirs if there is a large percentage of organic matter.

1.3 Numerical Modeling of CO_2 Geological Storage and Challenges

CO_2 storage in geological formations is a long, complex process that lasts from hundreds to millions of years. Neither laboratory studies nor short-term field tests could effectively evaluate such a process because it involves large temporal and spatial scales. Researchers developed analytical solutions (Saripalli and McGrail 2002; Gasda et al. 2009; Mathias et al. 2009) in early attempts to predict the evolution of the CO_2 plume during and after the injection. However, it is nearly impossible for those solutions to account for all the physics and chemistry associated with CO_2 storage, and they are generally limited to 1D or 2D conditions. Therefore, numerical simulation plays a significant role in the analysis, which predicts the long-term fate of the sequestrated CO_2, storage capacity, and feasibility and security of the storage sites. Mathematical modeling of CO_2 geo-sequestration must consider cross-coupling of multi-phase fluid flow, thermal effects, and geomechanics. The significance of geochemistry varies based on the composition of the rock and fluid at the geological site, hence, to analyze the long-term fate of sequestered CO_2, the storage capacity, and feasibility and security of the storage sites, a

Thermal-Hydrological-Mechanical (THM) or a Thermal-Hydrological-Mechanical-Chemical (THMC) simulator may be necessary.

Modeling CO_2 geo-sequestration requires careful consideration of phase partition, which is determined by the mutual solubilities in the fluid system. This partition is typically between aqueous and gaseous phases, or in aqueous-gaseous-liquid systems, such as in oil reservoirs. The CO_2 solubility in brine can be significant at reservoir conditions, making solubility trapping an inescapable part of storage mechanisms. The solubility of CO_2 in brine can be significant at reservoir conditions, making solubility trapping an important part of storage mechanisms. The equality of the chemical potential of aqueous and non-aqueous phases can be solved iteratively or non-iteratively with the proper equation of state and activity models (Duan and Sun 2003; Pruess and Spycher 2007). A more rigorous but computationally expensive approach involves solving multiphase chemical equilibriums using Gibbs energy minimization approaches (Leal 2020). For saline aquifers, the phase partition is relatively simple since there are only CO_2 and brine present. Many models have been developed for simulating sequestration in saline aquifers, accompanied by numerous relevant studies (e.g., Nghiem et al. 2014), Further details can be found in Chapter 2.

When compared to CO_2 storage in saline aquifers, the modeling of CO_2 storage in depleted oil and gas reservoirs is more complicated due to the existence of reservoir fluids like oil or natural gas. Although compositional models for enhanced oil and gas recovery (EOR/EGR) can offer some guidance, they often overlook the CO_2 dissolution into brine (Alfarge et al. 2017; Safi et al. 2016). CO_2 dissolution must be considered as solubility trapping is an important part of the trapping mechanisms. When modeling CO_2 storage in gas reservoirs, it is necessary to take into account the natural gas components present in the gas mixture, as the solubility of CO_2 is influenced by the gas composition. It remains a two-phase phase equilibrium

problem but needs calibration of the parameters in EOS and activity models. Many current simulators adopt the assumption that hydrocarbon gas is pure methane, as seen in studies by Ranjith et al. (2013), Afanasyev (2016), and Oldenburg et al. (2014). This approach is popular since methane typically constitutes over 92% of dry gas and the solubility of other light hydrocarbon components like ethane and propane is much lower (around 10^{-4}). Despite the low solubility of other hydrocarbon components like ethane and propane, the assumption of treating hydrocarbon gas as pure methane underestimates the gas's thermodynamic properties, particularly density, even for dry gas. Additionally, the presence of heavier components slightly affects the solubility of CO_2. Therefore, it would be beneficial to have the capacity to handle these heavier components in simulations.

Another challenge is that most existing models lack geomechanical capabilities. Reservoir and caprock stability are significant concerns in CO_2 geo-sequestration, and geomechanics provides valuable insights in this regard. In addition, geomechanical coupling can be used to address some important reservoir properties are stress-dependent, such as porosity and permeability. So far, among the commonly used simulators, CMG-GEM, ECLIPSE 300, COMET3, TOUGH2-EOS7C, and MUFITS, only the first two enable complex gas composition and geomechanics. In CMG-GEM, the storage in gas reservoirs can be modeled by developing brine as a H_2O-rich oil phase so that the solubilities can be addressed (Osseini et al. 2013). Such an assumption could be problematic if users do not calibrate the EOS parameters properly based on reliable data. ECLIPSE 300, instead, developed the GASWAT option specifically for storage in gas reservoirs, which modified the binary interaction parameters in Peng-Robinson EOS (PREOS) as suggested by Søreide and Whitson (1992), to correctly model the interaction between liquid and gas (Schlumberger 2012).

In summary, there are currently limited simulators that offer comprehensive modeling capabilities for CO_2 storage in gas reservoirs. To address this issue, an EOS module has been developed for this purpose. This module is designed to model a system consisting of CO_2, H_2O, NaCl, and up to three light hydrocarbon components, including methane, ethane, and propane. It can handle real gas mixtures, including supercritical CO_2, and is integrated into our fully coupled THM in-house simulator called TOUGH2-CSM (Winterfeld and Wu 2013).

1.4 Structure of the Dissertation

This dissertation will encompass a comprehensive review of the current state of numerical modeling for CO_2 geo-sequestration, including an exploration of technical challenges. Additionally, we will delve into the discussion of various commonly used simulators for CO_2 storage in gas reservoirs and their respective capabilities. Our EOS module methodology will be examined, covering the mutual solubility determination in the CO_2-hydrocarbon gas-brine system, phase partition, and fluid property calculations. The application of the EOS module to TOUGH2-CSM will also be detailed. We will then proceed with the model validation and verification using experimental results and TOUGH2-EOS7C. Finally, the last section of this dissertation will present a series of modeling studies and their respective results as follows:

1. THM coupled simulations;
2. CO_2 storage in a depleted gas reservoir in the Gulf of Mexico, and related injection strategy studies;
3. CSEGR in homogeneous and heterogeneous reservoirs, and related injection strategy studies.

CHAPTER 2

LITERATURE REVIEW

In this chapter, we will first discuss the status of the numerical modeling of CO_2 geo-sequestration, emphasizing the capabilities of the numerical models to handle various physical and chemical processes in a geo-sequestration system from simple to complex. Then we will focus on studies related to CO_2 sequestration in gas reservoirs.

2.1 CO_2 Migration and Thermo-Hydrological Modeling

Modeling CO_2 geo-sequestration can borrow the achievements in modeling gas injection for enhanced oil/gas recovery (EOR/EGR), in which gas (CO_2, nitrogen, flue gases) is injected into the reservoir for re-pressurization or displacement of the original fluid. Down in the reservoir, the flow of the injected gas and the pre-existing fluids are dominated by convective transport. Diffusion is usually neglected unless porous media is extremely low permeability, such as shale gas reservoirs (Zuloaga-Molero et al. 2016; Alfarge et al. 2017). Considering the large temporal scale of a CO_2 storage process and dissolution of CO_2 into the brine, diffusion should be included, giving the typical transport equation:

$$\frac{\partial}{\partial t}\left(\phi \sum_{k=1}^{P} \rho^{\beta} x_i^{\beta} S^{\beta}\right) - \sum_{k=1}^{P} \nabla\left(x_i^{\beta} u^{\beta} + S^{\beta} J_i^{\beta}\right) - q_i = 0 \tag{2.1}$$

where t is time, β is the phase index, P is the number of co-existing phases, ρ is the density, x_i^{β} denotes the mole fraction of component i in phase β, ϕ is the porosity, q is the sink/source term. Also, the second term is the combination of convection and diffusion terms, where u is the volumetric Darcy velocity and J is the molar diffusive flux that can be represented by original or modified Fick's 1st law (Alley and Alder 1979; Jaynes and Rogowski 1983; Webb and Pruess 2003). Whereas u has a relatively unified form:

$$u = -\frac{kk_{r\beta}}{\mu_\beta}\nabla(P - \rho g h) \tag{2.2}$$

where k is the absolute permeability, $k_{r\beta}$ is the relative permeability of phase β, and μ_β is the dynamic viscosity of phase β.

The multiphase flow described in Equation (2.1) is usually coupled with the thermal flow to account for non-isothermal conditions (e.g., heating/cooling due to the Joule-Thomson effect). The heat flow can generally be described by the energy conservation equation (Pruess et al. 1999):

$$\frac{\partial}{\partial t}\left(\phi S_l \rho_l e_l + \phi S_g \rho_g e_g + (1-\phi)\rho_s C_s T\right) - Q^h = -\nabla\,(q^h) \tag{2.3}$$

where l, g, and S are labels of liquid, gas, and solid phases, e is the internal energy, C_s is the specific heat of a solid, q^h is the energy-flux density, Q^h is the heat source term. q^h includes both advective and diffusive fluxes:

$$q^h = \sum_\beta \sum_i h_\beta^i q_\beta^i + \mathbf{i}_m^h \tag{2.4}$$

where h_β^i is the enthalpy of component i in phase β, and $\mathbf{i}_m^h$ is the diffusive or conductive heat conduction denoted by Fourier's law:

$$\mathbf{i}_m^h = -\lambda_m \mathbf{I}\nabla T \tag{2.5}$$

where λ_m is the apparent macroscopic thermal conductivity, and $\mathbf{I}$ is the identity matrix.

The coupled thermo-hydrological (TH) models could be used to investigate the evolution of the CO_2 plume, neglecting the chemical reactions and geomechanics. Olenburg et al. (2001) analyzed the feasibility of CO_2 sequestration with enhanced gas recovery (CSEGR) using the EOS7C module in the TOUGH2 reservoir simulator. EOS7C is a TH module dealing with the multiphase flow of water, brine, CO_2, tracer, and water at non-isothermal conditions. The study

focused on the CO_2 distribution in a 2-D vertical reservoir section initially saturated with water and CH_4. Pruess et al. (2002) presented an intercomparison of a wide range of reservoir simulators, testing their capabilities to address different physics and chemistries involved in CO_2 storage in saline aquifers, oil, and gas reservoirs. A basic agreement was found between results obtained with different simulators, but there were also some discrepancies, mainly due to differences in fluid property descriptions and space and time discretization. Though the test problems considered in this study were simplified and set to 1-D and 2-D conditions, it built the confidence in numerical modeling of CO_2 geo-sequestrations and provided a good reference for future works in this area. Class et al. (2009) performed a similar benchmark study that compared the results of different simulators on several problems related to CO_2 sequestration. They demonstrated that the results could be different for various simulators mainly due to the numerical method adopted and the physics and chemistries considered.

Lindeberg and Bergmo (2003) investigated the long-term fate of CO_2 sequestrated into a saline aquifer using commercial software, Eclipse 100. They found that the injected CO_2, due to gravity differences, migrated up-dip to the caprock and extended laterally for more than 200 years. Such a buoyancy-driven upward migration and the accumulation of the CO_2 below low-permeability layers (e.g., caprock) led to a typical gravity-override plume (Pruess and Garcia 2002; Nordbotten et al. 2005; Zhou et al. 2008). This means the thickness of the CO_2 plume decreases with the radial distance from the injection well. As a result, the dissolution of CO_2 into brine is expected to occur at the CO_2/brine interface, increasing the brine density by 1% (Pruess et al. 2002). The density difference allows the CO_2-rich brine to sink and the brine with no CO_2 to migrate upward and dissolve more CO_2. Such a process plays a vital role in CO_2 storage in saline aquifers and determines the injectivity and storage capacity (solubility trapping), which thus needs to be treated with care in numerical modeling. CO_2 dissolution into the brine, because

of the high dissolution rate, is usually assumed to be in thermodynamic equilibrium. Therefore, it was estimated using simple approaches that count in the effect of brine salinity in the first place. Pruess and Garcia (2002) employed an extended Henry's law to model CO_2 dissolution in brine with a fugacity correction. Long et al. (2004) described the dissolution behavior as the equality of fugacity in gas and aqueous phases:

$$f_{ig} = f_{iw}, i = 1, \dots, N_g \tag{2.6}$$

where f_{ig} and f_{iw} is the fugacity of component i in the gas phase and aqueous phase, respectively, and N_g denotes the number of the coexisting components in the gas phase. f_{ig} can be calculated using PREOS (Collins et al. 1992), and f_{iw} using Henry's law, where Henry's law constants were modified using the Scaled Particle Theory (Li and Long 1986).

Spycher and Pruess (2005) developed a more accurate and efficient solubility model, which was later applied to ECO2N, a fluid property model for the TOUGH2 code (Pruess and Spycher 2007). Thomas et al. (2012) summarized the available CO_2 solubility models based on the equality of fugacity and the methods to estimate the fugacities of gaseous and aqueous CO_2. The main problem of these methods is the simplification of the aqueous phase, where only water, CO_2, and one or two salts (usually NaCl and $CaCl_2$) are considered. In addition, it is also neglected that the solubility of CO_2 may also be impacted by the existence of ionic species induced by the dissociation of dissolved CO_2, such as CO_3^{2-} and HCO_3^-. These problems can typically be addressed by adopting multiphase chemical equilibrium models based on Gibbs energy minimization approaches (Zaydullin et al. 2014; Lucia et al. 2015; Leal et al. 2016, 2019). In addition, the solubility of CO_2 in brine and the dissolution rate are impacted by many other factors such as aquifer tilt angle, formation thickness, heterogeneity in permeability, and the number of layers (Silva et al. 2015), making predictions considerably difficult. The CO_2

dissolution into brine becomes less dominant in oil/gas reservoirs because the porous space is mainly occupied by hydrocarbons (assuming no bottom water is presented). However, due to the existence of residual or irreducible water, an appropriate estimation of the CO_2 solubility is still demanded.

Thermo-hydrological-mechanical (THM) process is essential for fluid flow in the reservoir and within the injection wells, which was usually overlooked in many simulations. The CO_2 flowing in the injection wells may be subject to several thermophysical activities, such as phase change, fractional loss, thermal conduction, convection, and Joule-Thomson heating and cooling (Oldenburg 2007; Han et al. 2010). In addition, CO_2 thermophysical properties may change dramatically in the wellbore. Therefore, the CO_2 in the wellbore should be represented by transient flow rather than steady-state flow (Lu and Connell 2008; Li et al. 2015). Therefore, a wellbore/reservoir flow coupling is preferred for adequate modeling of CO_2 injection (Pan et al. 2014; Rasmusson et al. 2015; Liu et al. 2016; Hoteit et al. 2019; Raad et al. 2021).

2.2 Caprock Stability and Hydromechanical Modeling

Hydromechanical (HM) or Thermo-hydrological-mechanical (THM) processes are critical in CO_2 sequestration, particularly during CO_2 injection. Injection of CO_2 pressurizes the targe geological site, which may trigger unwanted formation and caprock deformations, such as induced fracture and shear slip on preexisting faults (Credoz et al. 2009; Shukla et al. 2010; Smith et al. 2013). The deformation depends on the change in the stress state, thermal and mechanical properties of the geologic formation, and the fault frictional properties, which are usually intuitively unobvious (Vilarrasa et al. 2014; Wang et al. 2016). Thus, it should be analyzed using geomechanical models.

Geomechanical models can either be fully coupled or sequentially coupled (or partially coupled) with hydrological models (Chen and Gutierrez et al. 2001; Mainguy and Longuemare

2002; Jeannin et al. 2007). The majority of the fully coupled models rely on the fully implicit finite difference method, which solves coupled nonlinear equations simultaneously, using the Newton-Raphson scheme. This method is unconditionally stable and guarantees convergence if the mathematical problem is well-posed (Kim et al. 2011a), but large-scale simulations could become computationally expensive. Sequential couplings of TH or THM processes are easier to implement by linking different simulators, which provides more flexibility (Mainguy and Longuemare 2002; Jha and Juanes 2014). The design of robust and efficient sequential approaches to HM couplings has a long history and shows appropriate stability (Armero and Simo 1992; Mainguy and Longuemare 2002; Tran et al. 2005), or even unconditional stability (Kim et al. 2011b, 2011c, 2013; Jha and Juanes 2014)

Using HM or THM couplings allows us to analyze the formation and caprock stabilities and determine the pressure margins for CO_2 injection. Some early studies regarding caprock stability associated with CO_2 injection were carried out at Lawrence Berkeley National Laboratory (LBNL) using THM-coupled computer codes TOUGH2-FLAC^{3D}. In their early simulations (Rutqvist and Tsang 2002; Rutqvist et al. 2007), a conservative assumption was used to obtain the critical pressure for fracturing, which is that the fracture is induced once fluid pressure exceeds the minimum principal stress:

$$P_{fc} = -\sigma_3 \tag{2.7}$$

In analogy, the critical pressure for a slip to occur can be written as:

$$P_{sc} = -\sigma_{m2} + S_0 \, cot\varphi - \frac{|\tau_{m2}|}{sin\varphi} \tag{2.8}$$

where S_0 is the faults coefficient of internal cohesion, and φ is the angle of internal friction. Also, τ_{m2} and σ_{m2} are the two-dimensional maximum shear stress and mean stress in the plane σ_1 and σ_2, respectively, denoted as:

$$\tau_{m2} = \frac{1}{2}(\sigma_1 - \sigma_3) \tag{2.9}$$

$$\sigma_{m2} = \frac{1}{2}(\sigma_1 + \sigma_3) \tag{2.10}$$

These simulations used the assumption of linear poroelastic and isotropic properties. This reasonable assumption has been widely adopted to represent the mechanical rock properties and rock fluid interactions (Shemin and Garven 1992; Zimmerman 2000; Pandey et al. 2018; Raziperchikolaee and Mishara 2020). However, irreversible strains may also present due to the significant pressure build-up during CO_2 sequestration and the small yield stress of most of the rocks. Therefore, elastoplastic or viscoplastic rather than poroelastic models generally yield more precise results (Settari et al. 1999). Vilarrasa et al. (2010) adopted the viscoplastic constitutive model in their coupled HM modeling study of CO_2 sequestration in deep saline aquifers. They retained the conservative assumption for hydraulic fracturing but predicted the onset of shear slip based on the Drucker-Prager yield function (Desai 1980).

Isotropic plastic and anisotropic elastoplastic constitutive models were used in a series of simulation studies regarding fault reactivation due to CO_2 injection (Rutqvist et al. 2008; Cappa and Rutqvist 2011a, 2011b). Both models were proved appropriate to represent fault hydromechanical behaviors in their studies. The anisotropic elastoplastic model, in which the reservoir rock is considered elastic and the fault follows an elastoplastic behavior, is more physically reasonable. Whereas isotropic plasticity has the advantage of simplicity. Jha and Juanes (2014) proposed another approach to determine the fault pressure, considering that the fluid pressures are different on two sides of the fault, leading to a discontinuity in the effective stress across the fault. In their approach, the fault pressure was expressed by the maximum of the equivalent multiphase pressures on the positive (P_+) and negative side (P_-) of the fault:

$$P_{fc} = \max(p_-, p_+) \tag{2.11}$$

They applied this theory to their coupled HM model to study the realistic fault constitutive behavior subjected to CO_2 sequestration into saline aquifers. Recently, there has been an emerging interest in applying the extended finite element method (X-FEM) to coupled THM problems (Wang et al. 2009; Lei et al. 2015; Miah et al. 2015; Cheng et al. 2022). This is because x-FEM could effectively handle the fracture discontinuity, and in such a method, the fracture morphology is independent of the mesh grid (Cheng et al. 2022). Thus, this method could give a more realistic representation of fracture/dimensions and improve computing efficiency (Wang et al. 2020).

THM modeling provides the capability to predict the potential safety issues during CO_2 sequestration but also in hydraulic and mechanical properties concerning the change in the stress field. The in-situ stress is expected to change significantly during high-pressure CO_2 injection and the following fluid migration. The change could alter some critical parameters for fluid flow, such as porosity, permeability, and capillary pressure. The change in these parameters could usually be estimated by correlating them directly or indirectly to mean stress (Winterfeld and Wu 2012). For example, porosity is a function of the mean stress, and permeability changes with porosity (Rutqvist et al. 2002). This allows THM modeling to obtain a more accurate prediction of CO_2 migration and long-term fate compared with TH modeling.

2.3 Geochemistry and Reactive Transport Modeling

The last section focused on the THM processes involved in CO_2 sequestrations, where the role of chemical reactions is less pronounced. However, chemical processes are of the same level of importance as other processes. The chemical reactions in CO_2 sequestration can be

summarized in chronological order. First, injected CO_2 dissolved into the brine to form some aqueous species, such as $CO_{2,aq}$, $H_2CO_{3,aq}$, CO_3^{2-}, and HCO_3^- (Fang et al. 2010):

$$CO_2\ (g) \longrightarrow CO_2\ (aq) \tag{2.12}$$

$$CO_2\ (aq) + H_2O\ (l) \rightleftharpoons H_2CO_3\ (aq) \tag{2.13}$$

$$H_2CO_3\ (aq) \rightleftharpoons H^+ + HCO_3^- \rightleftharpoons 2H^+ + CO_3^{2-} \tag{2.14}$$

Then, the cations in the brine, such as Ca^{2+} and Mg^{2+} interact with CO_3^{2-} to precipitate carbonate minerals, such as limestone and dolomite. These are the fundamentals of mineral tripping, which sequestrates CO_2 permanently in the subsurface environment (Bachu et al. 1994). On the other hand, mineral dissolution may occur at the same time depending on the composition of the formation rock. Common minerals that dissolve in the acidic solution include calcite, kaolinite, illite, and dolomite (Silva et al. 2015).

The dissolution of gas/supercritical CO_2 in brine is relatively fast, for example, the rate is around 6.3×10^{-3} mol m^{-2} s^{-1} in seawater (Shindo et al. 1995). As mentioned above, though it is a kinetic process, it is usually assumed to be in thermodynamic equilibrium in numerical modeling. In contrast, the dissolution/precipitation of the minerals is much slower, taking hundreds to tens of thousands of years to complete, which should be represented by geochemical kinetics (Balashov et al. 2013). The most commonly used kinetic law in the geochemical modeling of CO_2 geosequestration is a simplified law from Lasaga et al. (1994):

$$r_n = f(c_1, c_2, \dots, c_{Nc}) = \pm k_n A_n \left|1 - \Omega_n^{\theta}\right|^{\eta} \qquad n = 1, \dots, N_q \tag{2.15}$$

where r_n is the kinetic rate, where positive and negative r_n demonstrate precipitation and dissolution, respectively, k_n is the rate constant, A_n is the specific reactive surface per kg H_2O, Ω_n is the kinetic mineral saturation ratio. N_c and N_q denotes the number of primary chemical

species number of minerals at kinetic conditions, respectively. θ and η are usually set to one or determined based on experimental data (Chou et al. 1989). The kinetic rate constant k, considering neutral, acid, and base mechanisms ($\mathrm{n}, \mathrm{H}^{+}, \mathrm{OH}^{-}$) can be expressed as (Lasaga et al. 1994; Palandri and Kharaka 2004):

$$k = k_{25}^{n} \exp\left[\frac{E_{\alpha}^{n}}{R}\left(\frac{1}{T} - \frac{1}{298.15}\right)\right] + k_{25}^{H^{+}} \exp\left[\frac{E_{\alpha}^{H^{+}}}{R}\left(\frac{1}{T} - \frac{1}{298.15}\right)\right] a_{H+}^{n_{H+}} + k_{25}^{n} \exp\left[\frac{E_{\alpha}^{OH-}}{R}\left(\frac{1}{T} - \frac{1}{298.15}\right)\right] a_{OH-}^{n_{OH-}} \quad (2.16)$$

where E_a is the activation energy, k_{25} is the rate constant at 25℃, R is the universal gas constant, T is the absolute temperature, $a_{H+}^{n_{H+}}$ and $a_{OH-}^{n_{OH-}}$ are the activity of H^{+} and OH^{-}, respectively.

Xu et al. (2003) simulated CO_2 sequestration in deep arenaceous formations using a non-isothermal reactive geochemical transport code, TOUGHREACT. They illustrated that CO_2 was sequestrated through the precipitation of minerals such as dolomite, calcite, and siderite, and the precipitation of the secondary minerals was controlled by the rock composition and corresponding kinetic reaction rates. Xu et al. (2004) dug deeper into CO_2 sequestration through mineral precipitation, which considered the importance of redox processes and the porosity change due to mineral dissolution/precipitation. Their results illustrated that the amount of CO_2 immobilized by mineral trapping could be comparable with that by solubility trapping under favorable conditions. In addition, the precipitation of carbonates reduced the porosity significantly, affecting the permeability and fluid flow in the reservoir. Zerai et al. (2006) simulated the mineral trapping of disposed of CO_2 in Rose Run sandstone, Ohio, focusing on equilibrium and kinetic modeling. It demonstrated that the brine-to-rock ratio, the PH, the fugacity of CO_2, and the dissolution rate were significant factors in determining the stability of the carbonate rock. These studies neglected the base mechanism because the brine was generally assumed to be acidic due to CO_2 dissolution.

Xu et al. (2007) investigated the impact of injected composition, including pure CO_2, CO_2-H_2S, and CO_2-SO_2 mixtures, on the mineral trapping of CO_2. They found out that the properties of the acidified zone varied with injected gas, and significant quantities of CO_2 were trapped through the precipitation of Ankerite, dawsonite, and siderite. In addition, porosity changes were noticed in all simulations due to mineral dissolution and precipitation. Cantucci et al. (2009) performed geochemical modeling of CO_2 storage in the Weyburn reservoir using the PHREEQC software package with modifications to the thermodynamic database and fugacity of supercritical CO_2. The results indicated that CO_2 could be sequestrated by solubility trapping and mineral trapping via dawsonite precipitation. Balashov et al. (2013) investigated the impacts of geochemical kinetics on CO_2 sequestration in saline sandstone reservoirs with a diffusion transport model. In their simulation, mineral trapping became important after 200 years after CO_2 diffusion was initiated due to smectite dissolution and calcite precipitation. Calcite precipitation counted for 30% of the storage capacity when reaching maximum storage.

Zheng et al. (2012), Zheng et al. (2013), and Zheng and Spycher (2017) used reactive transport models and batch simulations to predict the changes in shallow groundwater chemistry in response to CO_2/brine leakage. Such risk analyses are required before the large-scale deployment of CO_2 geological sequestration. The above studies mainly aimed at CO_2 sequestration into saline aquifers, which mostly considered gas-aqueous-rock interactions in slightly heterogeneous reservoirs. For CO_2 storage in gas/oil reservoirs, the complexity rises significantly due to the existence of a hydrocarbon mixture and more servere reservoir heterogeneity. So far, only a very few models can simulate geochemical processes counting in the equilibrium phase behavior of complex hydrocarbon mixture and strong reservoir heterogeneity (e.g., Flemisch et al. 2011; Voskov et al. 2016).

The geochemical calculations of these problems generally involve uncertainties raised from thermodynamic and kinetic databases, the choice of primary and secondary minerals, and the corrections of equilibrium constants concerning temperature and pressure. Dethlefsen et al., 2012 analyzed the uncertainties associated with the thermodynamic database (PHREEQC and SUPCRT92) and selected secondary mineral assemblage. Their results showed that varying the thermodynamic database could cause a 61% difference in CO_2 sequestrated, and the choice of secondary mineral assemblage could lead to a difference of up to 74%. In addition, the correction of equilibrium constants regarding pressure influenced 11%.

Haase et al. (2013) performed an uncertainty study by comparing the computed results from EQ3/6, PHREEQC, and FactSage/ChemApp. From their results, the CO_2 fugacity was the most sensitive parameter, affecting calcite dissolution. Balashov et al. (2013) performed sensitivity tests to identify minerals that could impact the geochemical evolution of storage in a baseline reservoir and indicated the sensitivity of CO_2 sequestration to rate constants of minerals such as oligoclase albite and smectite varied in magnitude. There were also uncertainties concerning CO_2 solubility models, as we described above. Handling these uncertainties remains a challenging task at present due to limited experimental and field data.

Another challenging task is to develop coupled THMC simulators, which can handle all important physics and chemistries involved in CO_2 geo-sequestration. So far, only a few simulators can handle complex THMC processes associated with CO_2 geosequestration, which are generally achieved by linking reactive transport simulators to geomechanical models using sequential approaches. For example, Taron et al. (2009) coupled TOUGHREACT with the mechanical framework of $FLAC^{3D}$ to simulate THMC interactions in deformable, fractured porous media. Zhang et al. (2015) proposed a sequentially coupled THMC simulator for CO_2 geo-sequestration, taking advantage of the capabilities of TOUGHREACT and TOUGH2-CSM.

2.4 CO_2 Sequestration in Depleted Gas Reservoir

As mentioned above, CO_2 storage in depleted gas and oil reservoirs can provide intermediate-scale storage. Bourg et al. (2015) stated that the potential storage capacity of saline aquifer is around 1000 to 10000 Giga tonnes, whereas that of gas and oil reservoirs is up to 900 Giga tonnes. Depleted gas reservoirs were proven stable to store hydrocarbon gases, making them promising sites for CO_2 storage with minimum environmental impact (Gupta 2010). From an economic standpoint, these reservoirs were often well understood through well logs, seismic, or core analysis before exploitation, which saves the cost associated with reservoir characterizations. One can also take advantage of the existing infrastructures, such as wells and pipelines. The production wells can be turned into CO_2 injectors with little expense, and pipelines can even be directly used.

During the exploitation, the reservoir pressure decreases as continuously producing gas. It may cause some water invasion from the bottom aquifer, but the majority of the reservoir remains occupied by gas. The remaining gas is very compressible, providing a large potential to sequester CO_2. Over the years, CSEGR has attracted increasing attention, which injects CO_2 to displace remaining CO_2 after depletion. The CO_2 injection usually ceases once CO_2 breaks through, to avoid the costly sweetening processes for separating the mixture of CO_2 and hydrocarbon gas. At this point, the CO_2 that remained in the reservoir was sequestered. CSEGR provides limited CO_2 storage since it does not pressurize the reservoir as sheer CO_2 storage (from now on, we will use sheer CO_2 storage to represent storage not aiming at EGR) does. But it further cuts down the expenses by producing natural gas. While CO_2-enhanced oil recovery (EOR) is a well-established practice, CO_2 EGR has yet to be tested in the field (Khan et al. 2012). So far, either sheer storage or storage through EGR has been mostly studied numerically via simulations.

Oldenburg et al. (2004) developed a TOUGH2 module, EOS7C, for CO_2 storage in gas reservoirs. Such a module can handle mutual solubilities in the CO_2-CH_4-brine system and thermodynamic properties of real gas mixtures. Rebscher et al. (2006) investigate the feasibility of CSEGR in Altmark natural gas reservoirs using TOUGH2-EOS7C. They found that CO_2 breakthrough early due to high permeability layers and recommend using gel treatment for conformance control. Zhang et al. (2007) developed a system-level model to analyze CO_2 geo-sequestration from geological, economic, and environmental aspects. Ennis-King et al. (2011) provided a history matching of TOUGH2-EOS7C to field data for CO_2 storage in the Naylor gas reservoir in Australia. Through the history matching, it demonstrated that such CO_2 storage was modeled accurately by numerical simulation. There were also a few attempts that used TOUGH2-EOS7C to study the effect of injection strategies on the storage capacity and enhanced methane recovery (Fan et al. 2021; Liu et al. 2022).

ECLIPSE 300^{TM}'s GASWAT mode was developed specifically for CO_2 storage or CSEGR (Schlumberger 2012). In the GASWAT option, the binary interaction coefficients for PREOS were modified based on Søreide and Whitson (1992) to handle gas-brine problems. ECLIPSE is a compositional simulator that handles up to 8 components (N_2, CO_2, C_1, C_2, C_3, iC_4, C_5, iC_5) and it can also be used for coupled geomechanical modeling. Polak and Grimstad (2009) investigated the feasibility of CSEGR and long-term storage in Atzbach-Schwanenstadt natural gas field, and the results demonstrated that CSEGR is not beneficial due to CO_2 early breakthrough, and long-term storage may encounter CO_2 leakage if CO_2 reached the abandon wells. Shi and Durucan (2009) used ECLIPSE 300 to study the hydromechanical response of the reservoir and cap rock with respect to the production and CO_2 injection and analyzed the possible shear failure and reactivation of the faults in the same gas field in Austria. Gao et al. (2021) did similar studies in Sarah CO_2 storage site, by linking ECLIPSE 300 and FLAC^{3D}.

Another commercial software, CMG-GEM has also been commonly used for CO_2 storage in gas reservoirs. Narinesingh and Alexander (2014) investigated the impact of injection pressure on condensate recovery and CO_2 storage. They found out that high injection pressure could improve the storage capacity by hysteresis. Zhang et al. (2021) looked into using CO_2 as cushion gas for CSEGR and demonstrated injecting CO_2 from the bottom layer can prevent the escaping of working gas, thus improving the CO_2 storage. They also stated that a high production rate could help withdraw more natural gas. Omar et al. (2021) used CMG-GEM to test a new CO_2 injection scheme, which injects CO_2 along with brine to retard breakthrough.

COMET3 is a reservoir simulator for shale oil, shale gas, and coalbed methane, so it is often used for CSEGR in shale gas reservoirs. There have been also some in-house simulators designed for CO_2 storage in gas reservoirs, such as MUFITS (Afanasyev 2016), but their capabilities are usually depicted vaguely in the published data, perhaps for confidentiality reasons. For this reason, they will not be discussed here. Among the four simulators discussed above, only the two commercial software have relatively complete capability of modeling CO_2 storage in gas reservoirs. The other two can only handle simple composition and are not equipped with geomechanical options.

CHAPTER 3

METHODOLOGY AND APPROACH

In this chapter, the methodology and approaches will be introduced for the EOS module, including:

1. Thermodynamic equilibrium in CO_2-hydrocarbon gas-brine system
2. Phase partition
3. Implementation to TOUGH2-CSM and thermodynamic properties

3.1 Thermodynamic Equilibrium in the CO_2-Hydrocarbon Gas-Brine System

The mutual solubility is determined by solving the thermodynamic equilibrium between the non-aqueous phase and the aqueous phase which dissolves CO_2 and some hydrocarbon components (here methane, ethane, and propane). The equilibrium constant of the gas species and water are calculated using different correlation as given in the following content.

3.1.1 Equilibrium Constant of Gas Species

For the system to reach thermodynamic equilibrium, the chemical potential of each component in the aqueous (AQ) and non-aqueous (NAQ) phases should be equal. For the non-aqueous phase, the chemical potential of the components is given by,

$$\mu^{NAQ}(T,P) = \mu^{0}_{NAQ}(T,P) + RTln(f) \tag{3.1}$$

where T is temperature, P is pressure, u is chemical potential, μ^0 is the chemical potential at the reference pressure, R is the universal gas constant, and f is the fugacity written as,

$$f = P\phi y \tag{3.2}$$

where P is total pressure, ϕ is the fugacity coefficient, and y is the mole fraction of each component in the non-aqueous phase.

The chemical potential of the aqueous components, instead, can be written in the form of activity, a, as,

$$\mu^{AQ}(T,P) = \mu^{0}_{AQ}(T,P) + RTln(a) \tag{3.3}$$

By equating two chemical potentials we can derive the final equation for dissolved gas,

$$P\phi y = k_H \gamma x \tag{3.4}$$

where x is the mole fraction of the component in the AQ phase, k_H is Henry's constant, ϕ is the fugacity coefficient, and γ is the activity coefficient.

The intermediate steps can be found in Ziabakhsh-Ganji and Kooi (2012). For each gas component, except water, we have

$$(P\phi_i y_i)_{NAQ} = (k_{Hi}\gamma_i x_i)_{AQ} \tag{3.5}$$

and

$$K_i = \frac{y_i}{x_i} = \frac{k_{Hi}\gamma_i}{P\phi_i} \tag{3.6}$$

where the subscript *i* is the index of the gas species, and K_i is the thermodynamic equilibrium ratio. ϕ_i need to be derived utilizing some equation of state (EOS) that describe PVT or PVT-X properties of brine and gas mixture. Here we use PREOS because of simplicity and credibility. Some virial-like EOS such as Duan and Sun (2003) could also be applied. PREOS is written regarding the compressibility factor Z as,

$$Z^3 - (1-B)Z^2 + (A - 2B - 3B^2)Z - (AB - B^2 - B^3) = 0 \tag{3.7}$$

where parameters *A* and *B* are a function of pressure and temperature and can be obtained from

$$A = \frac{aP}{R^2T^2} \tag{3.8}$$

$$B = \frac{bP}{RT} \tag{3.9}$$

For mixtures, PREOS employs the following mixing rule by Zudekevitch and Joffe (1970),

$$a = \sum_{i=1}^{nc}\sum_{j=1}^{nc} x_i x_j \sqrt{a_i a_j}\left(1 - \delta_{ij}^{BIC}\right) \tag{3.10}$$

$$b = \sum_{i=1}^{nc} x_i b_i \tag{3.11}$$

where δ_{ij}^{BIC} is the binary interaction parameters and the other parameters are calculated as,

$$a_i = \frac{\Omega_a R^2 T_{ci}^2}{P_{ci}}\left[1 + \kappa_i\left(1 - \sqrt{\left(\frac{T}{T_{ci}}\right)}\right)\right]^2 \tag{3.12}$$

$$b_i = \frac{\Omega_b R T_{ci}}{P_{ci}} \tag{3.13}$$

$$\kappa_i = 0.37464 + 1.54226\omega_i - 0.26992\omega_i^2 \tag{3.14}$$

Note that by assuming infinite dilution, the above mole fraction of water equals zero, which eliminates the need for iteration. Once we determine Z from Equation (3.17) following the approach described by Danesh (1998), we are able to obtain the ϕ_i as,

$$\begin{aligned} ln\phi_i = {} & \frac{b_i}{b}(Z-1) - ln(Z-B) \\ & - \frac{A}{2\sqrt{2}B} \times \left(\frac{2\sum_j^{nc} x_i a_{ij}}{a} - \frac{b_i}{b}\right) \times ln\left(\frac{Z + \left(\sqrt{2}+1\right)B}{Z - \left(\sqrt{2}-1\right)B}\right) \end{aligned} \tag{3.15}$$

The activity coefficients of the dissolved gases are calculated using the approach proposed by Ziabakhsh-Ganji and Kooi (2012). The brine salinity is considered by counting in the reduction of the activity coefficient due to interaction with solutes,

$$ln\,\gamma_i = \sum_c 2m_c\lambda_{i-Na} + \sum_c 2m_a\lambda_{i-Cl} + \sum_c\sum_a 2m_a\xi_{i-Na-Cl} \tag{3.16}$$

where m_c and m_a are molalities of anion and cation, λ_{i-Na} is the second-order interaction parameter, $\xi_{i-Na-Cl}$ is the third interaction parameter, and i is the index of gas species. λ_{i-Cl} is assumed zero here. λ_{i-Na} and $\xi_{i-Na-Cl}$ are obtained using the following correlation,

$$\begin{aligned}\lambda_{i-Na}\ or\ \xi_{i-Na-Cl} \\ = C_1 + C_2T + \frac{C_3}{T} + C_4P + \frac{C_5}{P} + \frac{C_6P}{T} + C_7\frac{T}{P^2} + \frac{C_8P}{630-T} \\ + C_9T\,ln\,P + \frac{c_{10}P}{T^2}\end{aligned} \tag{3.17}$$

where P is in bar, T is in K, and C_1 to C_{10} are fitting parameters.

Henry's constant k_{H_i} of the dissolved gas species are attained using the correlation by Akinfiev and Diamond (2003), which assumes infinite dilution of the dissolved gas species,

$$ln\left(k_{H_i}\right) = (1-\eta_i)\,ln\,f^0_{H_2O} + \eta_i\,ln\left(\frac{RT}{Mw}\rho^0_{H_2O}\right) + 2\rho^0_{H_2O}\Delta B \tag{3.18}$$

$$\Delta B = \tau + \Gamma p + \beta\sqrt{\frac{10^3}{T}} \tag{3.19}$$

where η_i is a constant for each dissolved gas species, T is the temperature in K, and $f^0_{H_2O}$ and $\rho^0_{H_2O}$ are fugacity and density of pure water. In Equation (3.19), τ, Γ, β are fitting parameters. These parameters and second-order and third-order C_1 to C_{10} in Equation (3.17) need to be calibrated with experimental data so that the equilibrium can be calculated. We adopted the calibrated parameters for CO_2 and methane in Ziabakhsh-Ganji and Kooi (2012), with minor changes. Those for ethane and propane were calibrated based upon collected experimental data, as shown in

Table 3.1.

Calibrations of parameters in Equation (3.19) requires solubility data in the water-gas system, or experimentally measured Henry's constant. For parameters in Equation (3.17), it requires solubility data in the brine-gas system such that the salting-out effect can be taken into account. Non-linear least squares fitting method was used to fit these parameters. Note the solubility data in the brine-gas system for propane are very rare in the published data. With this concern, the data was generated using the approach in Søreide and Whitson (1992). They produced data using solubilities in pure water and Seconow salting-out coefficients,

$$S_b = S_w \times 10^{-k_s C_{sw}} \tag{3.20}$$

where S_b and S_w are solubilities in brine and pure water, k_s is the salting-out factor, and C_{sw} the salinity in molality. k_s relates to the normal boiling point of the gas species, T_{bi} and temperature, T,

$$k_{si} = 0.13163 + 4.45 \times 10^{-4} T_{bi} - 7.692 \times 10^{-4} T + 2.6614 \times 10^{-6} T^2 - 2.612 \times 10^{-9} T^3 \tag{3.21}$$

Using this method, the solubility data of propane for the brine-gas system were obtained. Table 3.2 and Table 3.3 summarize the second-order and third-order interaction parameters. Table 3.4 gives the calibrated parameters for Henry's constant calculations. The standard deviation of the fitting can be found in the last column in Table 3.1

Table 3.1 Geometry of the base case for reservoir simulation

	NaCl Molality (mol/kg)	T(K)	P(bar)	Standard dev (%)
Ethane				
Errington et al. (1998)	0	300-570	0.2-65.18	4.21
Rettich et al. (1981)	0	275-323	0.75	3.75
Crovetto et al. (1982)	0	295-429.05	10	6.94
Kobayashi and Catz (1953)	0	310.93-444.25	10	13.46
Clever et al. (1970)	0	303.15	1	1.75
Wu et al. (1985)	0	298.15	1	4.36
Narasimhan et al. (1981)	0	293.15-303.15	1	2.72
Taft et al. (1951)	0	293.15-303.15	1	11.84
Eucken and Hertzberg (1950)	0.01-2.95	273-293	1	8.44
Mishnina et al. (1961)	0.505-6.193	288.15-348.15	1	18.88
Ben-Naim et al. (1974)	1.0	283.15-328.15	1	2.97
Czerski and Czaplinski (1962)	0.311-3.484	273.15	1-25	6.20
Propane				
Chapoy et al. (2004)	0	277.62-368.16	3.57-39.15	17.41
Battino (1983)	0	273.15-348.15	1	2.45
Wen and Hung (1970)	0	278.15-308.15	1	5.48
Kresheck et al. (1965)	0	274.15-328.15	1	3.83
Wishnia (1963)	0	288.15-308.15	1	8.53
Morrison and Billett (1952)	0	285.45-347.25	1	1.24
Generated data	0-10	273.15-450.0	0-500	12.15

Table 3.2 Calibrated second-order interaction parameters for activity coefficient

Constant	λ_{CO_2-Na}	λ_{CH_4-Na}	$\lambda_{C_2H_6-Na}$	$\lambda_{C_3H_8-Na}$
C_1	-0.0652869	-5.7066455E-1	-0.84689	-0.82823
C_2	1.6790636E-4	7.2997588E-4	1.317E-3	1.749E-3
C_3	40.838951	01.5176903E2	1.53115E2	1.53396E2
C_4	0	3.1927112E-5	0	0
C_5	0	0	1.290223	0.221646
C_6	-3.926652E-2	-1.6426510E-5	1.3155E-2	-13.5881
C_7	0	0	-1.27E-2	-4.6E-4
C_8	2.1157167E-2	0	-1.289E-2	1.67558
C_9	6.5486487E-6	0	0	1
C_{10}	0	0	3.3631E-2	4.2079E3

Table 3.3 Calibrated third-order interaction parameters for activity coefficient

Constant	λ_{CO_2-Na}	λ_{CH_4-Na}	$\lambda_{C_2H_6-Na}$	$\lambda_{C_3H_8-Na}$
C_1	-1.144624E-2	-2.9990084E-3	5.24667E-3	-8.9919E-3
C_2	2.8274958E-5	0	0	0
C_3	0	0	0	0
C_4	0	0	0	0
C_5	0	0	0	0
C_6	1.3980876E-2	0	0	0
C_7	0	0	0	0
C_8	-1.43491E-2	0	0	0
C_9	0	0	0	0
C_{10}	0	0	0	0

Table 3.4 Calibrated parameters in Henry's constant

Gas species	η	τ	β	Γ
CO_2	-0.114535	-5.279063	6.187967	0
CH_4	-0.092248	-5.779280	7.262730	0
C_2H_6	-0.939566	-11.84746	12.98532	0
C_3H_8	-0.838790	-10.17948	11.77503	0

3.1.2 Equilibrium Constant of Water

The equilibrium constant of H_2O (K_{H2O}) is calculated differently, using the relation proposed by Spycher et al. (2003),

$$K_{H_2O} = \frac{y_{H_2O}}{x_{H_2O}} = \frac{K^0_{H_2O}}{f^0_{H_2O}P} exp\left[\frac{(P-1) * MW_{H_2O}}{RT}\right] \tag{3.22}$$

where MW_{H2O} is the molar mass of H_2O, and $K^0_{H_2O}$ is the equilibrium constant at the reference pressure of 1 bar which is obtained from,

$$log\left(K^0_{H_2O}\right) = -2.209 + 3.097 \times 10^{-2}\theta - 1.098 \times 10^{-4}\theta^2 + 2.048 \times 10^{-7}\theta^3 \tag{3.23}$$

where θ is the temperature in ℃.

$f^0_{H_2O}$ is calculated using the relation of King et al. (1992) instead of PREOS as the latter is not efficiently accurate,

$$f^0_{H_2O} = P_s\, exp\left[\frac{(P-P_s)v}{RT}\right] \tag{3.24}$$

where P_s is the saturation pressure and v is the molar volume. The corresponding relations for these two parameters are given as follows,

$$ln\left(\frac{P_s}{P_c}\right) = \frac{T_c}{T}[a_1\tau + a_2\tau^2 + a_3\tau^3 + a_4\tau^{3.5} + a_5\tau^4 + a_6\tau^{7.5}] \tag{3.25}$$

where $\tau = 1 - \frac{T}{T_c}$, T_c and P_c are water critical temperature and pressure, a_1 to a_6 are fitting parameters, which can be found in Shibue (2003).

$$v = Mw_{H2O} \times V \tag{3.26}$$

$$V = \frac{V^0 - V^0 P}{B + A_1 P + A_2 P^2} \tag{3.27}$$

$$\begin{aligned} V^0 = (1 + 18.159725 \times 10^{-3}\theta)/(0.999 + 18.224 \times 10^{-3}\theta \\ - 7.922 \times 10^{-6}\theta^2 - 55.448 \times 10^{-9}\theta^3 + 149.76 \times 10^{-12}\theta^4 \\ - 393.3 \times 10^{-15}\theta^5) \end{aligned} \tag{3.28}$$

$$B = 19654.32 + 147.037\theta - 2.21554\theta^2 + 1.048 \times 10^{-2}\theta^3 - 2.28 \times 10^{-5}\theta^4 \tag{3.29}$$

$$A_1 = 3.29 - 2.39 \times 10^{-3}\theta + 2.84 \times 10^{-4}\theta^2 - 2.82 \times 10^{-6}\theta^3 + 8.48 \times 10^{-9}\theta^4 \tag{3.30}$$

$$A_2 = 6.245 \times 10^{-5} - 3.913 \times 10^{-6}\theta - 3.499 \times 10^{-8}\theta^2 + 7.942 \times 10^{-10}\theta^3 - 3.299 \times 10^{-12}\theta^4 \tag{3.31}$$

where V is the reciprocal of the density of pure water and θ is the temperature in ℃. These relations are also used to calculate the density of pure water.

3.2 Phase Partition and Mutual Solubility

Once obtaining the equilibrium constants, we need to determine the phase partition between non-aqueous and aqueous phases and the mutual solubilities. These terms are of great importance for fluid flow calculations in the simulation. Taking the CO_2-CH_4-Brine system as an example, following the steps in section 3.1, we have,

$$K_i = \frac{y_i}{x_i}, \quad i = \mathrm{H_2O}, \mathrm{CO_2}, \mathrm{CH_4} \tag{3.32}$$

Based on material conservation and equimolar constraint, we also have,

$$n_v y_i + n_l x_i = Z_i, \quad i = \mathrm{H_2O}, \mathrm{CO_2}, \mathrm{CH_4} \tag{3.33}$$

$$n_v + n_l = 1 \tag{3.34}$$

where Z_i is the mole fraction of each species (or feed) in the entire system (including both non-aqueous and aqueous phases) and n_v and n_l are the phase mole fractions of non-aqueous and aqueous phases, respectively. The parameters that need to be obtained are the composition of

each phase (x_i and y_i) and n_v and n_l. We use the Rachford-Rice equation to iteratively solve for n^v,

$$\sum_{i=1}^{N} \frac{Z_i(K_i - 1)}{1 + (K_i - 1)n^v} = 0, \qquad i = \mathrm{H_2O}, \mathrm{CO_2}, \mathrm{CH_4} \tag{3.35}$$

With the known value of n^v, K_i, and Z_i, the mole fraction of each phase is subsequently obtained from,

$$x_i = \frac{Z_i}{1 + (K_i - 1)n^v} \tag{3.36}$$

$$y_i = \frac{K_i Z_i}{1 + (K_i - 1)n^v} \tag{3.37}$$

Shabani and Vilcaez (2017) proposed a different approach to attain x_i and y_i. Instead of solving Rachford-Rice equation, this approach is non-iterative, in which the fraction of $\mathrm{H_2O}$ in the gas phase (y_{H_2O}) is obtained from,

$$y_{H_2O} = \frac{1 - \sum \frac{y_i}{K_i}}{\frac{1}{K_{H_2O}} - \sum \frac{y_i}{K_i}}, \quad i = \mathrm{CO_2} \text{ and } \mathrm{CH_4} \tag{3.38}$$

which is close to the method proposed by Spycher et al. (2003) for the solubility of CO_2 in brine. Here y_i is the initial mole fraction of the gas species in the gas phase, which assumes infinite dilution of water. After that, we can use y_{H_2O} to correct y_i using the following normalization equation,

$$y_i^n = \frac{y_i}{1 + y_{H_2O}}, \quad i = \mathrm{CO_2} \text{ and } \mathrm{CH_4} \tag{3.39}$$

where y_i^n is the normalized mole fractions of $\mathrm{CO_2}$ and $\mathrm{CH_4}$ in the gas phase. Then the mole fraction of each species in the aqueous phase can be calculated from,

$$x_{H_2O} = \frac{y_{H_2O}}{K_{H_2O}} \tag{3.40}$$

$$x_i^n = \frac{y_i^n}{K_i} \tag{3.41}$$

This model is not very rigorous since it does not take material balance into account. But it is simple, computationally cheap, and predicts mutual solubilities perfectly fine. As shown in Figure 3.1, the solubilities of the three species predicted by iterative and non-iterative models are very close at 50% CO_2; 50% CH_4; 100 ℃. We further compared their predictions under various temperatures, compositions, and salt molalities, and the results showed that the difference between the two models was usually less than 1%. Nevertheless, the calculations of n^v and n^l in this method need special care.

With x_i and y_i determined, we have 4 equations that can be used to calculate n_v and n_l. In such cases, n_v and n_l have no unique solutions. To avoid violating material conservations, we solve for n_v and n_l using Equation (3.33) (i=1 for water) and Equation (3.34) and then correct y_{CO_2} and y_{CH_4} based on Equation (3.33) (i=2, 3). The reason for correcting y_{CO_2} and y_{CH_4} instead of x_{CO_2} and x_{CH_4} is that xs are relatively small and thus more sensitive to corrections. Another reason is that x_{CO_2} and x_{CH_4} play an important role to decide phase conditions in the non-iterative approach, which will be discussed in detail later.

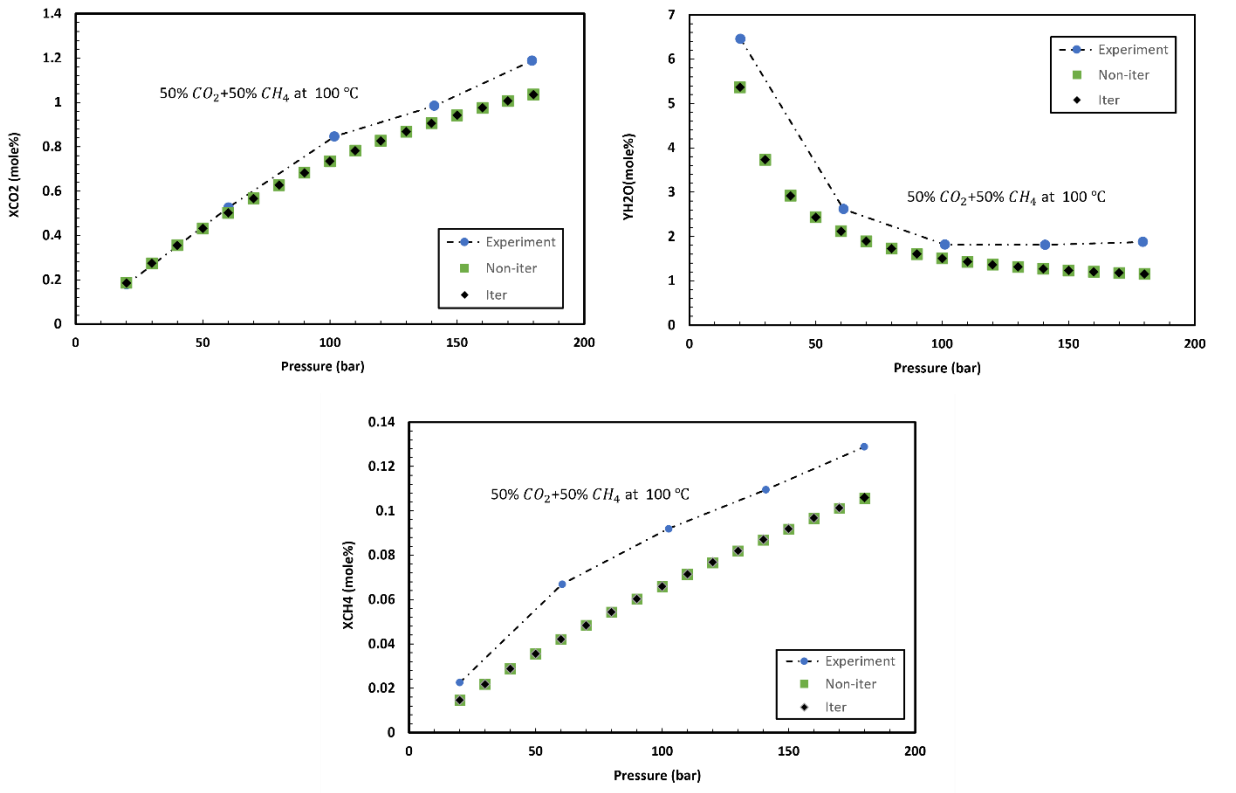

Figure 3.1 Mutual solubility prediction for brine-CO_2-CH_4 system using both non-iterative and iterative models at 50% CO_2, 50% CH_4, and 100℃

3.3 Nesting TOUGH2-CSM and the EOS Module

This section will introduce the incorporation of this EOS module into TOUGH2-CSM from the following aspects:

1. Governing equation and solution method
2. Capability of the EOS module
3. Phase partition and composition
4. Thermodynamic properties

3.3.1 Governing Equation and Solution Method

TOUGH2-CSM is a fully coupled THM simulator, which solves fluid and heat flow and geomechanics in a fully implicit manner. The governing equations are given as follows.

3.3.1.1 Mass Conservation

The mass conservation equation can be expressed as follows:

$$\frac{d}{dt}M^k = -\nabla \cdot F^k + q^k \tag{3.42}$$

where M^k, F^k, and q^k denote the accumulation term, flow term, and sink/source term, respectively, and k is the index for each component. The accumulation term can be expressed as:

$$M^k = \phi \sum_{\beta} S_\beta \, \rho_\beta x_\beta^k \tag{3.43}$$

where ϕ is the porosity, β is the phase index, and S_β, ρ_β are saturation and density of phase β. x_β^k is the mass fraction of component k (water, NaCl, CO_2, C_1, C_2, and C_3) in phase β. The flow term sums up the advective mass flux (F_{adv}^k) and diffusion ($F_{\beta,dis}^k$) and hydrodynamic dispersion term (F_{dis}^k). F_{adv}^k can be expressed as:

$$F_{adv}^k = \sum_{\beta} x_\beta^k F_\beta \tag{3.44}$$

in which F_β, the mass flux of phase β can be described by multiphase Darcy's law:

$$F_\beta = -k\left(\frac{k_{r\beta}\rho_\beta}{\mu_\beta}\right)(\nabla p_\beta - \rho_\beta g) \tag{3.45}$$

where k is the absolute permeability, $k_{r\beta}$ is the relative permeability of phase β, ∇p_β is the pressure gradient for phase β (summation of the reference phase pressure and capillary pressure), and g is the acceleration of gravity. $F_{\beta,dis}^k$ is given below:

$$F_{\beta,dis}^{k} = -\phi\tau_0\tau_\beta\rho_\beta d_\beta^k \nabla x_\beta^k \tag{3.46}$$

where d_β^k is the diffusion coefficient for component k in phase β, $\tau_0\tau_\beta$ combined is the tortuosity, in which τ_0 represents the tortuosity of the porous medium and the latter depends on saturation. F_{dis}^{k} is given as follows:

$$F_{dis}^{k} = \sum_{\beta} \rho_\beta \overline{D_\beta^k}\ \nabla x_\beta^k \tag{3.47}$$

where $\overline{D_\beta^k}$ is the hydrodynamic dispersion tensor and ∇X_β^k is the concentration gradient of component k in phase β.

3.3.1.2 Energy Conservation

The energy conservation equation can also be described by Equation (3.42), but the accumulation term sums up internal energies. It is the equation after NK (number of components) mass balance equations, so the accumulation term should be denoted as M^{NK+1}, which can be expressed as:

$$M^{NK+1} = (1-\phi)\rho_R C_R T + \phi \sum_{\beta} S_\beta \rho_\beta u_\beta \tag{3.48}$$

where subscript R and β represent properties of rock and fluid, respectively, and u_β denotes the specific internal energy of each phase. The heat flux F^{NK+1} considers both conduction and convection:

$$F^{NK+1} = -\lambda_T \nabla T + \sum_{\beta} h_\beta F_\beta \tag{3.49}$$

in which λ_T is the thermal conductivity and h_β is the specific enthalpy of phase β.

3.3.1.3 Momentum Balance

Finally, the geomechanical equations are based on Hooke's law extended to non-isothermal multi-porosity media. The first equation is based on Hooke's law for a thermo-multi-poroelastic media, relating volumetric strain to mean stress:

$$K\epsilon_v = \tau_m - \sum_j \left(\alpha_j P_j + 3\beta K \omega_j \left(T_j - T_{ref}\right)\right) \tag{3.50}$$

where *K* is the bulk modulus, ϵ_v is the volumetric strain, $\tau_m$is the mean stress, subscript *j* refers to different continua such as fracture and matrix, α is the Biot coefficient, β is the linear thermal expansion coefficient, ω is the multi-porosity continuum volume fraction, and T_{ref} is the reference temperature. The other equation refers to momentum conservation, which relates mean stress, pore pressure, temperature, and body force:

$$\nabla \cdot \{\frac{3(1-v)}{1+v}\nabla\tau_m + \overrightarrow{F_b} - \frac{2(1-2v)}{1+v}\nabla[\sum_j (\alpha_j P_j + 3\beta K \omega_j T_j)]\} = 0 \tag{3.51}$$

where v is Poisson's ratio and $\overrightarrow{F_b}$ is the body force. More detail about the governing geomechanical equations for TOUGH2-CSM can be found in Winterfeld and Wu (2016).

3.3.1.4 Equations in integral form

In TOUGH2-CSM, these equations are integrated within the arbitrary representative elementary volume using the integral finite difference method, The mass conservation equation can be expressed as:

$$\frac{dM_n^k}{dt} = -\frac{1}{V_n}\sum_m A_{nm}F_{nm}^k + q_n^k \tag{3.52}$$

where M_n^k is the average mass of component k over representative elementary volume, V_n. A_{nm} is the interface area for the connection between volume n and m, F_{nm} denotes the mass flux

between two volumes, and q_n is the sink/source term. The discretized advective flux and diffusive flux are given as follows:

$$F_{\beta,nm,adv} = -k_{nm}\left(\frac{k_{r\beta}\rho_\beta}{\mu_\beta}\right)_{nm}\left[\frac{p_{\beta,n}-p_{\beta,m}}{D_{nm}} - \rho_{\beta,nm}g_{nm}\right] \tag{3.53}$$

$$F^k_{\beta,nm,dis} = -\sum_\beta\left(\phi\tau_0\tau_\beta\rho_\beta d^k_\beta\right)_{nm}\left[\frac{\left(x^k_\beta\right)_m - \left(x^k_\beta\right)}{D_{nm}}\right] \tag{3.54}$$

where subscript nm denotes the averaging, often harmonic and upstream weighting, of the properties at the interface between element n and m. D_{nm} sums up the distances from the element central point to the interfaces, or more specifically, $D_{nm} = \frac{D_n+D_m}{2}$. For energy conservation equation:

$$\frac{dU_n}{dt} = \frac{1}{V_n}\sum_m A_{nm}F_{nm} + q_{h,n} \tag{3.55}$$

$$F_{nm} = -\lambda_{nm}\left(\frac{T_n - T_m}{D_{nm}}\right) + \sum_\beta h_{\beta,nm}F_{\beta,nm} \tag{3.56}$$

The means stress equation can be expressed as a surface integral over surface segments:

$$\sum_m\left[\frac{3(1-v)}{1+v}\nabla\tau_{nm} - \frac{2(1-2v)}{1+v}(\alpha\nabla p_{nm} + 3\beta K\nabla T_{nm}) + \overline{F_{nm}}\right]A_{nm} = 0 \tag{3.57}$$

To solve these equations simultaneously, these equations are written in a residual form. Then an equation system with NEL×NEQ equations is solved using Newton's method. NEL refers to the number of elements and NEQ denotes the number of equations required for each element (*NK*+2 for THM modeling).

3.3.2 The capability of the EOS module and parameter choices.

The EOS module considers up to 6 components, water, NaCl, CO_2, C_1, C_2, and C_3. There are three phases, aqueous, non-aqueous, and solid phase. The solid phase, if exists, contains only NaCl, which means mineral reactions are excluded. Since TOUGH2-CSM is a THM simulator, the simulation runs may also include heat transfer and geomechanics. For those runs, the number of equations is 8 (6 mass conservations, an energy balance, and a momentum balance). Note in our EOS module, we only consider the non-aqueous phase as a gas-like fluid (subcritical gas, or supercritical gas-like fluid). High-pressure liquid-like fluid is not considered (e.g. more than 1000 bar).

A summary of the components and primary variable choices is provided in Table 3.5. As we consider the water dissolution into the gas phase, the water might be carried by the gas flow, causing salt precipitation. To account for such conditions, we follow the convention of ECO2N (Pruess 2005), of which the second primary variable refers to salt (NaCl here) mass fraction (X_{sm}) in the water-salt system, or solid saturation (S_s) plus 10 if the solid phase presents. In this way, the salt concentration is independent of the CO_2 amount, and the solid saturation can be properly addressed. The first primary variable is the pressure and the other four primary variables for mass conservation are the mass fraction of CO_2, C_1, C_2, and C_3. The module aims at simulating CO_2 storage in gas reservoirs and CSEGR. The general workflow of TOUGH2-CSM is given in Figure 3.2.

Table 3.5 Summary of the EOS

Components		
	#1: Water #2: NaCl #3: CO_2 #4: CH_4	#5: C_2H_6 #6: C_3H_8
Parameter choices		
(NK, NEQ, NPH, NB) =		(6, 8, 3, 6) 4 components, non-isothermal, geomechanical (6, 8, 3, 6) 4 components, isothermal, geomechanical
Primary variables		
P	Pressure (pa)	
X_{sm}	The salt mass fraction in the water-salt system, or S_s+10 when solid salt presents	
Z_{2m}	Mass fraction of CO_2	
Z_{3m}	Mass fraction of CH_4	
Z_{4m}	Mass fraction of C_2H_6	
Z_{5m}	Mass fraction of C_3H_8	
T	Temperature (℃)	
Stress	Mean stress (pa)	

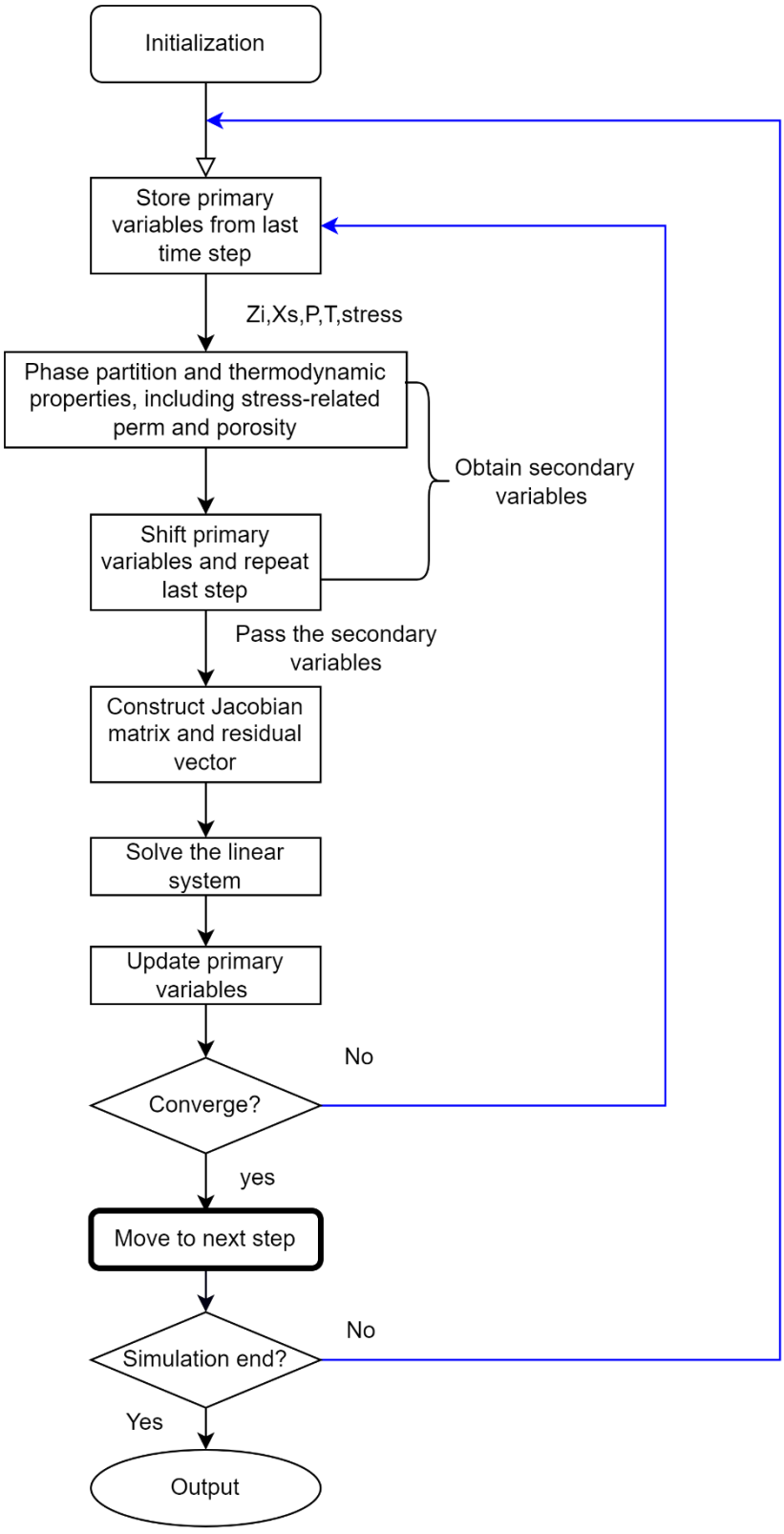

Figure 3.2 Flow chart of a typical simulation run

3.3.3 Phase Condition and Composition

The phase condition and composition in the EOS module can be obtained utilizing Rachford-Rice equation or a non-iterative approach. Details of both approaches are discussed in detail in the following content.

3.3.3.1 Iterative approach

The determination of phase condition and composition in the iterative approach is very straightforward. By utilizing the Rachford-Rice equation, the phase composition and saturation can be obtained simultaneously once equilibrium ratios are calculated. Before this, the salt concentration and the presence of a solid phase need to be carefully checked using the approach by Pruess (2005). In their approach, the equilibrium solubility of NaCl (X_{seq}) can be estimated as a function of temperature. Then NaCl mass fraction in water-NaCl system, $X_{sm,}$ and solid saturation, S_s can be examined following the rule shown in Figure 3.3. Note that X_s is the salt concentration used to calculate the thermal dynamic equilibrium between aqueous and non-aqueous phases. If X_{sm} exceeds X_{seq}, we set X_s equal to X_{seq} and provide an initial guess to S_s, which is a small amount (ZERO=10^{-5}). Also, if solid salt is already present, we need to check whether it disappears (whether X_{sm}<10.0).

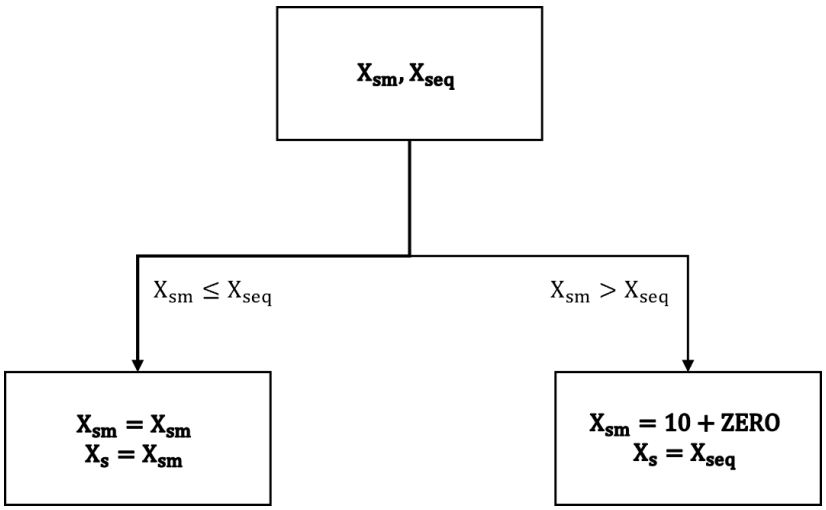

Figure 3.3 Scheme for examining salt concentration and solid phase presence.

Once X_s is decided, we can calculate the equilibrium constants as described in section 3.1.1. Note that the primary variables 3 to 6 should be converted to mole fractions before being used for equilibrium calculations. In addition, the salt concentration should be converted to molality for calculating the activity coefficient,

$$X_s = \frac{m\, M_{NaCl}}{1000 + m\, M_{NaCl}} \Rightarrow m = \frac{1000 X_s / M_{NaCl}}{1 - X_s} \tag{3.58}$$

where m is the molality of NaCl, which is defined as moles per 1000 g of water, and M_{NaCl} is the molecular weight/molar mass of NaCl (55.448 g/mole). Then phase mole fraction and phase composition can be obtained with the help of the Rachford-Rice equation as shown in Figure 3.4. From here, for clarity, subscripts i = 1 to 5 refer to H_2O, CO_2, C_1, C_2, and C_3 respectively. Next, these mole fractions may be converted to mass fractions (x_{im}, y_{im}):

$$x_{im} = \frac{x_i MW_i}{\sum_i x_i MW_i} \tag{3.59}$$

$$y_{im} = \frac{y_i MW_i}{\sum_i x_i MW_i} \tag{3.60}$$

where MW_i is the molar mass of component i. The phase mole fractions need to be transformed into phase saturations (S_g, S_l) for fluid flow calculations and some properties, such as relative permeability. They are computed based on the molar densities (md_l, md_g):

$$md_l = \frac{\rho_l}{\sum_i x_i MW_i} \tag{3.61}$$

$$md_g = \frac{\rho_g}{\sum_i y_i MW_i} \tag{3.62}$$

where ρ_l and ρ_g are the liquid density and gas density in kg/m^3, respectively, and the calculation of the density will be provided later with that of other thermodynamic properties. Note x_i and MW_i for the aqueous phase are corrected with respect to the dissolved NaCl. S_g and S_l are calculated as:

$$S_l = \frac{\frac{1-n^v}{md_l}}{\frac{1-n^v}{md_l} + \frac{n^v}{md_g}}(1 - S_s) \tag{3.63}$$

$$S_g = \frac{\frac{n^v}{md_g}}{\frac{1-n^v}{md_l} + \frac{n^v}{md_g}}(1 - S_s) \tag{3.64}$$

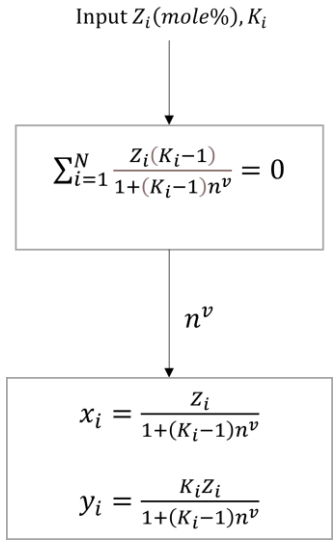

Figure 3.4 Workflow of calculation of phase mole fraction and composition based on the Rachford-Rice equation

3.3.3.2 Non-iterative approach

The determination of the phase choice and composition for the non-iterative approach is comparatively complex. Rather than computing n^v by solving the Rachford-Rice equation directly, the phase condition in the non-iterative approach is determined based upon the equilibrium solubilities in mass fraction (denoted as x_{im} and y_{im}). For example, for a system that considers water, CO_2, and C_1, the workflow is given in Figure 3.5. Z_2 and Z_3 are the 3rd and 4th primary variables, and Z_1 is the overall mass fraction of water, excluding dissolved NaCl:

$$Z_1 = (1 - Z_2 - Z_3) \times (1 - X_s) \tag{3.65}$$

If Z_1 is less than the equilibrium water solubility in the gas mixture, the system falls into single phase gas condition. If Z_2 and Z_3 are both less than the equilibrium solubility of CO_2 and C_1 in an aqueous solution, it is a single liquid condition. If none of the above conditions are satisfied, it means the aqueous and gas phase coexist.

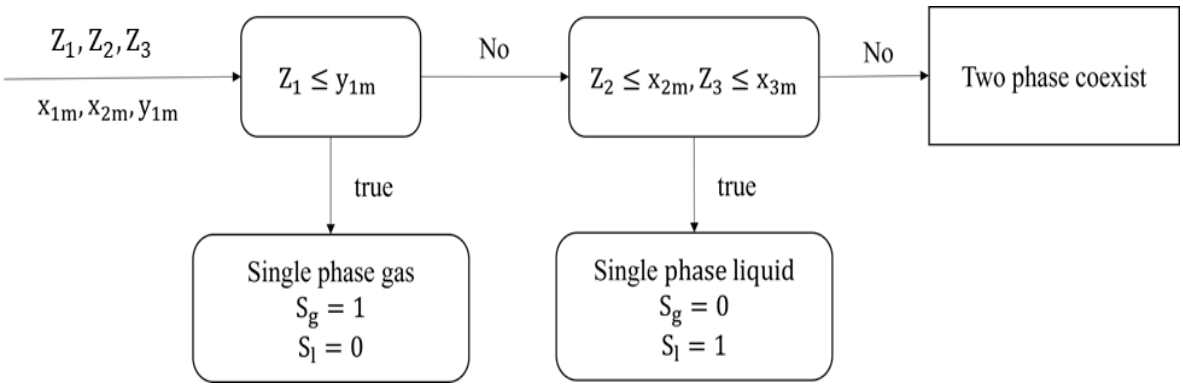

Figure 3.5 Scheme for determining phase choices

If the phase condition falls into single-phase criteria (gas or liquid), the phase composition (in mass fractions) can be described by Z_i. For single liquid condition, the dissolved salt should be reconsidered. For single gas condition, as no salt should appear in the gas mixture, the second primary variable, X_{sm} should shift to 10+ZERO, indicating all salt precipitates.

For the two-phase condition, we need to carefully calculate the phase mole fractions or phase saturations. As discussed in section 3.2, n^v has no unique solution because the calculation of the phase composition does not strictly follow material balances. We derive n^v from the following:

$$n^v y_1 + n^l x_1 = Z_1 \tag{3.66}$$

$$n^v + n^l = 1 \tag{3.67}$$

where, n^l is the mole fraction of the aqueous phase. Then we correct y_2 and y_3 based on n^v and n^l,

$$y_2 = \frac{Z_2 - x_2 n^l}{n^v} \tag{3.68}$$

$$y_3 = \frac{Z_3 - x_3 n^l}{n^v} \tag{3.69}$$

The following steps are the same as in the iterative approach.

3.3.4 Fluid thermodynamic properties

This section will introduce the computation of the thermodynamic properties of the gas mixture and aqueous solution. These properties include density, specific enthalpy, and viscosity. Correlations in ECO2N (Pruess 2005) are borrowed for properties of aqueous solutions. For density and specific enthalpy, only water, dissolved NaCl, and CO_2 are taken into account. The properties of C_1 to C_3 in their aqueous state were not found in the literature, supposedly as a result of small solubilities and lack of interest. For viscosity, it considers only water and dissolved NaCl. The density of the gas mixture is calculated using widely adopted correlations that consider all components, which will be detailed in the following content.

3.3.4.1 Density

The aqueous solution density calculation starts from brine density by the approach in Battistelli et al. (1997), which refers to correlations of Haas (1976) and Andersen et al. (1992). The dissolved CO_2 is considered by assuming the additivity of brine and dissolved CO_2:

$$\frac{1}{\rho_{aq}} = \frac{1 - x_2}{\rho_b} + \frac{x_2}{\rho_{CO_2}} \tag{3.70}$$

where ρ_{CO_2} is the partial density of the dissolved CO_2, which is temperature-dependent and calculated from the correlation developed by Garcia (2001). The molar volume of dissolved CO_2 (V_ϕ) assuming infinite dilution can be calculated as:

$$V_\phi = a + bT + cT^2 + dT^3 \tag{3.71}$$

in which V_ϕ is in cm^3/gmole, temperature T is in ℃, and a to d are fitting parameters given in Table 3.6.

Table 3.6 Empirical parameters for molar volume of dissolved CO_2

a	37.51
b	-9.585e-2
c	8.74e-4
d	-5.044e-7

The partial density of dissolved CO_2 can be obtained as follows in units of kg/m^3:

$$\rho_{CO_2} = \frac{MW_{CO_2}}{V_\phi} \times 10^3 \tag{3.72}$$

where MW_{CO_2} is the molar mass of CO_2. It is reasonable to neglect the pressure dependence of ρ_{CO_2} because dissolved CO_2 accounts for only a few percent and is always dilute.

The calculation of gas density (ρ_g) requires molar volume (MV) and the average molar mass of the components:

$$MV = \frac{z_{fac} RT}{P} \tag{3.73}$$

$$\rho_g = \frac{\sum y_i MW_i}{MV} \tag{3.74}$$

where Z_{fac} is the gas compressibility factor obtained from PREOS and R is the universal gas constant.

3.3.4.2 Viscosity

The viscosity of the aqueous solution is the brine viscosity obtained through a correlation in Phillips et al. (1981). The dissolved gas species are neglected, which is reasonable considering small solubilities. The viscosity of the gas mixture considers all components, except NaCl, using Lohrenz-Bray-Clark correlation adapted from the original work by Jossi et al. (1962):

$$[(\mu - \mu^*)\xi + 10^{-4}]^{0.25} = a_0 + a_1\rho_r + a_2\rho_r^2 + a_3\rho_r^3 + a_4\rho_r^4 \tag{3.75}$$

where $\mu^*$is the viscosity of the gas mixture at low pressure (or dilute gas mixture viscosity), ξ is the viscosity-reducing parameter, and ρ_r is the reduced density, which is the ratio of the density to the critical density. a_0 to a_4 are fitting parameters. These parameters are used as universal constants as default.

ξ and can be expressed as:

$$\xi = \frac{(\sum_i y_i T_{ci})^{\frac{1}{6}}}{(\sum_i y_i MW_i)^{\frac{1}{2}}(\sum_i y_i p_{ci})^{\frac{1}{6}}} \tag{3.76}$$

and ρ_c is defined as:

$$\rho_c = \frac{1}{v_{c,mix}} = \frac{1}{\sum_i y_i v_{ci}} \tag{3.77}$$

where v_{ci} is the critical volume of the component i. v_{ci} are constants in our model are constants because there are no C_7 or plus components that require correlations or tuning. Now μ^* can be computed as:

$$\mu^* = \frac{\sum_i y_i \mu_i^* \sqrt{MW_i}}{\sum_i y_i \sqrt{MW_i}} \tag{3.78}$$

where μ_i is given as follows if $T_{ri} < 1.5$:

$$\mu_i^* = 3.4 \times 10^{-4} \frac{T_{ri}^{0.94}}{\xi_i} \tag{3.79}$$

and if $T_{ri} \geq 1.5$:

$$\mu_i^* = 1.778 \times 10^{-4} \frac{(4.58T_{ri} - 1.67)^{\frac{5}{8}}}{\xi_i} \tag{3.80}$$

For the above two equations the viscosity-reducing parameter of component i is given by

$$\xi_i = \frac{T_{ci}^{\frac{1}{6}}}{MW_i^{\frac{1}{3}} p_{ci}^{\frac{2}{3}}} \tag{3.81}$$

3.3.4.3 Specific enthalpy

The specific enthalpy of the aqueous solution is the summation of brine and dissolved gas enthalpy multiplied by their mole fractions (Lorenz et al. 2000):

$$h_{aq} = (1 - x_2)h_b + x_2 h_{CO_2,aq} \tag{3.82}$$

This correlation is valid for a temperature from 25 ℃ to 300 ℃ and all NaCl concentrations. $h_{CO_2,aq}$ is a function of temperature, pressure, and NaCl concentration, which sums the gas CO_2 enthalpy and the heat of dissolution. For gas-like CO_2, we have:

$$h_{CO_2,aq}(T, P, X_s) = h_{CO_2,g}(T, P) + h_{dis,g}(T, X_s) \tag{3.83}$$

where $h_{dis,g}$ can be obtained from an equation in Battistelli et al. (1997). For high pressure condition, liquid-like CO_2, which is more likely the case for CO_2 geo-sequestration, $h_{CO_2,aq}$ is written as:

$$h_{CO_2,aq}(T, P, X_s) = h_{CO_2,l}(T, P) + h_{dis,l}(T, X_s) \tag{3.84}$$

Liquid and gaseous CO_2 may co-exist along the saturation line, in which case the above two equations should be equal, giving:

$$h_{dis,l}(T, X_s) = h_{dis,g}(T, X_s) + h_{CO_2,gl}(T) \tag{3.85}$$

and the specific enthalpy of CO_2 vaporization can be expressed as:

$$h_{CO_2,gl}(T) = h_{CO_2,g}(T, P_s) - h_{CO_2,l}(T) \tag{3.86}$$

where P_s is the saturated vapor pressure, which is a function of temperature. Pruess (2005) reported that these equation function well for single-gas or two-phase h_{CO_2}. However, for single-

liquid conditions, a modified formulation should be used. For CO_2 storage in depleted gas reservoirs, it is more likely that two phases co-exist. But considering the presence of the bottom aquifer, which is in a single liquid condition with possible CO_2 invasion, such a formulation is also adopted in our model.

The specific enthalpy of the gas mixture is calculated as the ideal gas specific enthalpy plus enthalpy departure to address real gas effects:

$$H = \left(H - H^{ig}\right) + H^{ig} = \left(H - H^{ig}\right) + \sum_i y_i H^{i,ig} \tag{3.87}$$

where $H^{i,ig}$ is the specific enthalpy of gas component i at ideal gas conditions, which can be calculated as:

$$H^{i,ig} = H^{i,ig,0} + C_{p,i}(T - T^0) \tag{3.88}$$

where superscript 0 denotes the reference state (25℃) and $C_{p,i}$ is the heat capacity, which is a function of T as,

$$C_{p,i} = a + bT + cT^2 + dT^3 \tag{3.89}$$

where T is in ℃. a, b, c, and d are fitting parameters. The enthalpy departure, $(H - H^{ig})$, is calculated using PREOS to come up with the real gas enthalpy.

CHAPTER 4

MODEL VALIDATION AND VERIFICATION

4.1 Validation via Experimental Results

Turta et al. (2008) conducted a series of core flooding tests to study the performance of CO_2-EGR in sandstone cores. They injected CO_2 to displace methane from dry (100% saturated with methane) and wet cores (with residual brine). The brine is a 3% NaCl solution. Two of the tests were picked for validation and the core properties and test parameters are given in Table 4.1 and Table 4.2, respectively. The first test used the dry core, for which the phase condition was single gas. The first comparison between the test and simulation can only provide little reference to the model accuracy but can help examine the precision of the provided data, such as core and test parameters. In the simulation, a cuboid model was used to represent the cylindrical core, which was discretized into 20×5×5 grid blocks. The cross-sectional area of the cuboid model was identical to that of the real core. The tests were carried out under constant temperature and confining pressure, and as a consequence, the thermal and geomechanical functions were turned off.

Table 4.1 Physical properties of the core

Core properties	
Length (cm)	30.48
Diameter (cm)	3.81
Air Permeability (mD)	500
Porosity (frac.)	0.25
Pore volume (cc)	72.4

Table 4.2 Test parameters for tests with dry core and core with irreducible water saturation

Test parameters				
Test #	Initial Pressure (bar)	Temperature (℃)	Interstitial Velocity (IV) (m/day)	Injection Rate Converted from IV (kg/s)
Dry Core	62	70	2.52	9.732e-7
With S_{rw}=0.17	62	70	1.1	3.717e-7

As shown in Figure 4.1 the simulation result matches the experimental results pretty well for both methane recovery and CO_2 concentration in the effluent. This indicates that the experimental parameters provided by Turta et al. (2008) are very precise, and the core is homogeneous. In such circumstances, the next comparison that uses a wet core should be reliable (see Figure 4.2). Here, we employ average absolute deviation (AAD) and maximum absolute deviation (MAD) to express the difference between simulation results and experimental results,

$$\text{AAD } \% = \left(100 \times \sum abs\left(\frac{\left[(X_{exp} - X_{sim}\right)}{X_{exp}}\right]\right)/N \tag{4.1}$$

$$\text{MAD } \% = 100 \times \max\left(abs\left(\frac{\left[(X_{exp} - X_{sim}\right)}{X_{exp}}\right]\right) \tag{4.2}$$

The AAD for methane recovery is 2.46%, and MAD appears at 1.05 PV of CO_2 injection, which is around 2.9%. The AAD for the methane concentration in the effluent is 3.72%, and MAD shows at 1.12 PV, which is around 5.8%. The simulated results fit well with the experimental results, which, to a certain degree, confirm the model's accuracy.

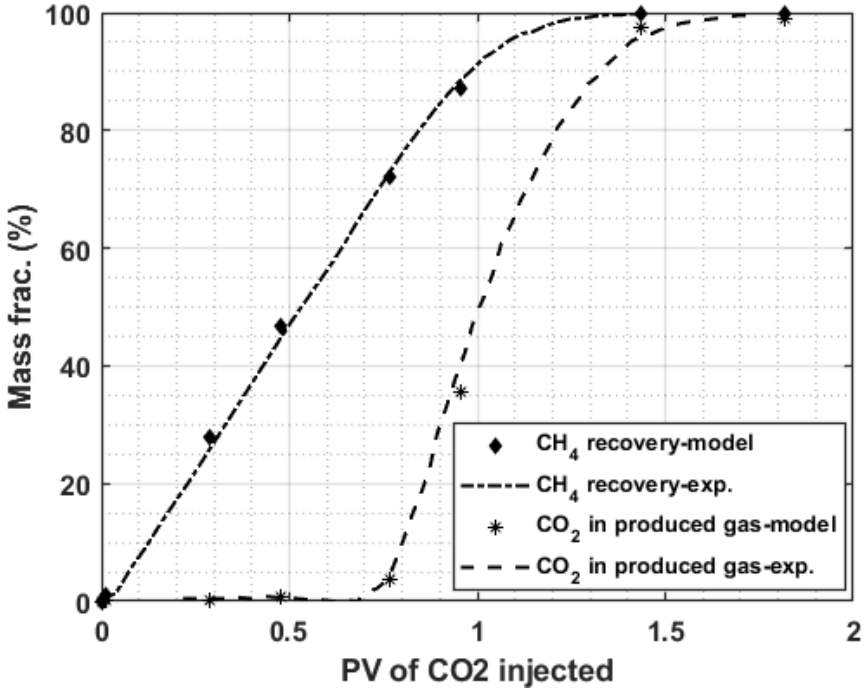

Figure 4.1 Results comparison for the core flooding test using a dry core.

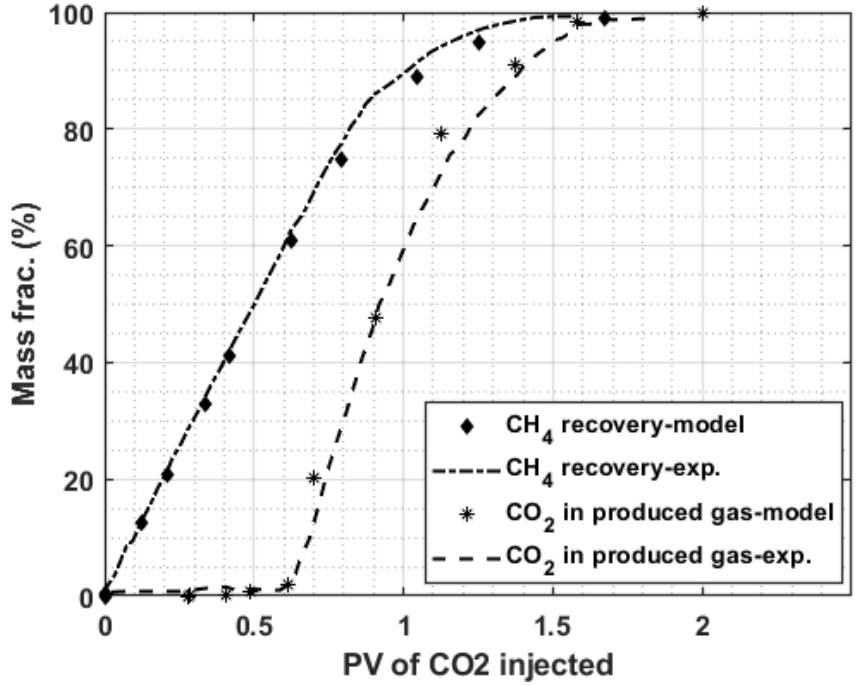

Figure 4.2 Results comparison for the core flooding test using core with irreducible brine saturation.

4.2 Verification with TOUGH2-EOS7C

In the above, the modeling results matched well with the experimental results, but only in terms of methane recovery and concentration in the effluent. Other important parameters, such as phase composition (e.g., CO_2 concentration in each phase) and pressure distribution were not available. Thus, a comparison with TOUGH2-EOS7C was performed to verify our model to deeper levels of detail. TOUGH2-EOS7C enables TH modeling of CO_2 EGR or underground storage. It considers five components, including water, salt (NaCl), CO_2 (or N_2), tracer, and methane. Density, viscosity, and other thermodynamic properties are computed using real gas property modules.

The first verification is the comparison of the solubility calculations in CH_4-CO_2-water system. Table 4.3 lists the solubilities calculated at 40 bars and 40 ℃, whereas Table 4.4 lists data at 100 bar and 40 ℃, where CO_2 and CH_4 are in supercritical conditions. Note the x_g and x_l in these tables are in mole fractions and the reference data was provided by Oldenburg et al. (2004). It shows that the calculated solubilities were very consistent with either those of EOS7C or experimental data.

Table 4.3 Solubilities of CO_2 and CH_4 in water at 40 bars and 40 ℃.

	Gas phase		Aqueous phase	
	$x_g^{CH_4}$	$x_g^{CO_2}$	$x_l^{CH_4}$	$x_l^{CO_2}$
EOS7C	2.62×10^{-3}	0.996	2.05×10^{-6}	1.33×10^{-2}
Our module	2.62×10^{-3}	0.996	2.08×10^{-6}	1.32×10^{-2}
Reference	0	1.0	0	1.37×10^{-2}
EOS7C	0.501	0.497	3.66×10^{-4}	6.82×10^{-3}
Our module	0.501	0.497	3.67×10^{-4}	6.79×10^{-3}
Reference	0.5	0.5	3.66×10^{-4}	6.74×10^{-3}
EOS7C	0.998	0	7.15×10^{-4}	0
Our module	0.998	0	7.23×10^{-4}	0
Reference	1	0	7.22×10^{-4}	0

Table 4.4 Solubilities of CO_2 and CH_4 in water at 100 bars and 40 ℃.

	Gas phase		Aqueous phase	
	$x_g^{CH_4}$	$x_g^{CO_2}$	$x_l^{CH_4}$	$x_l^{CO_2}$
EOS7C	6.98×10^{-3}	0.992	2.18×10^{-5}	2.13×10^{-2}
Our module	6.98×10^{-3}	0.992	2.21×10^{-5}	2.09×10^{-2}
Reference	0	1.0	0	2.19×10^{-2}
EOS7C	0.503	0.497	7.93×10^{-4}	1.21×10^{-2}
Our module	0.503	0.497	8.03×10^{-4}	1.19×10^{-2}
Reference	0.5	0.5	7.95×10^{-4}	1.21×10^{-2}
EOS7C	0.999	0	1.49×10^{-3}	0
Our module	0.999	0	1.52×10^{-3}	0
Reference	1	0	1.54×10^{-5}	0

Next, 1-D simulation runs were conducted using our model and TOUGH2-EOS7C. Since TOUGH2-EOS7C does not have geomechanical option, the simulations did not involve geomechanics. The simulation runs considered the injection of CO_2 into a depleted gas (only methane and brine due to the limited capabilities of EOS7C) reservoir, with irreducible water saturation of 25%. For simplicity, the model was 1D, with 20 grids in the X direction and six girds in the Z direction, as given in Figure 4.3. The rock properties are given in Table 4.5. The initial conditions were listed in Table 4.6. Note that the initial water saturation was set at 0.25, which was a little greater than the residual water saturation. We believe this setting is more reasonable than setting water saturation to 0 (e.g., Fan et al. 2021; Liu et al. 2022) or exactly the residual water saturation, as the water being refilled from the bottom water or surrounding water-

bearing zones after shut-in. The diffusivity of all components was set to 1e-5 m^2 s^{-1} in the gas phase and 1e-10 m^2 s^{-1} in the aqueous phase.

Table 4.5 Rock and other properties of the 1-D CO_2 storage run.

Rock and other properties	**Value**
Rock density (kg/m^3)	2600
Porosity (frac.)	0.30
Absolute permeability (I, J, K) (m^2)	1.E-13, 1.E-13, 1.E-13
Formation heat conductivity (W/m℃)	2.51
Specific heat (J/kg ˚C)	1.E3
Rock compressibility (Pa^{-1})	4.5E-10
Relative permeability model	van Genuchten-Mualem (Van Genuchten 1980)
Capillary pressure model	van Genuchten function
Residual water saturation	0.20
Residual gas saturation	0.16 (0.15 for capillary model)

Table 4.6 Summary of the initial condition for 1-D simulation run.

Initial Condition	Value
P (Pa)	150.E5
Salt concentration (mass frac.)	0.0
Gas saturation (frac.)	0.75
T (℃)	65

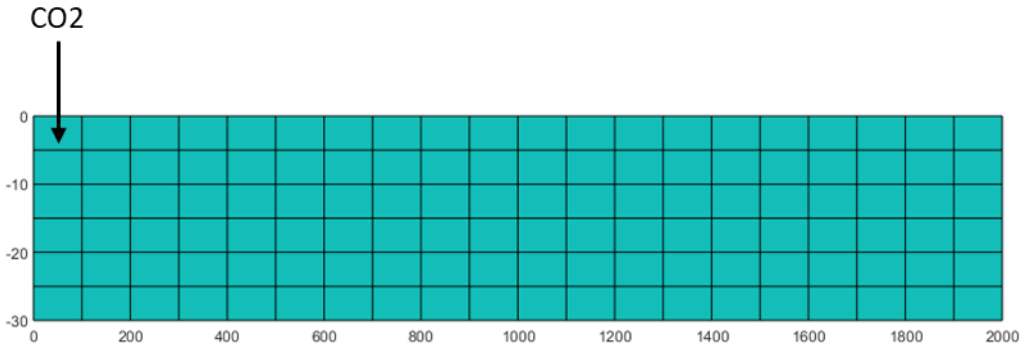

Figure 4.3 Discretization of the 1-D model, of which the length along Y direction is 100m.

The injection remains for two years at a constant rate of 4 kg/s from the top-left corner. Before that, the models run for a year without any sink/source terms to reach gravity equilibrium. Figure 4.4 shows the comparison of the overall CO_2 concentration (mass frac.) profile. It turned out that the CO_2 front reached 1100 m away from the injector. The results are very close, and barely notable from the graphs, with AAD of 0.78% and MAD of 0.84%. Figure 4.5 is the comparison of CO_2 mass fraction in the aqueous solution (x_{CO_2}). The AAD is 3.44% and the MAD is 4.21%. In Figure 4.6, the difference in pressure can be seen clearly because the pressure range employed here is from 205 to 211 bar. It demonstrates that the difference is still very small, with an AAD of 0.58% and MAD of 0.73%. To describe it in a more straightforward manner, our model predicted the pressure around 1 bar greater than EOS7C.

Another important parameter, the methane concentration in the aqueous phase, cannot be compared via these contour plots, because it varies from 10^{-6} to 10^{-3} depending on the CO_2 invasion. Mostly, the differences are within a few percent, except for the three grids near the injection well, where the difference can reach more than 30 %. However, it barely has any impact on the accuracy of the model, unless the goal is to analyze methane dissolution near the wellbore.

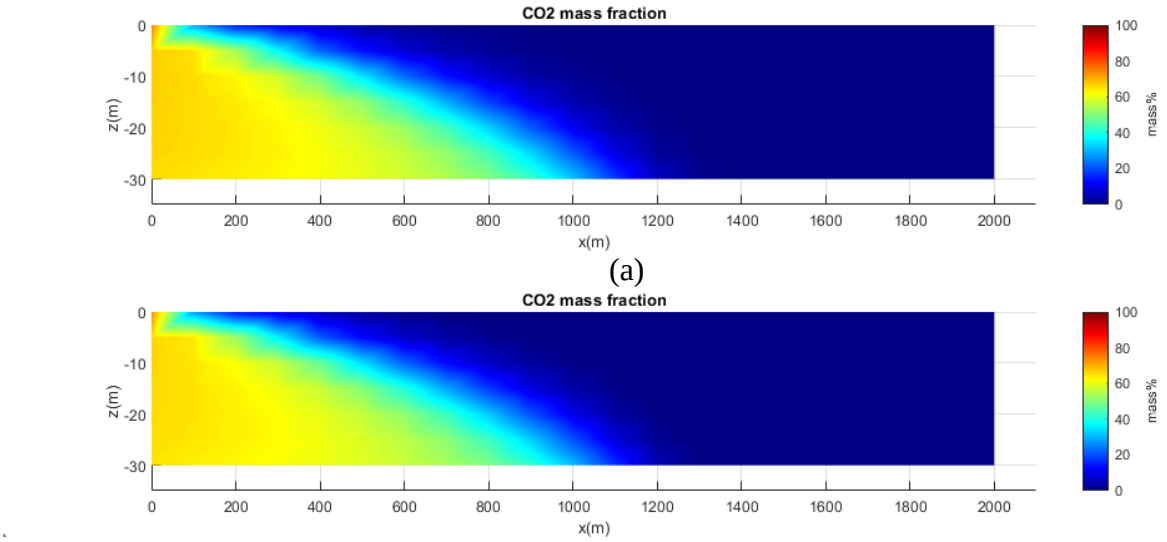

(a)

(b)

Figure 4.4 Comparison of CO_2 mass fraction between (a) our model and (b) EOS7C.

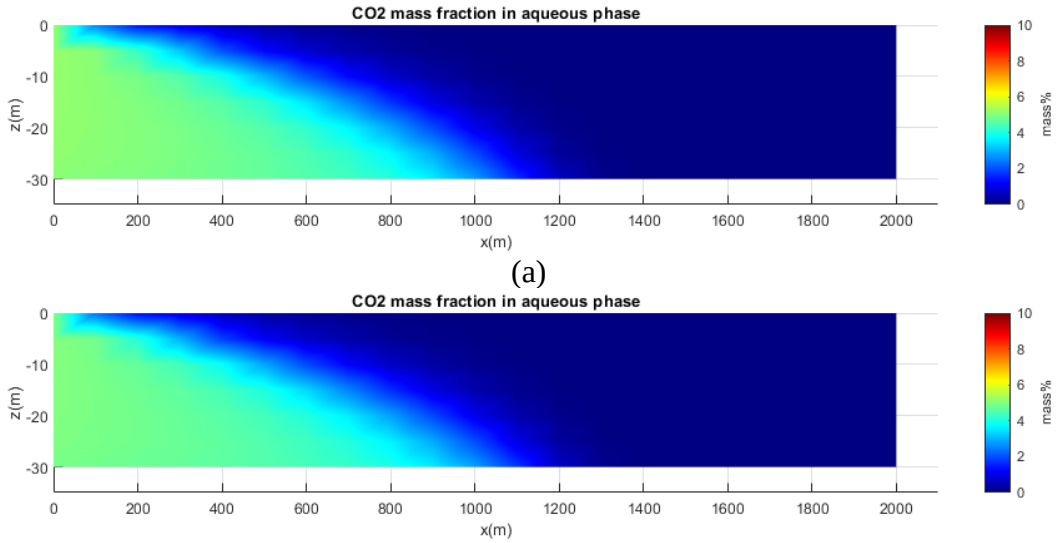

(a)

(b)

Figure 4.5 Comparison of CO_2 mass fraction in the aqueous phase: (a) Our model, (b) EOS7C.

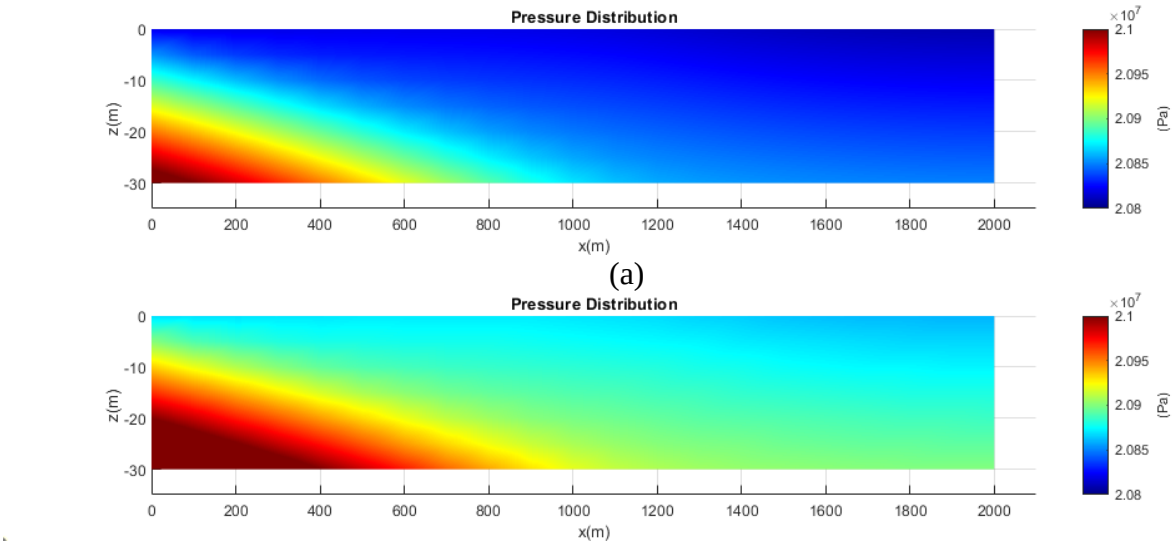

Figure 4.6 Comparison of Pressure distribution between (a) our model and (b) EOS7C.

Then a comparison of 3D simulations was conducted using the setup given in Table 4.7. This test run considered CO_2 injection into a 3-D reservoir. The cuboid model we used represented one-fourth of the reservoir ($300\text{m} \times 300\text{m} \times 30\text{m}$), where the injector was located at the corner. This time the NaCl concentration was set at 0.06 to examine the calculated solubility in saline water. The CO_2 injection took place at the middle depth, 15 m, and continued for 2 years at a rate of 2kg/s. The specific enthalpy of the injected CO_2 is assumed to be 2.49×10^5 J/kg at 200 bar and 25℃. The comparison of the simulation results is given in Figure 4.7. The pressure distributions seem completely different, which is because the scale we used ranged from 236 bar to 240 bar. We used such a small range to display the pressure profile since the pressure differences between elements were considerably small. The AAD is only around 0.8%.

Table 4.7 setup for the 3D simulation run

Properties	**Value**
Pressure (pa)	200.e5
Brine saturation (frac.)	0.25
NaCl concentration (mass frac)	0.06
Temperature (℃)	75
Rock density (kg/m^3)	2600
Porosity (frac.)	0.3
Absolute permeability (I, J, K) (m^2)	1.E-13, 1.E-13, 1.E-13
Formation heat conductivity (W/m℃)	2.51
Rock specific heat (J/kg ˚C)	1.e3
Compressibility (Pa^{-1})	4.5e-10

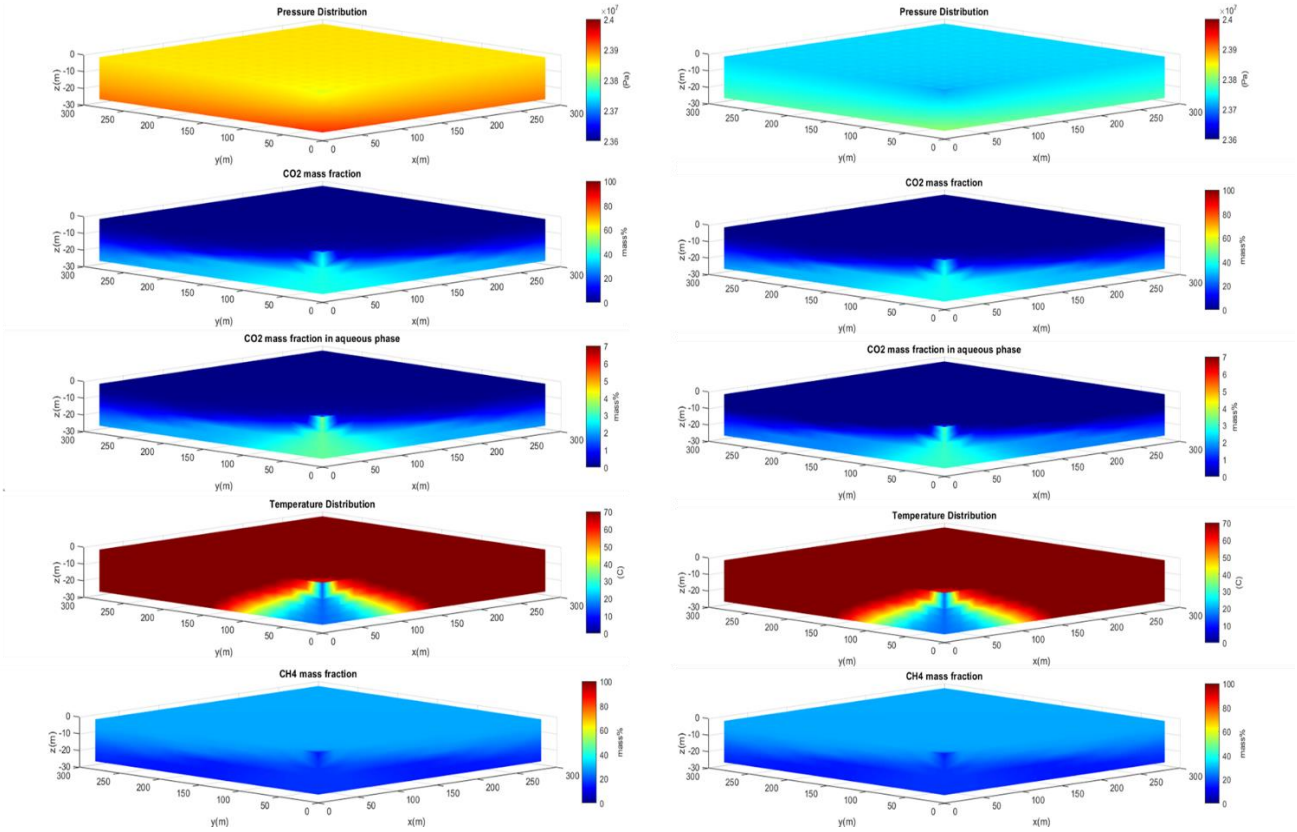

Figure 4.7 Comparison of the simulation results of TOUGH2-CSM (left) and TOUGH2-EOS7C (right). The plots from top to bottom are pressure, overall CO_2 concentration, CO_2 concentration in the aqueous solution, temperature, and overall CH_4 mass concentration.

4.3 Verification of mean stress calculation via 1D consolidation problem

The 1D consolidation problem used for the verification is Terzaghi's problem (Terzaghi et al. 1996), which refers to the uniaxial compression of a specimen. The specimen is laterally constrained, which means the fluid can only flow through the top surface (Figure 4.8). At the moment that the compression is applied and fluid has not yet started leaking, the pore pressure will rise to the undrained value. Such a phenomenon is called the Skempton effect. After that, being subjected to the compression, the specimen consolidates, and the fluid leaks off from the top, as time goes on. The pore pressure during such a process can be described by an analytical solution:

$$p(z,t) = \frac{4}{\pi} p_0(z) \sum_{1,3,\dots}^{\infty} \frac{1}{n} \exp\left[-\frac{n^2\pi^2 ct}{4h^2}\right] \sin\left[\frac{n\pi z}{2h}\right] \tag{4.3}$$

and the vertical displacement can be expressed as:

$$u(z,t) = c_M p_0(z)\{(L-z) - \frac{8h}{\pi^2} \sum_{1,3,\dots}^{\infty} \frac{1}{n^2} \exp\left[-\frac{n^2\pi^2 ct}{4h^2}\right] \sin\left[\frac{n\pi z}{2h}\right]\} + \mu_0\,(z) \tag{4.4}$$

In above:

$$p_0(z) = \frac{\alpha M}{K_u + \frac{4G}{3}} p_L \tag{4.5}$$

$$u_0(z) = \frac{1}{K_u + \frac{4G}{3}} p_L (L+z) \tag{4.6}$$

where M is the Biot Modulus, K_u is the undrained bulk modulus, c_M is the vertical uniaxial compressibility, and c is the consolidation coefficient. They can be calculated using the following correlations:

$$M = \left[\phi C_f + \frac{\alpha - \phi}{K_s}\right]^{-1} \tag{4.7}$$

$$K_u = \lambda + \frac{2G}{3} + \alpha^2 M \tag{4.8}$$

$$c_M = (\lambda + G)^{-1} \tag{4.9}$$

$$c = k/[\rho g(M^{-1} + \alpha^2 c_M)] \tag{4.10}$$

where C_f is the fluid compressibility, α is the Biot's coefficient, K_s is the bulk modulus, λ and G are lame constants, and k is the permeability. This problem was modeled in TOUGH2-CSM using a cartesian gird system with a dimension of $5m \times 5m \times 100m$. The top surface was subjected to a load of 2.0 MPa, giving an undrained pressure of 1.973 MPa, which was used as the initial pressure. The simulation parameters are given in Table 4.8. From Figure 4.9 and Figure 4.10, one can see that both the pore pressure and vertical displacement obtained from TOUGH2-CSM matched well with the analytical solution.

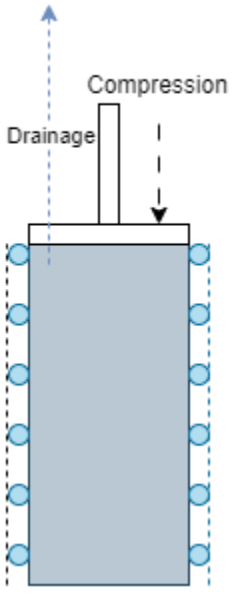

Figure 4.8 Schematic of Terzaghi's problem

Table 4.8 Input parameters for 1D consolidation problem

Parameters	**Value**
Pressure (Pa)	197.3e5
Water density (kg/m^3) (for analytical solution)	1000
Water compressibility (Pa^{-1}) (analytical)	4.4e-10
Temperature (℃)	20
Rock density (kg/m^3)	2600
Porosity (frac.)	0.25
Absolute permeability (m^2)	1.E-13
Poisson's ratio (unitless)	0.25
Young's Modulus (GPa)	0.1
Biot's coefficient (unitless)	1
Well index (m^3/Pa s)	2e-10
Bottomhole pressure (Pa)	1e5

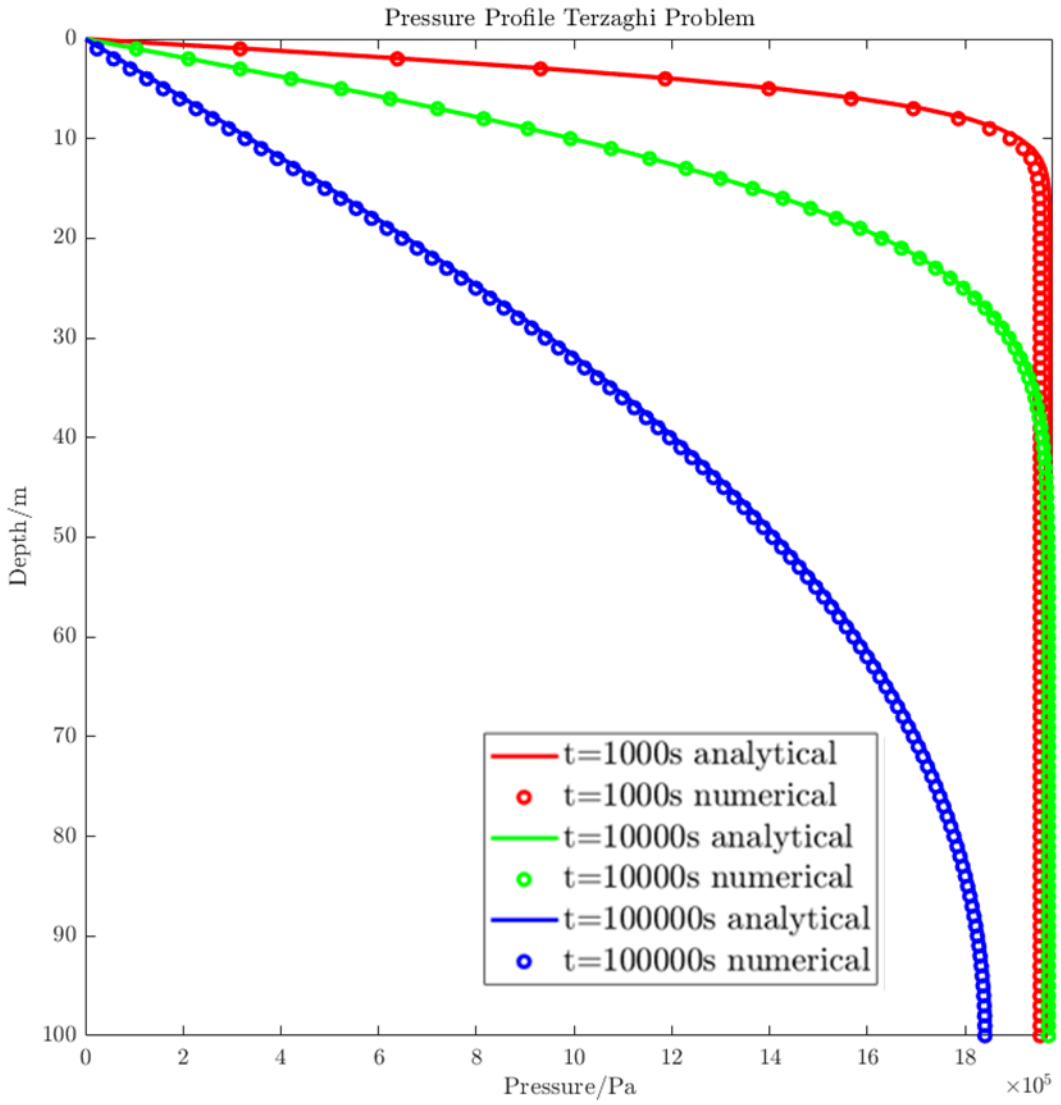

Figure 4.9 Comparison of the pore pressure obtained from the analytical solution and TOUGH2-CSM for the 1D consolidation problem

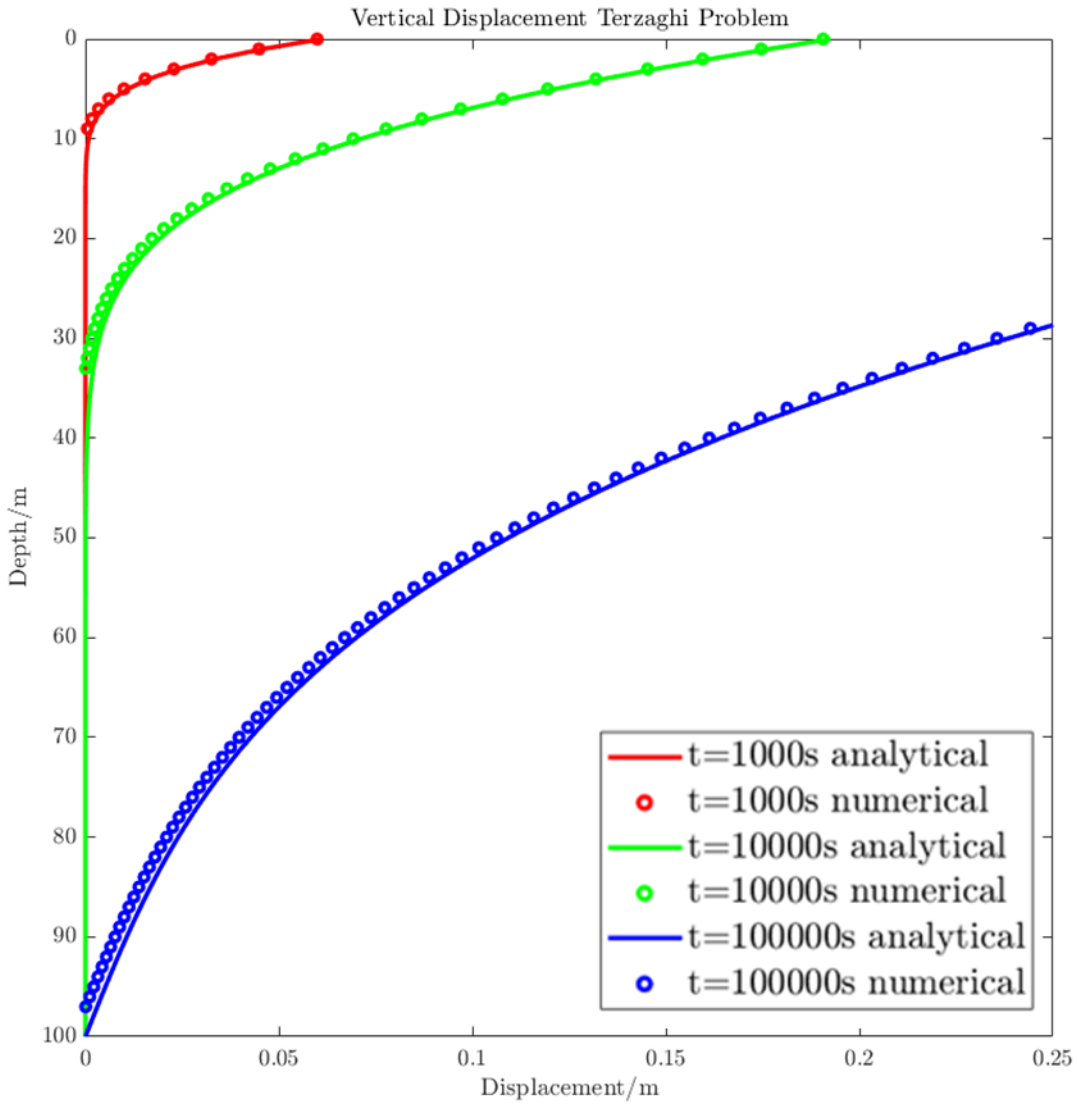

Figure 4.10 Comparison of the vertical displacement obtained from the analytical solution and TOUGH2-CSM for the 1D consolidation problem

CHAPTER 5

MODEL APPLICATION AND CASE STUDY

This chapter presents a few simulation studies conducted using TOUGH2-CSM, investigating both sheer CO_2 storage and CSEGR. These studies evaluated the storage capacity and enhanced natural gas recovery (only for CSEGR) and analyzed the impact of injection strategies, such as injection rate and depth.

5.1 THM Simulation Considering C_1 to C_3

Here, a THM-coupled simulation run was conducted using a cuboid model, which typically represented a quarter of the five-spot well pattern. The model considered CO_2 storage in a depleted gas reservoir, of which the gas composition was 84.55% methane, 10.47% ethane, and 4.98% propane, in mass fraction. The simulation run utilized correlations in Rutqvist et al. (2002) to address the stress-dependent porosity as follows

$$\phi = \phi_r + (\phi_0 - \phi_r)\exp\left(\alpha \times \sigma_M'\right) \tag{5.1}$$

where ϕ_r is the residual porosity at high stress, ϕ_0 is the porosity at zero stress, α is the exponent that should be experimentally determined, and σ_M' is effective stress.

The permeability is correlated to porosity as

$$k = k_0 \times \exp\left[c \times \left(\frac{\phi}{\phi_0} - 1\right)\right] \tag{5.2}$$

where k_0 is the permeability at zero stress, and c should be experimentally determined.

The cuboid model that has a size of 200×200×30 m was discretized into 20×20×6 girds, as given in Figure 5.1. No constant boundary conditions (pressure, temperature, or saturation) were assigned to external boundaries. All boundaries are closed boundaries except that a bottom water aquifer was modeled by adding 8 finite volume grids beneath the bottom layer, as marked

in blue in Figure 5.2. It was assumed that the aquifer size is four times the gas zone size, which led to a grid size of around 770,000 m^3 (total volume). The water zone contained water and a small amount of gas (3%) consisted of methane only. The rock properties were exactly the same for both the aquifer and gas zone. Note that for field case run, the aquifer size, if not provided, should be determined through history matching of the water production. After setting up, the first step was the equilibrium run, which continued for ten years without any sink and source terms to reach gravity equilibrium. Then CO_2 was injected from the location in Figure 5.1 at a rate of 6 kg/s (or equivalently, 189,000 tonnes/year) for 2 years. The rock properties and some initial setups can be found in Table 5.1.

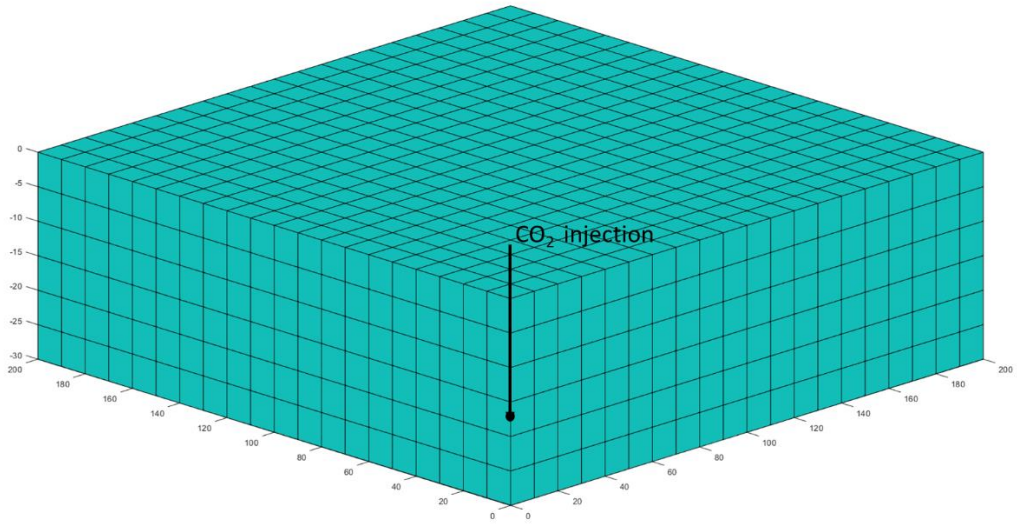

Figure 5.1 Model discretization for THM simulation run.

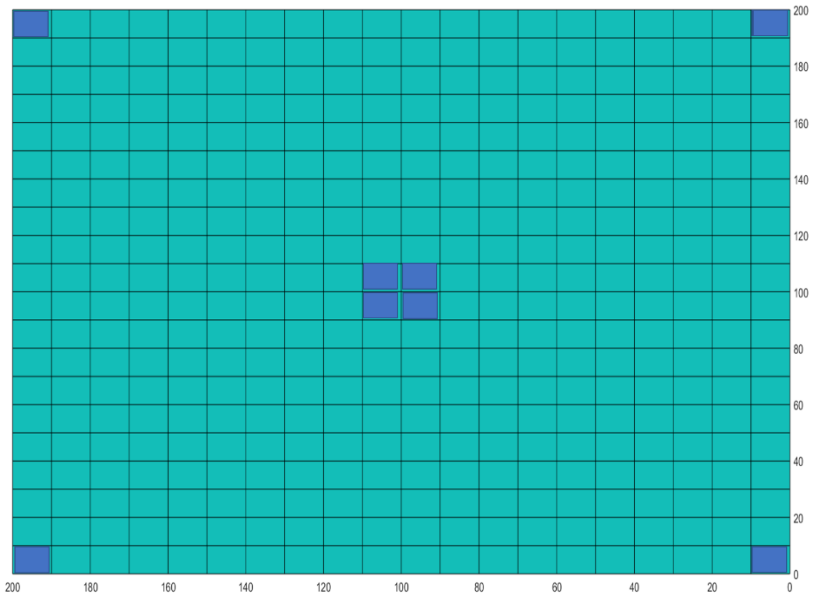

Figure 5.2 Locations of the 8 finite volume grids added beneath the bottom layer.

Figure 5.3 shows the results collected at the end of the simulation, including pressure, temperature, CO_2 mass fraction, and CO_2 concentration in the aqueous phase. With nearly 182,300 tonnes of CO_2 being injected, the reservoir pressure increased from 150 to around 257 bar. Around 160,000 tonnes of CO_2 showed in the gas zone, and the rest appeared in the saline aquifer. The storage through solubility trapping accounted for 3.5% and 97.4 % of the overall storage in the gas zone and bottom aquifer, respectively.

The temperature change is more significant in the lower layers because the cold CO_2 sinks due to higher density compared with hydrocarbon gases. The temperature near the wellbore is very close to 25℃, the injection temperature. The CO_2 mass fraction is positively related to the distance from the injection well and reaches 100% in a few grids near the wellbore. The CO_2 mass fraction, combined with the temperature profile, can properly reveal the evolution of the CO_2 plume. The CO_2 concentration in the aqueous phase depends on the overall CO_2 mass fraction, where the highest values appear to be around 6%. Note there is a small portion dyed

dark red around the wellbore, and that is because these grids fell into single-phase gas conditions. This demonstrates the residual water was carried away from those locations by the gas flux.

The above simulation was run using the fully coupled THM option, which predicted the reservoir pressure more accurately with the mean stress calculation involved. Here, another simulation was run, this time with geomechanics decoupled to check whether the differences are significant. As shown in Figure 5.4, the average pressure is around 0.82 bar lower than that in the THM run. This indicates that TH simulation may underestimate the reservoir pressure, during CO_2 injection, even by a small amount. The reservoir temperatures are consistent, and the difference can be ignored. The differences in overall CO_2 concentration and CO_2 concentration in the aqueous phase are less than 0.35 %.

Next, another TH simulation was conducted, this time assuming the natural gas contained only methane. Even though the solubilities of C_2 and C_3 are considerably small, neglecting them could change the result due to the change in thermodynamic properties of the gas mixture, such as density, enthalpy, and viscosity. As shown in Figure 5.5, this average pressure at the end of the injection is around 256 bar, which is less than that in the last run, 257.8 bar. The average temperature estimated is 55.84 ℃, which is 0.4 ℃ less than that in the last case. The differences in CO_2 overall concentration and aqueous concentration are small (within a percent).

For CO_2 geo-sequestration, the reservoir pressure is very important. The pressure limit or the target pressure set for the CO_2 injection is directly related to the storage capacity. An accurate prediction of the reservoir pressure allows us to precisely estimate the CO_2 storage, and to some extent, prevent possible stability issues. In such circumstances, the model presented in this work can perform better than simulators without the capability of handling geomechanics coupling and/or more complex gas composition.

Table 5.1 Rock properties and other setups for the THM simulation run.

Rock properties	
Rock density (kg/m^3)	2600
Porosity (frac.)	0.35
Absolute permeability (I, J, K) (m^3)	1.E-12, 1.E-12, 1.E-12
Formation heat conductivity (W/m℃)	2.51
Specific heat (J/kg ˚C)	1.E3
Rock compressibility (Pa^{-1})	1.E-10
Poisson's ratio	0.25
Young's modulus (Pa)	5E-9
Biot's coefficient	1.0
Other setups	
Relative permeability model	van Genuchten-Mualem
Capillary pressure model	van Genuchten function
Residual water saturation	0.20
Residual gas saturation	0.16 (0.15 for capillary model)
Initial pressure (bar)	150
Initial temperature (℃)	65
Initial mean stress (bar)	387
Initial gas saturation (%)	78
Brine salinity (mass frac.)	0
CO_2 injection related	
Injection rate (kg/s)	2
Temperature (℃)	25
Specific enthalpy of the injected CO_2 (J/kg)	2.499E5

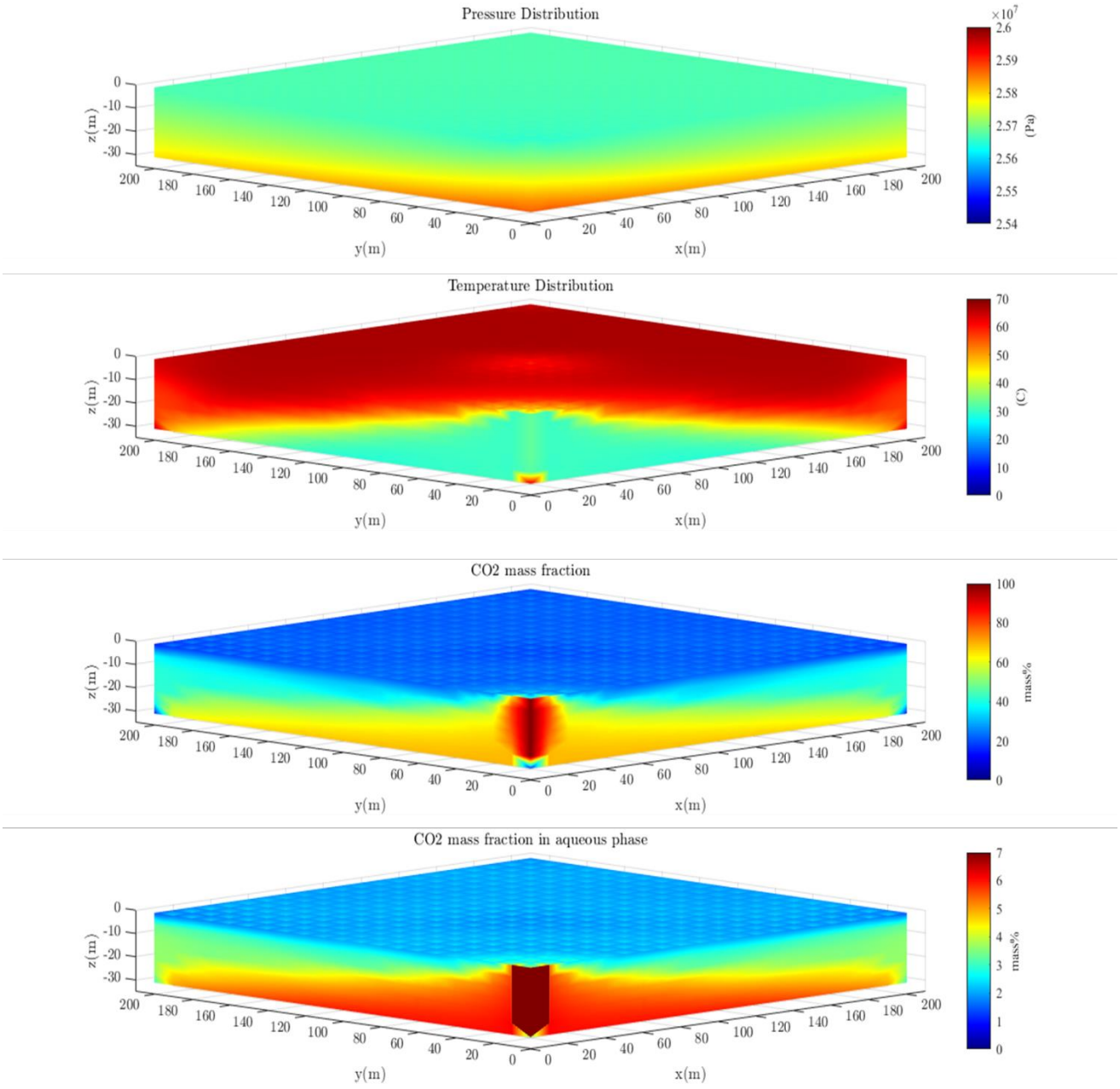

Figure 5.3 Results collected at the end of the simulation

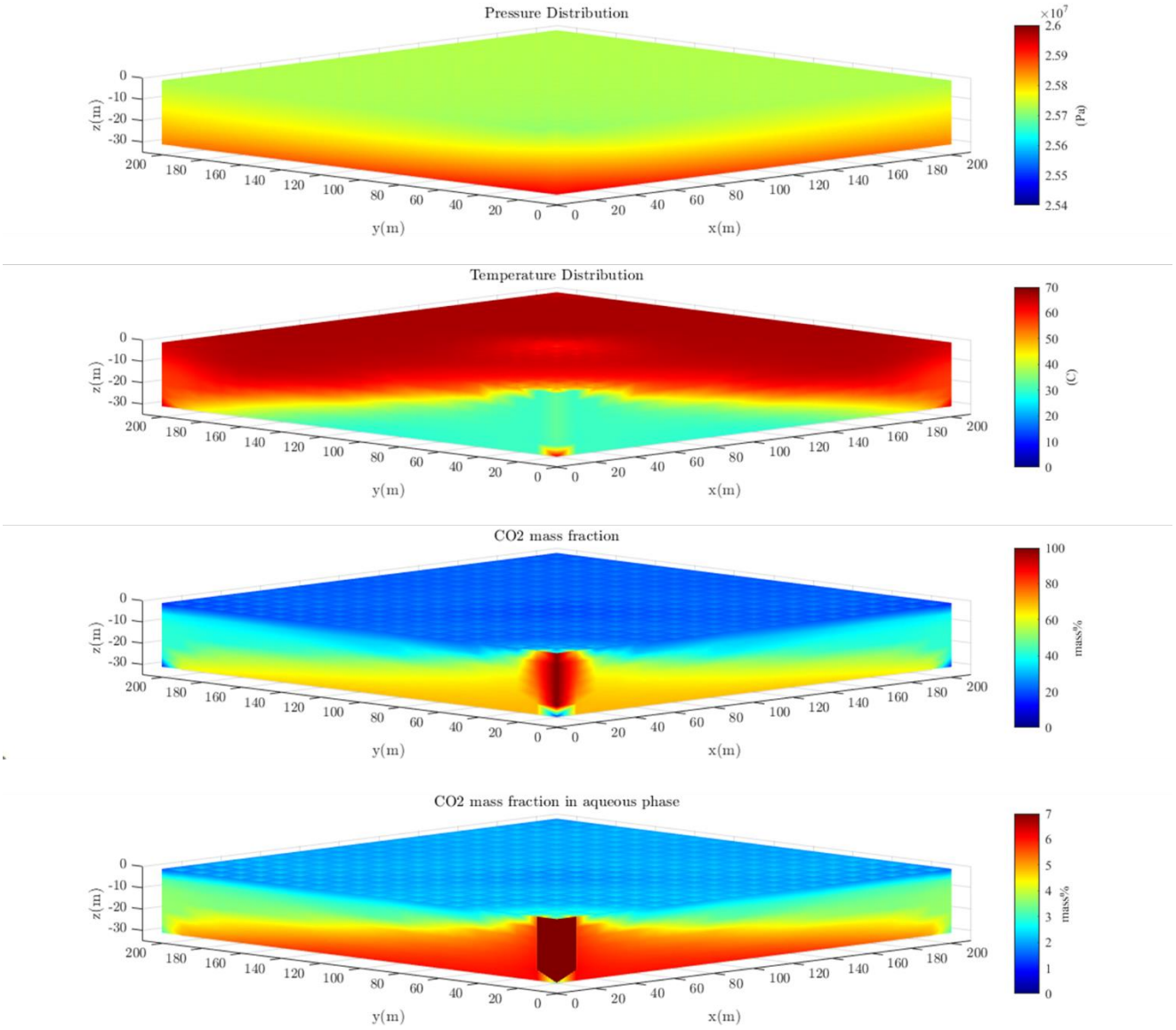

Figure 5.4 Results collected at the end of the simulation for TH run

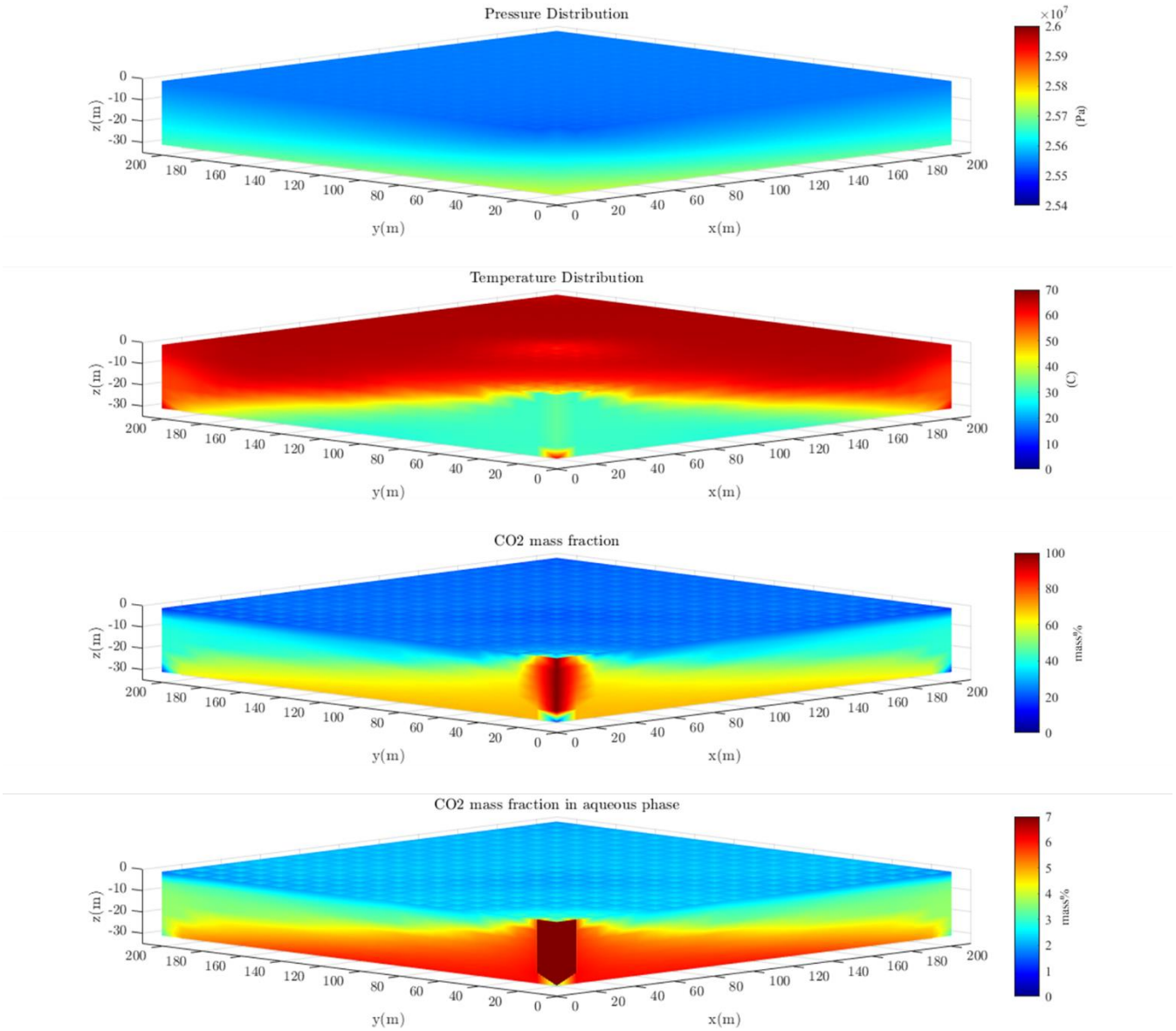

Figure 5.5 Results at the end of the TH simulation that considers natural gas as pure methane

5.2 CO_2 Storage in VR115_PO gas sand in the Gulf of Mexico

In this section, we present a simulation study of CO_2 storage in a gas reservoir, utilizing more realistic reservoir structures, boundary conditions, and rock and fluid properties. The geological site considered here is a gas sand, VR115_PO in the Gulf of Mexico. The reservoir had a subsea depth of 2225 m, with an average net thickness of 11.9 m and a total area of 1.6×10^6 m^2. Some major reservoir and fluid properties, including reserves and cumulative productions, are given in Table 5.2. The model contained six layers, of which the first four represented the gas-rich zone, where the water saturation equals the residual water saturation. To reveal the shape of the reservoir model, it was given in Figure 5.6 as six horizontal slices, each representing a layer.

There is not any type of constant boundary conditions applied to external boundaries. Assuming no interactions with adjacent reservoirs, the boundary conditions were based on a finite-volume bottom aquifer, as illustrated in yellow in Figure 5.6. The aquifer size was determined by adjusting the volume of those aquifer grid blocks to match the cumulative gas and water productions. Agartan et al. (2018) determined the depleted reservoir pressure to be 146 bars. This pressure was adopted in our history matching, making the work much easier.

The composition of the natural gas was unknown, and thereby, the simulation considered only methane for the gas composition. Since the rock's mechanical properties, such as Young's modulus and Poisson's ratio were not found, geomechanical coupling was turned off. The diffusion coefficients were set to 10^{-5} and 10^{-10} for gaseous and aqueous species, respectively, as recommended by Oldenburg (2007). In our best match, the cumulative gas production was around 4.82×10^8 m^3 and the water production was 5.49×10^6 m^3. In this case, the aquifer size was determined to be 4.623×10^7 m^3, which was nearly eight times the gas zone size. The output of this run was used as the initial condition in our base case.

The base case referred to CO_2 injection into this reservoir, through six injection wells, as shown in Figure 5.7. The target pressure was set to be the initial reservoir pressure, 252 bar. When the lithology and cap rock stability are not examined, picking initial reservoir pressure is often a good choice to avoid possible CO_2 leakage. The injectors were constant rate injectors and the injection were terminated once reaching the target pressure.

It turned out that around 1.665 billion tonnes of CO_2 were injected when the target pressure was reached. 97.73% of the injected CO_2 was present in the gas zone, of which 98% existed as free gas. Whereas in the aquifer, around 75% of the CO_2 was stored through solubility trapping. In those grid blocks, the average CO_2 mass fraction was only about 1.16×10^{-4}, which was much lower than the equilibrium solubility. This demonstrates that the aquifer still had a great potential to store more CO_2. At the reservoir condition, water is denser than CO_2. In such circumstances, with no further pressurization of the reservoir, additional CO_2 can get into the aquifer through dispersion and diffusion only. Such a process could be very slow but may improve CO_2 storage. For example, keeping the same amount of CO_2 injection, if we extend the injection period or use cyclic injection, the reservoir pressure might be less than the target pressure.

Table 5.2 Major reservoir and fluid properties of VR115_PO

Parameters	**Value**
Original gas in place (OGIP) (m^3)	1.1015E+09
Cumulative gas production (m^3)	4.9554E+08
Cumulative water production (m^3)	5.6634E+06
Subsea depth (m)	2225
Gas zone average depth (m)	11.9
Total area (m^2)	1.6E+06
Porosity (frac.)	0.31

Table 5.2 continued

Residual water saturation (frac.)	0.16
Permeability (m^2)	1.23E-12
Initial Pressure (bar)	252
Initial Temperature (℃)	74
Total completions in the reservoir	6
Initial gas formation volume factor	0.044

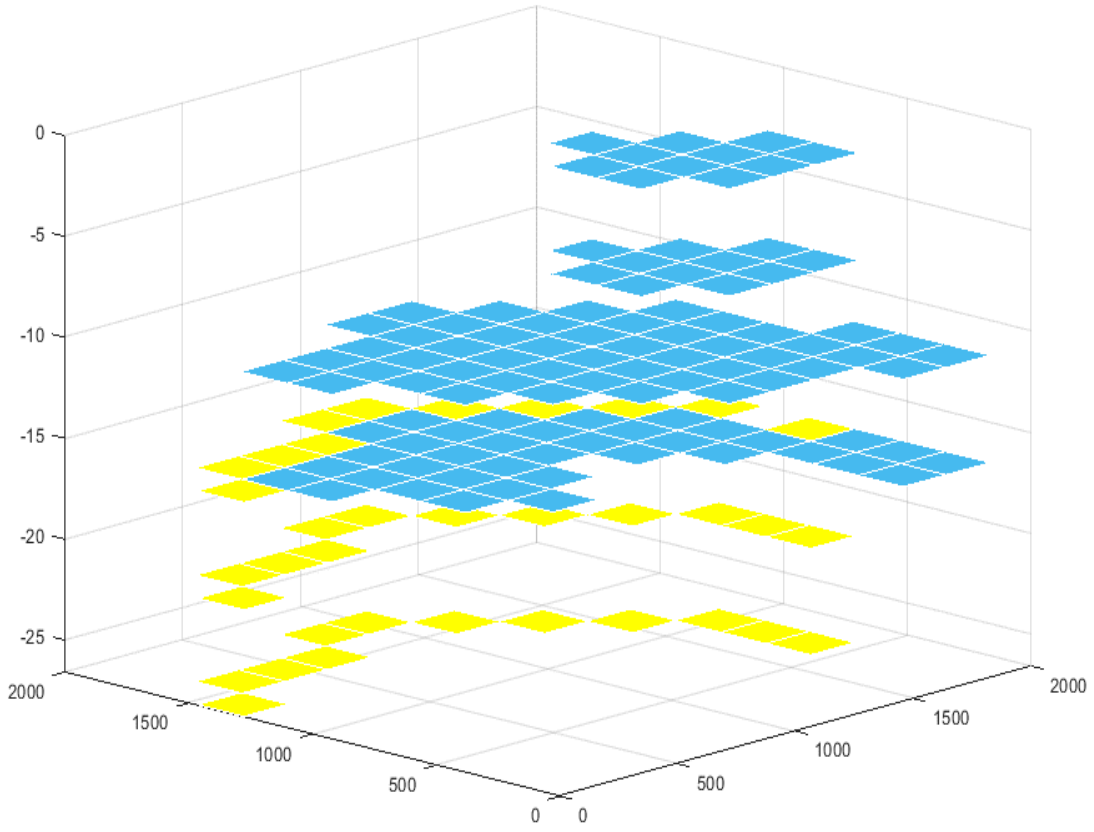

Figure 5.6 Schematic diagram of the reservoir model

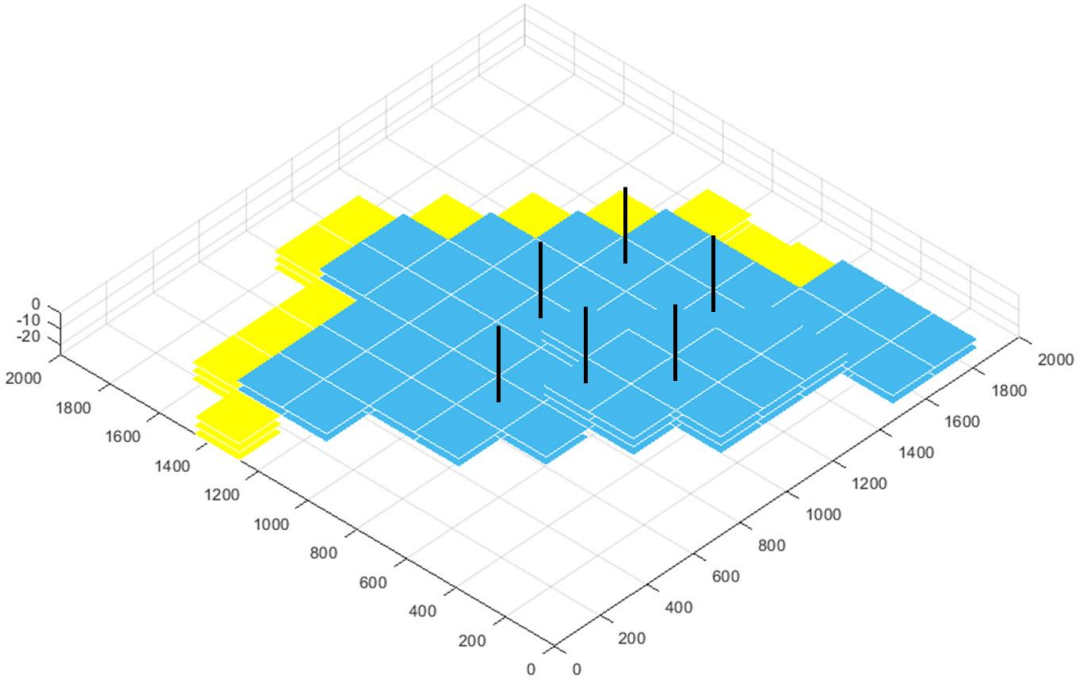

Figure 5.7 Location of the six injectors in the base case

Therefore two simulation runs were conducted to examine how different injection strategies affect the storage capacity. Scenario 1 used cyclic injection, in which the injection stopped after two years and then went back on. In scenario 2, the shut-in time was doubled. All these runs used the same reservoir and fluid properties in the base case, and the CO_2 injection rate remained the same. This time, as the injection rate stayed consistent with the base case, the injection period was adjusted so that it can reach the target reservoir pressure. The diffusion coefficients, which are nearly impossible to obtain, also remained identical to those in the base case.

The CO_2 storages in these two runs were compared with that in the base case, as given in Table 5.3. The results show that by using cyclic injections, the CO_2 storage increased, and a greater increase was achieved in Scenario 2. However, the improvements were very limited, at a level of million tonnes. Suppose that the improvement will become more significant if we further

extend the shut-in time or use multiple cycles. But this deviates from the original purpose which is to approach net zero in 2050 and remedy global temperature raising, let alone the additional operational cost.

Table 5.3 Comparison of the CO_2 injections in different scenarios

Scenario	**CO_2 injection (billion tonnes)**
Base case	1.6651
Scenario 1	1.6684
Scenario 2	1.6698

Another injection strategy that may improve the CO_2 injection is injecting CO_2 in deeper positions, which are close to or even below the gas-water contact. Thus, Scenario 3 and 4 were considered to investigate the effect of the injection depth on the CO_2 injection. Scenario 3 deepened the injections by a layer, while the injections remained in the gas zone, whereas Scenario 4 injected CO_2 directly into the aquifer (layer 5). In Scenario 4, the well locations were also completely changed, as given in Figure 3. Note in reality, these deep injection wells, especially those that penetrated into the aquifer, usually do not exist. These wells are generally repurposing existing producers, which are often set at the top of the gas zone.

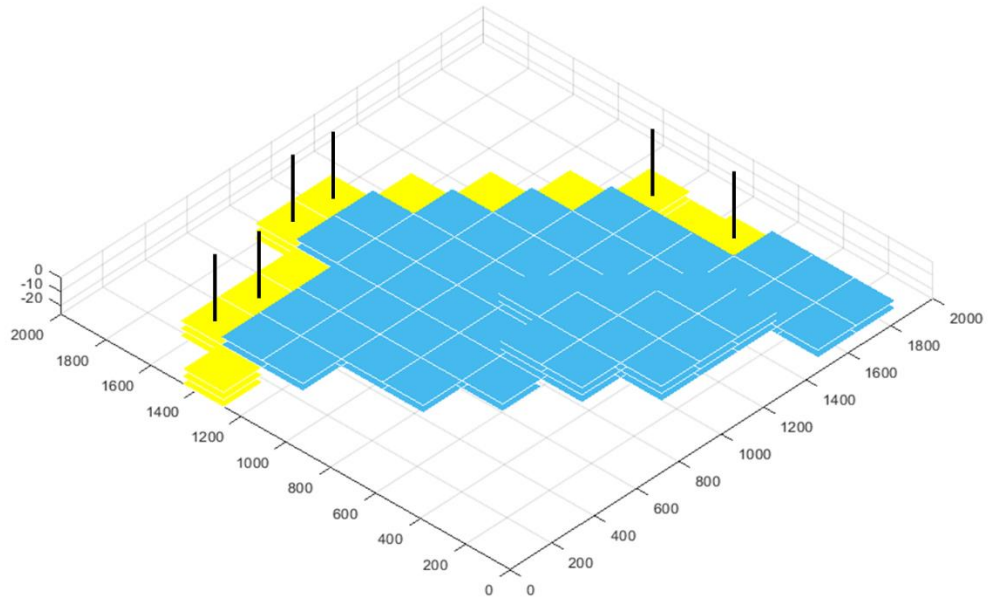

Figure 5.8 Injection well locations in Scenario 4.

Table 5.4 listed the final reservoir pressure and CO_2 distribution in the aquifer in the base case and Scenario 3 and 4. At the same CO_2 injection, the final reservoir pressure in Scenario 3 was only 0.1 bar lower than that in the base case, and a little more CO_2 was stored in the aquifer. Such a negligible difference does not worth the cost associated with the drilling operations. In Scenario 4, the final reservoir pressure was 232.37 bar, and a significant amount of CO_2 appeared in the aquifer. The gas zone only contained around 0.1 billion tonnes of CO_2, indicating that there still is a great capability of storing CO_2. Therefore, another simulation run (Scenario 5) was conducted, which increased the injection rate so that the target pressure can be reached.

When reaching the target pressure, the reservoir stored 1.93 billion tonnes of CO_2, which is 0.265 billion tonnes greater than the base case did. This demonstrates that injecting CO_2 from the bottom aquifer could improve CO_2 storage by making the most of the solubility trapping in the bottom aquifer. However, one should be aware that Scenario 5 is very ideal. First, the

geology and the shape of the aquifer were unknown, so the aquifer was simplified as a few large-volume water-rich grid blocks. In addition, it is well-recognized that using smaller grids and increasing the number of layers could improve the accuracy of the simulation, which is saying the result of Scenario 5 might not be accurate enough. Next, it was assumed that the CO_2 dissolution into brine obeys thermodynamic equilibrium, which may overestimate the dissolved CO_2 for each time step. This assumption is widely accepted and implemented for simulating CO_2 geo-storage. However, in Scenario 5, it might be problematic, because rather than immediately dissolving into the brine, the injected gas was more likely to result in gas channeling or fingering. Leaving aside these deviations from reality and the possible spending associated with drilling new wells, the results demonstrate that injecting CO_2 into the bottom aquifers could improve the CO_2 storage.

Table 5.4 Final reservoir pressure and CO_2 storage in the aquifer for the base case and Scenario 3 and 4

Scenario	**Final reservoir pressure (bar)**	**CO_2 stored in the aquifer (billion tonnes)**	**Overall CO_2 storage (billion tonnes)**
Base case	252.13	0.03779	1.6651
Scenario 3	252.01	0.03953	1.6651
Scenario 4	232.37	1.59045	1.6651
Scenario 5	252.06	1.78452	1.9343

5.3 CO_2 Storage and Enhanced Gas Recovery

The above modeling studies focused on sheer CO_2 storage in gas reservoirs, which did not involve any gas production. Here we present simulation studies on CSEGR. CSEGR has attracted increasing interest because it sequestrates CO_2 and at the same time withdraws remaining natural gas. CSEGR is very different from CO_2 storage because there is typically no significant increase in reservoir pressure, and CO_2 storage depends greatly on CO_2 breakthrough. Once CO_2 breaks through, it is believed that production is no longer beneficial since separating the gas mixture is costly.

A cuboid model that represents a quarter of the five-spot injection pattern was used. It had a dimension of 200 m×200 m×45 m, and it was discretized into 15×15×9 elements. All boundaries were closed boundaries and the bottom aquifer was ignored. Since there was no significant pressurization of the reservoir so the interaction between the gas zone and the aquifer was not as important as that for sheer storage. The reservoir was homogeneous with a porosity of 0.25 and permeabilities of 6×10^{-14} m^2, 6×10^{-14} m^2, and 6×10^{-15} m^2 in X, Y, and Z directions. Input parameters are detailed in Table 5.5. The CO_2 injector was set in layer 1 and the CO_2 was injected into the reservoir with a constant rate of 1 kg/s. The injection stopped when CO_2 broke through (CO_2 concentration exceeds 1% in the producer). The producer was a constant pressure producer with a bottom hole pressure of 35.5 bar and the well index was set 1×10^{-12} m^3/Pa s.

It turned out that around 11 MM tonnes of CO_2 was sequestrated and the additional gas recovery factor (AGRF), defined as the amount produced natural gas divided by remaining gas in place at depletion (kg/kg), was around 8.8%. It is well recognized that the CO_2 breakthrough depends greatly on the injection rate, thus affecting CO_2 storage and gas recovery. To quantify the influence, three simulations were conducted with an injection rate of 0.5, 0.2, and 0.1 kg/s. The results were compared in Table 5.6.

Table 5.5 Input parameter for CSEGR simulation run.

Parameters	**Value**
Rock density (kg/m^3)	2650
Rock specific heat (J/kg ˚C)	1000
Formation heat conductivity (W/m℃)	2.51
Porosity (frac.)	0.25
Residual water saturation (frac.)	0.16
Permeability (m^2) (I, J, K)	$6\times10^{-14}, 6\times10^{-14,}$ 6×10^{-15}
Initial Pressure (bar)	35.5
Initial Temperature (℃)	66.7
Initial gas saturation (frac.)	0.839
Initial gas formation volume factor	0.044

Table 5.6 summary of the results of simulations with different injection rates

Case #	**Injection rate** (kg/s)	**AGRF** (%)	**CO_2 breakthrough time** (day)	**CO_2 storage** (MM tonnes)
1 (base)	1	8.83	127.16	11.0
2	0.5	10.39	218.29	9.43
3	0.2	14.68	468.30	8.09
4	0.1	18.44	848.45	7.33

It can be seen that decreasing the injection rate could help produce more natural gas but reduce CO_2 storage. Similar results were also reported by Fan et al. (2021) and Liu et al. (2022). But in field operation, the time value and operational cost should be taken into account because using a lower injection rate does not only bring in higher recovery but also longer operations. For example, changing the injection rate from 0.2 to 0.1 kg/s could improve AGRF by 26% but

nearly double the operation time. Thereby an economic analysis might be needed for making the decisions.

Injection depth is another important factor that impacts the CO_2 breakthrough. The injected CO_2 typically moves downhill from the injection point due to gravity acceleration, functioning as cushion gas (Liu and Sun 2019). In such cases, the CO_2 flow path and migration depend strongly on the injection depth. The model contained 9 layers and as a consequence, additional 8 simulations were conducted, with the CO_2 injector set in different layers. The injection rate was 0.2 kg/s for all the simulations. The comparison of the results is given in Table 5.7.

Table 5.7 Comparison of the results of simulations with different injection depths.

Injection depth (layer #)	AGRF (%)	CO_2 storage (MM tonnes)
1	14.68	8.09
2	29.10	13.10
3	31.54	13.79
4	34.02	14.48
5	35.90	15.00
6	35.89	15.00
7	35.26	14.83
8	34.62	14.66
9	34.00	14.48

It shows that both gas recovery and CO_2 storage increase with the injection depth, but the turning point appears at layer 5 to layer 6 (more clearly in Figure 5.9). To better interpret the problem, the CO_2 concentration profile of the simulation with injection at layer 1, 3, 5, 7, and 9

are presented in Figure 5.10. It shows that for injection at layer 1, the CO_2 mostly displaces the CO_2 in the shallow areas and bypasses a large portion of the reservoir. As the injection depth increase, it seems that the CO_2 sweeps a larger volume because it sinks to the bottom layers and builds up as cushion gas to push the natural gas. Too deep injections, nevertheless, can be detrimental, leaving a large part of the shallower areas unswept.

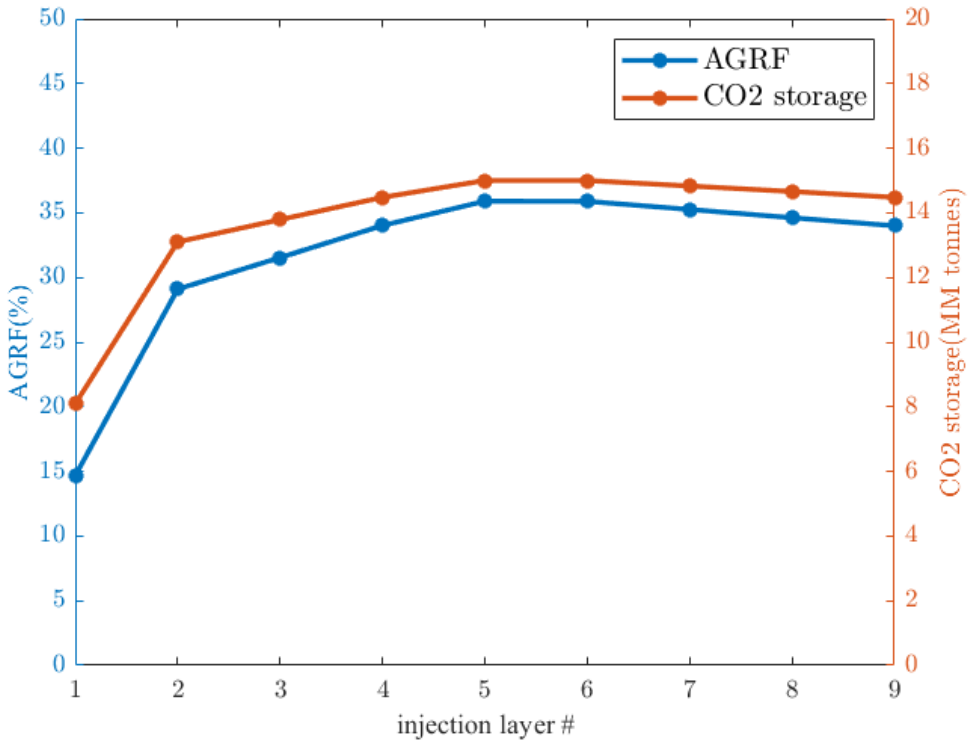

Figure 5.9 Additional gas recovery and CO_2 storage obtained from simulation with different injection depth.

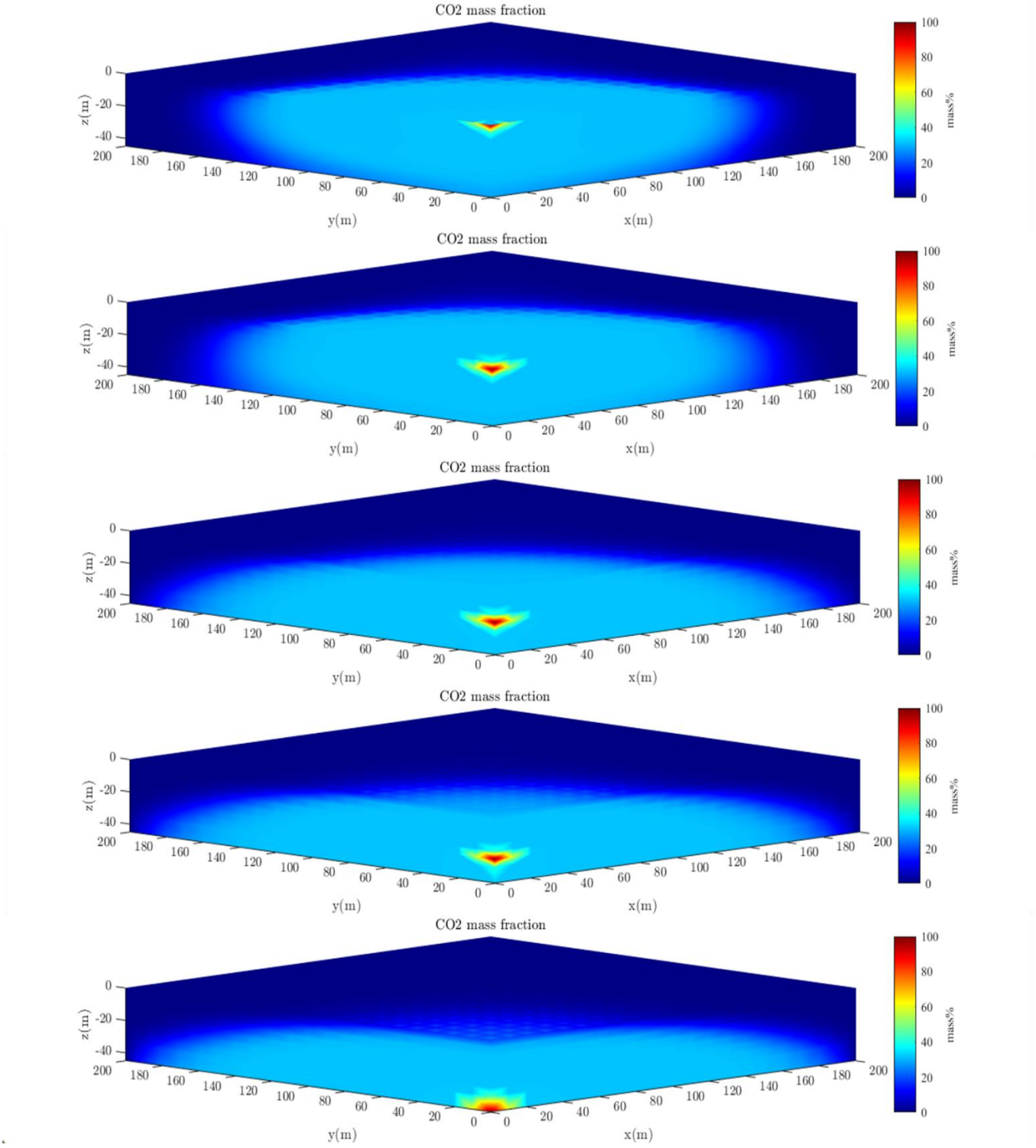

Figure 5.10 CO_2 concentration profile for simulations with different injection depths. For top to bottom: Layer 1, 3, 5, 7, 9.

Based on the results, it seems that injection at the middle layers could bring the best gas recovery and CO_2 storage. By continuing our study, we realize that the results also depend on the distance between the injector and producer, the injection rate, and the vertical permeability. Using the same setup but increasing the distance could reduce the difference caused by injection depth or even reverse the results completely. Similarly, keeping other parameters the same but reducing the injection rate could lead to the same results. In simple terms, changing the distance between the injector and producer or the injection rate gives the CO_2 opportunities to slowly migrates from the top to the bottom layers and sweep a larger volume than some deeper injections do. Therefore, it might be difficult to come up with a universal rule for optimizing injection depth, and it is on a case-to-case basis.

Table 5.8 Permeability values assigned to the layers for the heterogeneous reservoir

Layer #	Permeability in I and J (m^2)
1	6e-14
2	9e-14
3	9e-14
4	1e-14
5	1e-13
6	6e-13
7	4e-14
8	6e-15
9	1e-13

The above simulations assumed that the reservoir was homogeneous, in which case the CO_2 has no preference for going through any specific flow channel but forms a uniform displacement. In reality, the reservoirs are heterogeneous. The displacing CO_2 seeks the high

permeability channels to flow through and bypasses the low permeability regions (known as channeling). Thus, this time we assigned different permeability values to the layers to generate a heterogeneous reservoir as shown in Table 5.8. The permeability in the vertical direction was still one-tenth of the horizontal permeability.

Similar injection strategies were evaluated, first being injection rate and then the injection depth. Table 5.9 shows the results for injection at layer 1 with various injection rates. The results are very consistent with those for the homogeneous cases that AGRF increases and CO_2 storage decreases with injection rate. Next, simulations with different injection depths were conducted and the results are given in Table 5.10. This time the relationship becomes more complicated, which can be seen more clearly in Figure 5.11. Instead of having one turning point, it has two this time and the twists become more remarkable.

The reason for the sharp drop when changing the injection from layer 4 to 5 is quite obvious. Layer 5 has a higher permeability compared to the first four. Injecting at this layer even omitted the effort for CO_2 to find the high permeability channel. CO_2 is likely to flow through this channel and reach the producer rapidly. Therefore, one can imagine that the region swept by CO_2 should be very "flat" and thin. To verify this, the CO_2 concentration profiles of the first five cases are given in Figure 5.12. The swept region can be approximately reflected by the area marked in light blue. It turns out the high permeability layer 5 has effects on the displacement to varying degrees but for the first four cases the displacing CO_2 still covers a large portion in the upper layers. Whereas for case 5, the displacement mostly occurs in the thief zone.

The results of the last four cases are given in Figure 5.13. The permeability of layer 6 was even higher than that of layer 5, which explains why case 6 yielded the lowest AGRF and CO_2 storage. As we further deepened the injection, owing to the gravity drainage, CO_2, to a great extent, avoided flowing through the high permeability layers. This led to the dramatic upgoing

trend in Figure 5.11, especially for case 8 and 9. In those cases, CO_2 penetrated through the deeper layers and gradually builds up there until reaching the producer. It is worth noticing that layer 9 was also of a high permeability. However, due to gravity and the fact that vertical permeabilities were only one-tenth of the horizontal permeabilities, CO_2 could cover more area while migrating slowly from the bottom corner to the producer at the top.

Based on these results, one can conclude that reservoir heterogeneity plays an important role in determining the displacement pattern for CSEGR. In reality, the heterogeneity could be more server, especially when there are faults and fractures. In that case, the injection strategy needs to be picked with extreme care. The CO_2 injection should avoid the high permeability zones to maximize the gas recovery and CO_2 storage. Typically, injecting at the bottom layers is advisable.

Table 5.9 Results of simulations with different injection rates

Injection rate (kg/s)	AGRF (%)	CO_2 storage (MM tonnes)
1	7.50	8.35
0.5	10.24	7.14
0.2	14.64	6.48
0.1	17.47	5.94

Table 5.10 Results of simulation with different injection depths

Injection depth (layer #)	AGRF (%)	CO_2 storage (MM tonnes)
1	14.64	8.09
2	15.14	8.27
3	15.66	8.44

Table 5.10 Continued

4	15.64	8.44
5	11.69	7.06
6	11.22	6.88
7	11.69	7.06
8	16.10	8.61
9	21.52	10.31

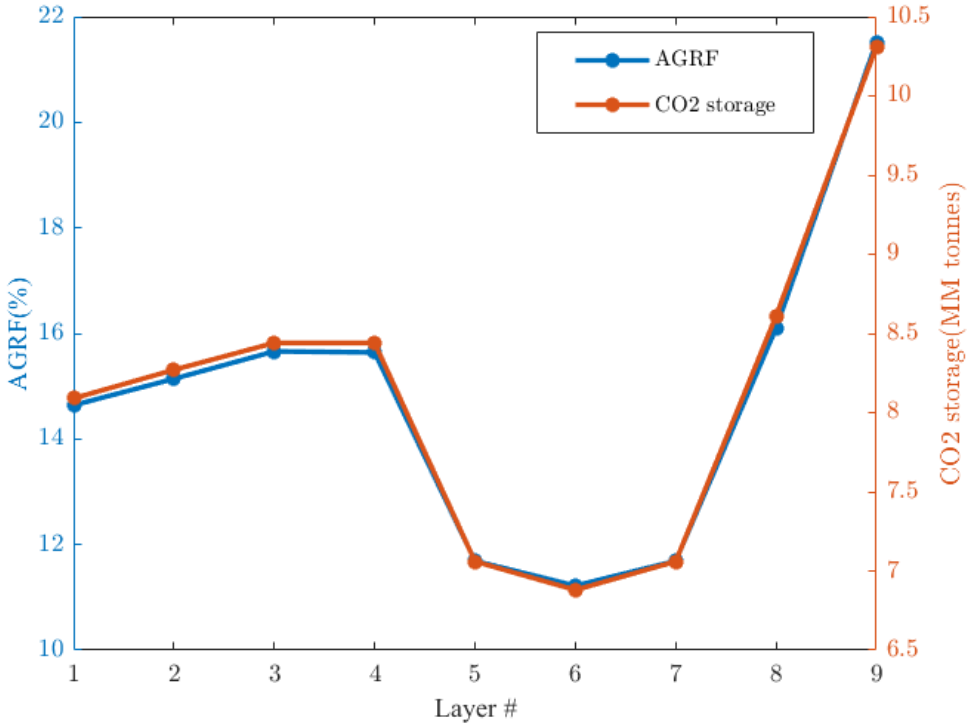

Figure 5.11 Additional gas recovery and CO_2 storage obtained from simulation with different injection depth for the heterogeneous case

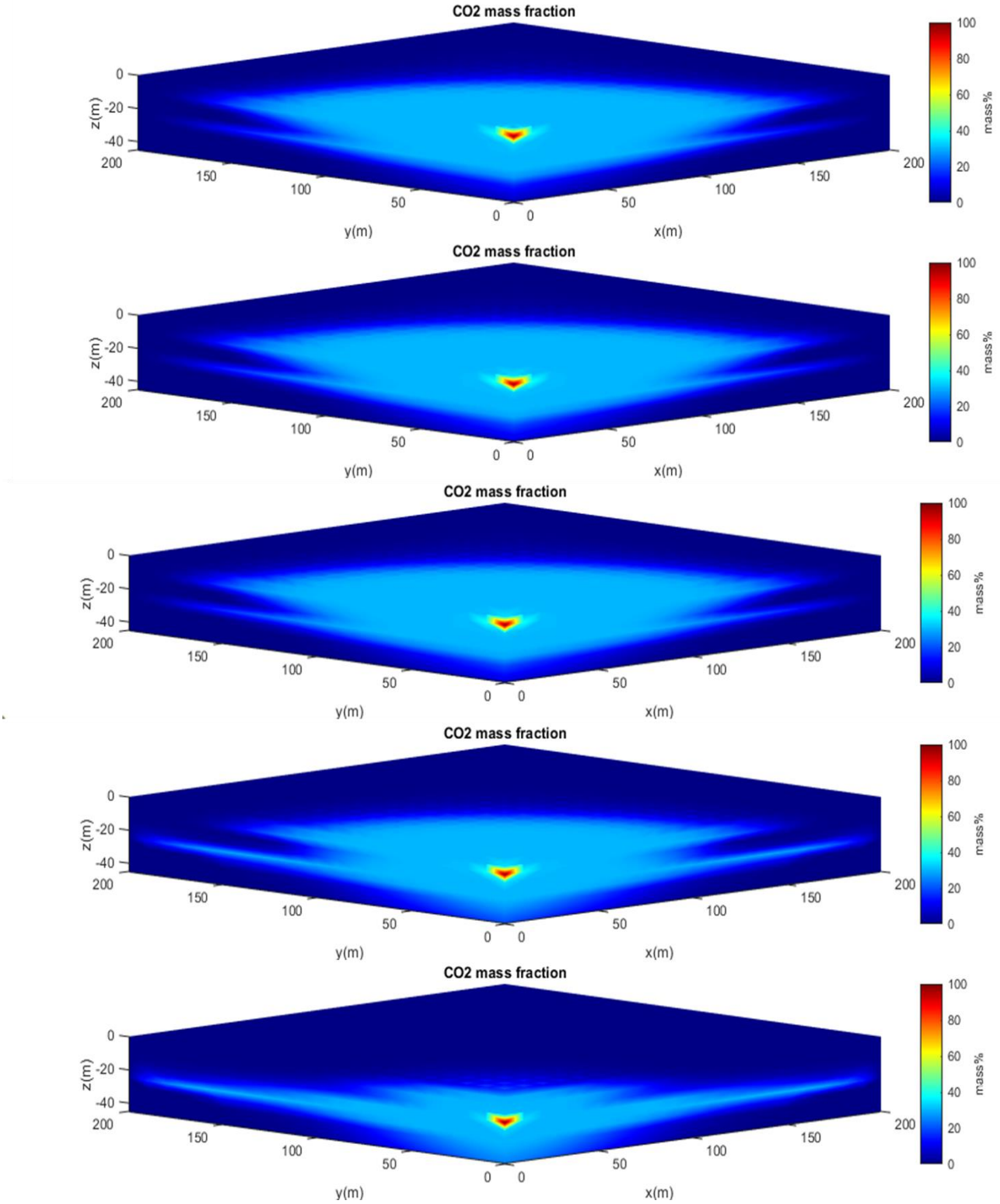

Figure 5.12 CO_2 concentration distribution for (from top to bottom) case 1 to 5.

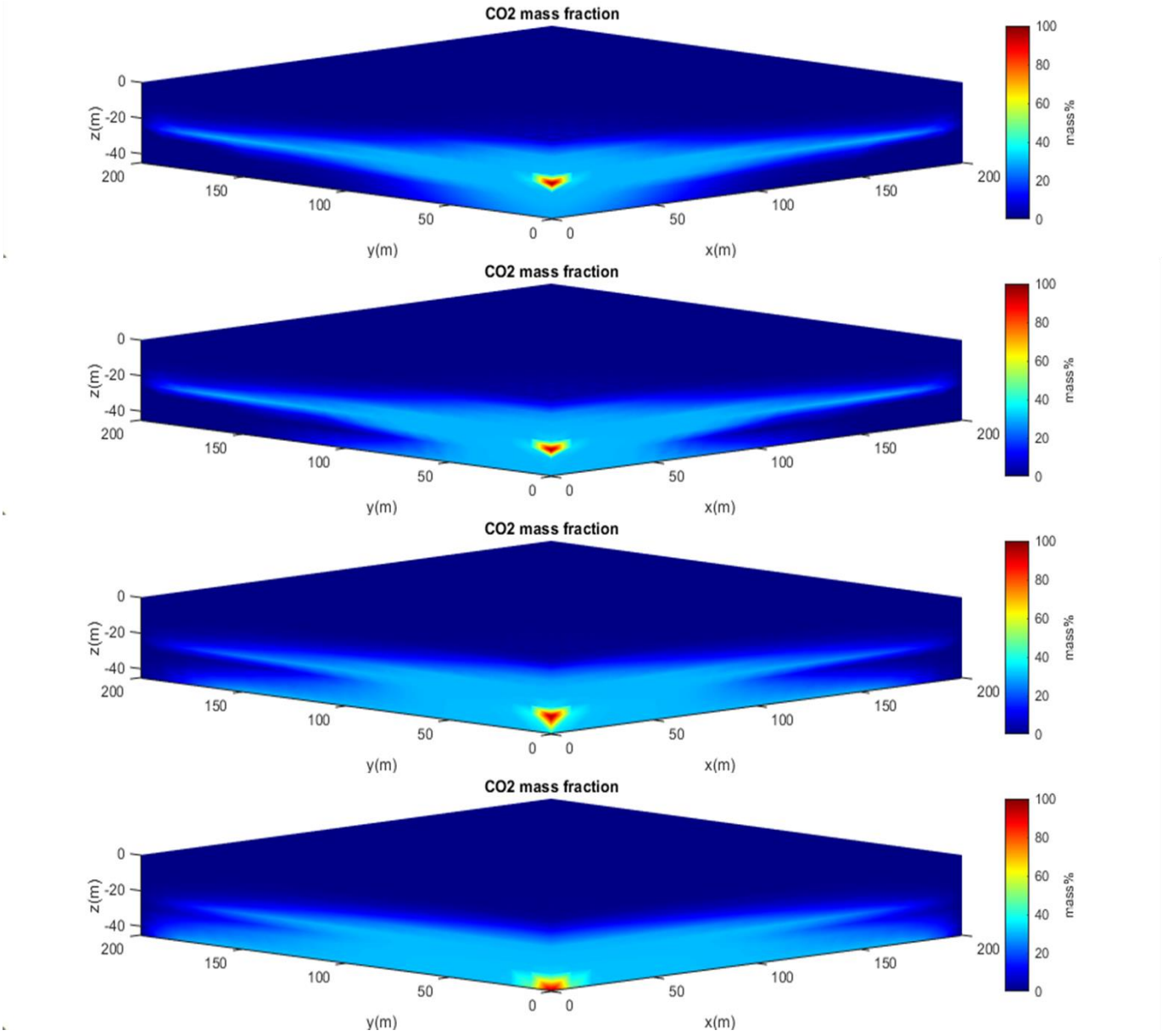

Figure 5.13 CO_2 concentration distribution for (from top to bottom) case 6 to 9.

CHAPTER 6

CONCLUSIONS AND RECOMMENDATIONS

6.1 Summary and Contribution

In this dissertation, an EOS module is developed to model CO_2 geological sequestration in gas reservoirs, which can handle up to six components including water, NaCl, CO_2, and three light hydrocarbon components (C_1 to C_3). The module calculates mutual solubilities in water-hydrocarbon gas-CO_2 using fugacity and Henry's constant, while considering activity coefficients to account for the salting out effect when NaCl is present. The parameters used to calculate Henry's constant and activity coefficients are calibrated based on either experimental or generated data using correlations. Additionally, the module can calculate the thermodynamic properties of both real gas mixtures and aqueous solutions.

The developed EOS module can be integrated into TOUGH2-CSM to enable fully coupled THM modeling for CO_2 geo-sequestration in gas reservoirs. This integration allows for accurate prediction of reservoir pressurization, which is crucial for preventing cap rock instability. The capability of handling more realistic natural gas composition provides more precise estimations of storage capacity and gas recovery compared to models that assume natural gas as pure methane. Additionally, the framework is easily extendable to include more elements for simulating other processes, such as waste gas EGR, with minimal effort.

6.2 Conclusion

The dissertation includes various numerical modeling studies that investigate CO_2 storage in gas reservoirs and CSEGR. The first study compares the results of simulations using the THM option, TH option, and TH option that only considered C_1. The comparison shows that including geomechanics and considering hydrocarbon compositions beyond C_1 can improve the accuracy of predictions, particularly for reservoir pressure. Accurate predictions of pressure are crucial as

they directly impact storage capacity and reservoir integrity. Therefore, including geomechanics and a more realistic composition can be advantageous for simulations.

The next focuses on CO_2 storage in VR115_PO, a depleted gas sand in the Gulf of Mexico and investigated the injection strategies. The following conclusion can be drawn from that:

1. CO_2 storage is primarily determined by the target pressure (or threshold pressure), while the injection strategies include injection rate, cyclic injection, and injection depth have minimum impact.
2. Injecting deep into the bottom aquifer was found to be beneficial, as it maximizes the solubility trapping effect provided by the aquifer, resulting in a 20% increase in CO_2 storage capacity in this particular case.

In the final study, a cuboid model that represents a quarter of the five-spot well pattern is utilized to simulate CSEGR in depleted gas reservoirs. The study examines injection strategies such as injection rate and depth and evaluates their impact on CO_2 storage and gas recovery. Both homogeneous and heterogeneous (in permeability) models are utilized in the investigation. The key findings are presented below. It is important to note that these conclusions are relevant only to particular or similar model configurations and may not be generalizable to other setups.

1. A greater CO_2 storage is typically accompanied by a higher recovery factor because more CO_2 storage means a larger swept area.
2. The injection strategy has a great impact on gas recovery and CO_2 storage by deciding the displacement pattern.
3. If economically feasible, a low injection rate is preferred to avoid the early breakthrough of CO_2.

4. In this simulation study, CO_2 storage and recovery factor increase with the injection depth, and the peak shows at the intermediate depth. However, the results may vary from case to case, depending on the distance between injector and producer, vertical permeability, injection rate, and any other that determines the horizontal and vertical migrations of the displacing CO_2.
5. The reservoir heterogeneity brings more uncertainties to optimizing the injection depth. The high permeability channels could cause an early breakthrough of the injected CO_2, and thus the injection should avoid these thief zones.

6.2 Recommendations

There are a number of potential studies that are needed for future research efforts. and they are listed as follows:

1. Our work currently focuses on CO_2 storage in conventional gas reservoirs. further work is required to extend this approach to include modeling for storage in unconventional sources. This will involve developing additional subroutines to account for factors such as adsorption
2. Expanding our research to encompass additional chemical species, such as H_2S, N_2, and O_2, would allow us to address the presence of impurities in hydrocarbon gas, or to simulate waste gas EGR.
3. The EOS module has been integrated into the serial version of TOUGH2-CSM. It can be adopted in the parallel version that runs on a high-performance computing cluster (HPC) to improve the computation time.
4. The model can be verified or benchmarked with commercial software ECLIPSE 300^{TM}, which allows more than C_1 for the natural gas composition.

5. To expand the scope of our field case study, we could include additional depleted gas reservoirs in the Gulf of Mexico and beyond. Using advanced preprocessing tools, such as Wingrider, we could generate complex grid systems to evaluate storage capacity and optimize injection strategies more accurately.

REFERENCES

Afanasyev, A. A. 2013. Application of the reservoir simulator MUFITS for 3D modelling of CO_2 storage in geological formations. *Energy Procedia*, 40, 365-374.

Agartan, E., Gaddipati, M., Yip, Y., Savage, B. et al. 2018. CO_2 storage in depleted oil and gas fields in the Gulf of Mexico. *International Journal of Greenhouse Gas Control*, *72*, 38-48.

Alfarge, D., Wei, M., and Bai, B. 2017. Factors affecting CO_2-EOR in shale-oil reservoirs: numerical simulation study and pilot tests. *Energy and Fuels*, **31**(8), 8462-8480.

Alley, W. E., and Alder, B. J. 1979. Modification of Fick's law. *Physical Review Letters*, **43**(10), 653.

Andersen, G., A. Probst, L. Murray and S. Butler. An Accurate PVT Model for Geothermal Fluids as Represented by H_2O-NaCl- CO_2 Mixtures, Proceedings 17th Workshop on Geothermal Reservoir Engineering, pp. 239 - 248, Stanford, CA, 1992.

Armero, F., and Simo, J. C. 1992. A new unconditionally stable fractional step method for non-linear coupled thermomechanical problems. *International Journal for numerical methods in Engineering*, **35**(4), 737-766.

Bachu, S., Gunter, W. D., and Perkins, E. H. 1994. Aquifer disposal of CO_2: hydrodynamic and mineral trapping. *Energy Conversion and management*, **35**(4), 269-279.

Balashov, V. N., Guthrie, G. D., Hakala, J. A. et al. 2013. Predictive modeling of CO_2 sequestration in deep saline sandstone reservoirs: Impacts of geochemical kinetics. *Applied Geochemistry*, 30, 41-56.

Battino, R. 1983. Giant atomic and molecular models and other lecture demonstration devices designed for concrete operational students. *Journal of Chemical Education*, **60**(6), 485.

Ben-Naim, A., and Yaacobi, M. 1974. Effects of solutes on the strength of hydrophobic interaction and its temperature dependence. The Journal of Physical Chemistry, **78**(2), 170-175.

Cantucci, B., Montegrossi, G., Vaselli, O. et al. 2009. Geochemical modeling of CO_2 storage in deep reservoirs: The Weyburn Project (Canada) case study. *Chemical Geology*, **265**(1-2), 181-197.

Cappa, F., and Rutqvist, J. 2011a. Modeling of coupled deformation and permeability evolution during fault reactivation induced by deep underground injection of CO_2. *International Journal of Greenhouse Gas Control*, **5**(2), 336-346.

Cappa, F., and Rutqvist, J. 2011b. Impact of CO_2 geological sequestration on the nucleation of earthquakes. *Geophysical research letters*, **38**(17).

Celia, M. A., Bachu, S., Nordbotten, J. M. et al. 2015. Status of CO_2 storage in deep saline aquifers with emphasis on modeling approaches and practical simulations. *Water Resources Research*, **51**(9), 6846-6892.

Chapoy, A., Mokraoui, S., Valtz, A. et al. 2004. Solubility measurement and modeling for the system propane–water from 277.62 to 368.16 K. *Fluid Phase Equilibria*, 226, 213-220.

Chen, H. Y., and Teufel, L. W. 2000. Coupling fluid-flow and geomechanics in dual-porosity modeling of naturally fractured reservoirs-model description and comparison. Presented at SPE International Petroleum Conference and Exhibition in Mexico.

Cheng, L., Luo, Z., Zhao, L. et al. 2022. Numerical analysis of fracture deformation and instability during CO_2 geological sequestration using a THM-XFEM coupled model. *Computers and Geotechnics*, 145, 104664.

Chou, L. E. I., Garrels, R. M., and Wollast, R. 1989. Comparative study of the kinetics and mechanisms of dissolution of carbonate minerals. *Chemical geology*, **78**(3-4), 269-282.

Class, H., Ebigbo, A., Helmig, R. et al. 2009. A benchmark study on problems related to CO_2 storage in geologic formations. *Computational geosciences*, **13**(4), 409-434.
Clever, H. L., Baker, E. R., and Hale, W. R. 1970. Solubility of ethylene in aqueous silver nitrate and potassium nitrate solutions. Silver ion-ethylene association constant. *Journal of Chemical and Engineering Data*, **15**(3), 411-413.

Collins, D. A., Nghiem, L. X., Li, Y. K., and Grabonstotter, J. E. 1992. An efficient approach to adaptive-implicit compositional simulation with an equation of state. *SPE reservoir engineering*, **7**(02), 259-264.

Credoz, A., Bildstein, O., Jullien, M. et al. 2009. Experimental and modeling study of geochemical reactivity between clayey caprocks and CO_2 in geological storage conditions. *Energy Procedia*, **1**(1), 3445-3452.

Crovetto, R., Fernández-Prini, R., and Japas, M. L. 1982. Solubilities of inert gases and methane in H_2O and in D_2O in the temperature range of 300 to 600 K. *The Journal of Chemical Physics*, **76**(2), 1077-1086.

Cui, G., Zhu, L., Zhou, Q., Ren, S. et al. 2021. Geochemical reactions and their effect on CO_2 storage efficiency during the whole process of CO_2 EOR and subsequent storage. International Journal of Greenhouse Gas Control, 108, 103335.

Czerski, L., and Czapliński, A. 1962. Solubility of ethane in water and NaCl and $CaCl_2$ solutions at 0.0 C and pressure above 1 at. Rocz. Chem. Ann. Soc. Chim. Polonorum, 36, 1827-1834.

Dana, S., and Jha, B. 2021. A fault slip model to study earthquakes due to pore pressure perturbations. arXiv preprint arXiv:2104.06257.

De Silva, G. P. D., Ranjith, P. G., and Perera, M. S. A. 2015. Geochemical aspects of CO_2 sequestration in deep saline aquifers: A review. *Fuel*, 155, 128-143.

Desai, C. S. 1980. A general basis for yield, failure and potential functions in plasticity. *International Journal for Numerical and Analytical Methods in Geomechanics*, **4**(4), 361-375.

Duan, Z., and Sun, R. 2003. An improved model calculating CO_2 solubility in pure water and aqueous NaCl solutions from 273 to 533 K and from 0 to 2000 bar. *Chemical geology*, **193**(3-4), 257-271.

Ennis-King, J., Dance, T., Xu, J. et al. 2011. The role of heterogeneity in CO_2 storage in a depleted gas field: history matching of simulation models to field data for the CO_2CRC Otway Project, Australia. *Energy Procedia*, 4, 3494-3501.

Errington, J. R., Boulougouris, G. C., Economou, I. G. et al. (1998). Molecular simulation of phase equilibria for water− methane and water− ethane mixtures. *The Journal of Physical Chemistry B*, ***102***(44), 8865-8873.

Esene, C., Zendehboudi, S., Aborig, A. et al. 2019. A modeling strategy to investigate carbonated water injection for EOR and CO_2 sequestration. *Fuel*, 252, 710-721.

Eucken, A., and Hertzberg, G. 1950. Aussalzeffekt und ionenhydratation. Zeitschrift für Physikalische Chemie, **195**(1), 1-23.

Fan, L., Tan, Q., Li, H., Xu, J., Wang, X., and Liu, S. 2021. Simulation on effects of injection parameters on CO_2 enhanced gas recovery in a heterogeneous natural gas reservoir. *Advanced Theory and Simulations*, **4**(8), 2100127.

Garcia, J. E. 2001. Density of aqueous solutions of CO_2 (No. LBNL-49023). Lawrence Berkeley National Lab.(LBNL), Berkeley, CA (United States).

Gasda, S. E., Nordbotten, J. M., and Celia, M. A. 2009. Vertical equilibrium with sub-scale analytical methods for geological CO_2 sequestration. *Computational Geosciences*, **13**(4), 469-481.

Gastine, M., Berenblyum, R., Czernichowski-Lauriol, I. et al. 2017. Enabling onshore CO_2 storage in Europe: Fostering international cooperation around pilot and test sites. *Energy Procedia*, 114, 5905-5915.

Gaus, I. 2010. Role and impact of CO_2–rock interactions during CO_2 storage in sedimentary rocks. *International journal of greenhouse gas control*, ***4***(1), 73-89.

Gaus, I., Le Guern, C., Pearce, J. et al. 2005. Comparison of long-term geochemical interactions at two natural CO_2-analogues: Montmiral (Southeast Basin, France) and Messokampos (Florina Basin, Greece) case studies. *In Greenhouse Gas Control Technologies* **7** (pp. 561-569).

Ge, S., and Garven, G. 1992. Hydromechanical modeling of tectonically driven groundwater flow with application to the Arkoma foreland basin. *Journal of Geophysical Research: Solid Earth*, **97**(B6), 9119-9144.

Godec, M., Koperna, G., Petrusak, R. et al. 2013. Assessment of factors influencing CO_2 storage capacity and injectivity in Eastern US Gas Shales. *Energy Procedia*, 37, 6644-6655.

Gunter, W. D., Mavor, M. J., and Robinson, J. R. 2005. CO_2 storage and enhanced methane production: field testing at Fenn-Big Valley, Alberta, Canada, with application. *In Greenhouse Gas Control Technologies* **7** (pp. 413-421).

Gutierrez, M., Lewis, R. W., and Masters, I. 2001. Petroleum reservoir simulation coupling fluid flow and geomechanics. *SPE Reservoir Evaluation and Engineering*, **4**(03), 164-172.

Haas, J. L. 1976. Physical properties of the coexisting phases and thermochemical properties of the H_2O component in boiling NaCl solutions. *US Geol. Surv. Bull*., 1421, 1-73.

Haase, C., Dethlefsen, F., Ebert, M. et al. 2013. Uncertainty in geochemical modelling of CO_2 and calcite dissolution in NaCl solutions due to different modelling codes and thermodynamic databases. *Applied geochemistry*, 33, 306-317.

Han, W. S., McPherson, B. J., Lichtner, P. C. et al. 2010. Evaluation of trapping mechanisms in geologic CO2 sequestration: Case study of SACROC northern platform, a 35-year CO_2 injection site. *American Journal of Science*, **310**(4), 282-324.

Han, W. S., Stillman, G. A., Lu, M. et al. 2010. Evaluation of potential nonisothermal processes and heat transport during CO_2 sequestration. *Journal of Geophysical Research: Solid Earth*, **115**(B7).

Hannis, S., Lu, J., Chadwick, A. et al. 2017. CO_2 storage in depleted or depleting oil and gas fields: what can we learn from existing projects?. *Energy Procedia*, 114, 5680-5690.

Hoad, D. 2015. Reflections on small island states and the international climate change negotiations (COP21, Paris, 2015). *Island Studies Journal*, **10**(2), 259-262.

Hosseini, S. A., Lashgari, H., Choi, J. W. et al. 2013. Static and dynamic reservoir modeling for geological CO_2 sequestration at Cranfield, Mississippi, USA. *International Journal of Greenhouse Gas Control*, 18, 449-462.

Hoteit, H., Fahs, M., and Soltanian, M. R. 2019. Assessment of CO_2 injectivity during sequestration in depleted gas reservoirs. *Geosciences*, **9**(5), 199.

Intergovernmental Panel on Climate Change. 2018. Global warming of 1.5° C: An IPCC special report on the impacts of global warming of 1.5° C above pre-industrial levels and related global greenhouse gas emission pathways, in the context of strengthening the global response to the threat of climate change, sustainable development, and efforts to eradicate poverty. Intergovernmental Panel on Climate Change.

Jaynes, D. B., and Rogowski, A. S. 1983. Applicability of Fick's law to gas diffusion. *Soil Science Society of America Journal*, **47**(3), 425-430.

Jeannin, L., Mainguy, M., Masson, R. et al. 2007. Accelerating the convergence of coupled geomechanical-reservoir simulations. *International journal for numerical and analytical methods in geomechanics*, **31**(10), 1163-1181.

Jha, B., and Juanes, R. 2014. Coupled multiphase flow and poromechanics: A computational model of pore pressure effects on fault slip and earthquake triggering. *Water Resources Research*, **50**(5), 3776-3808.

Jin, M., Somerville, J., and Smart, B. G. D. 2000. Coupled reservoir simulation applied to the management of production induced stress-sensitivity. Paper presented at International Oil and Gas Conference and Exhibition in China.

Jossi, J. A., Stiel, L. I., and Thodos, G. 1962. The viscosity of pure substances in the dense gaseous and liquid phases. *AIChE Journal*, **8**(1), 59-63.

Kelemen, Peter B., Sally M. Benson., Hélène Pilorgé. Et al. 2019 “An Overview of the Status and Challenges of CO_2 Storage in Minerals and Geological Formations,” Frontiers in Climate, November 2019. https://doi.org/10.3389/fclim.2019.00009

Khan, C., Amin, R., and Madden, G. 2012. Economic modelling of CO_2 injection for enhanced gas recovery and storage: a reservoir simulation study of operational parameters. *Energy and Environment Research*, **2**(2), 65-82.

Kim, J., Tchelepi, H. A., and Juanes, R. 2011a. Stability and convergence of sequential methods for coupled flow and geomechanics: Fixed-stress and fixed-strain splits. *Computer Methods in Applied Mechanics and Engineering*, **200**(13-16), 1591-1606.

Kim, J., Tchelepi, H. A., and Juanes, R. 2011b. Stability, accuracy, and efficiency of sequential methods for coupled flow and geomechanics. *SPE Journal*, **16**(02), 249-262.

Kim, J., Tchelepi, H. A., and Juanes, R. 2013. Rigorous coupling of geomechanics and multiphase flow with strong capillarity. *SPE journal*, **18**(06), 1123-1139.

King, M. B., Mubarak, A., Kim, J. D. et al. 1992. The mutual solubilities of water with supercritical and liquid carbon dioxides. *The Journal of Supercritical Fluids*, **5**(4), 296-302.

Kobayashi, R., and Katz, D. 1953. Vapor-liquid equilibria for binary hydrocarbon-water systems. *Industrial and Engineering Chemistry*, **45**(2), 440-446.

Kresheck, G. C., Schneider, H., and Scheraga, H. A. 1965. The effect of D_2O on the thermal stability of proteins. Thermodynamic parameters for the transfer of model compounds from H_2O to D_2O[1,2]. *The Journal of physical chemistry*, **69**(9), 3132-3144.

Lasaga, A. C., Soler, J. M., Ganor, J. et al. 1994. Chemical weathering rate laws and global geochemical cycles. *Geochimica et Cosmochimica Acta*, **58**(10), 2361-2386.

Leal, A. 2020. Reaktoro: a unified open-source framework for modeling chemically reactive systems. In Rock-Water Interaction Seminar, University of Bern.

Leal, A. M., Kulik, D. A., and Kosakowski, G. 2016. Computational methods for reactive transport modeling: A Gibbs energy minimization approach for multiphase equilibrium calculations. *Advances in Water Resources*, 88, 231-240.

Leal, A., Volpatto, D., and Kyas, S. 2019. Reactive transport simulation in porous media using Firedrake and Reaktoro. In Online Abstract: Firedrake Workshop 2019. Firedrake.

Lei, H., Xu, T., and Jin, G. 2015. TOUGH2Biot–A simulator for coupled thermal–hydrodynamic–mechanical processes in subsurface flow systems: Application to CO_2 geological storage and geothermal development. *Computers and Geosciences*, 77, 8-19.

Li, J., Wei, L., and Li, X. 2014. Modeling of CO_2-CH_4-H_2S-brine based on cubic EOS and fugacity-activity approach and their comparisons. *Energy Procedia*, 63, 3598-3607.

Li, X., Xu, R., Wei, L. et al. 2015. Modeling of wellbore dynamics of a CO_2 injector during transient well shut-in and start-up operations. *International Journal of Greenhouse Gas Control*, 42, 602-614.

Li, Y. K., and Nghiem, L. X. 1986. Phase equilibria of oil, gas and water/brine mixtures from a cubic equation of state and Henry's law. *The Canadian Journal of Chemical Engineering*, **64**(3), 486-496.

Lindeberg, E., and Bergmo, P. 2003. The long-term fate of CO_2 injected into an aquifer. *Greenhouse gas control technologies*, 1, 489-494.

Liu, D., Li, Y., Song, S. et al. 2016. Simulation and analysis of lithology heterogeneity on CO_2 geological sequestration in deep saline aquifer: a case study of the Ordos Basin. *Environmental Earth Sciences*, **75**(11), 1-13.

Liu, S., and Sun, B. 2019. Numerical Simulation of CO_2 Enhanced Gas Recovery (CO_2-EGR) for The Optimal Perforation Position.

Liu, S., Agarwal, R., and Sun, B. 2022. Numerical Simulation and Optimization of CO_2-Enhanced Gas Recovery in Homogeneous and Vertical Heterogeneous Reservoir Models. *Journal of Energy Resources Technology*, **144**(3).

Lorenz, S., Maric, D., and Rirschl, C. 2000. Eine analytische Funktion zur Bestimmung der Enthalpie wässriger NaCl Lösungen, draft report. *Institut für Sicherheitstechnologie, Köln, Germany*.

Lu, M., and Connell, L. D. 2008. Non-isothermal flow of carbon dioxide in injection wells during geological storage. *International journal of greenhouse gas control*, **2**(2), 248-258.

Lucia, A., Henley, H., and Thomas, E. 2015. Multiphase equilibrium flash with salt precipitation in systems with multiple salts. *Chemical Engineering Research and Design*, 93, 662-674.

Mainguy, M., and Longuemare, P. 2002. Coupling fluid flow and rock mechanics: formulations of the partial coupling between reservoir and geomechanical simulators. *Oil and Gas Science and Technology*, **57**(4), 355-367.

Mathias, S. A., Hardisty, P. E., Trudell, M. R. et al. 2009. Screening and selection of sites for CO_2 sequestration based on pressure buildup. *International Journal of Greenhouse gas control*, **3**(5), 577-585.

McKee, C. R., Bumb, A. C., and Koenig, R. A. 1988. Stress-dependent permeability and porosity of coal and other geologic formations. *SPE formation evaluation*, **3**(01), 81-91.

Miah, M., Blanco-Martín, L., Foxall, W. et al. 2015. Development of a hydro-geomechanical model to simulate coupled fluid flow and reservoir geomechanics. In Proceedings of the TOUGH Symposium.

Michael, K., Allinson, G., Golab, A., Sharma, S. et al. 2009. CO_2 storage in saline aquifers II–experience from existing storage operations. *Energy Procedia*, **1**(1), 1973-1980.

Mishnina, T. A., Avdeeva, O. I., and Bozhovskaya, T. K. 1961. Materialy Vses. *Nauchn-Issled Geol Inst*, 46, 93-110.

Morrison, T. J., and Billett, F. 1952. 730. The salting-out of non-electrolytes. Part II. The effect of variation in non-electrolyte. *Journal of the Chemical Society* (Resumed), 3819-3822.

Narasimhan, S., Natarajan, G. S., and Nageshwar, G. D. 1981. Solubilities of Ethene, Propene and 2-Methylpropene in Normal Alcohols. *INDIAN JOURNAL OF TECHNOLOGY*, **19**(7), 298-299.

Narinesingh, J., and Alexander, D. 2014. CO_2 enhanced gas recovery and geologic sequestration in condensate reservoir: a simulation study of the effects of injection pressure on condensate recovery from reservoir and CO_2 storage efficiency. *Energy Procedia*, 63, 3107-3115.

Negredo, A. M., Bird, P., Sanz de Galdeano, C. et al. 2002. Neotectonic modeling of the Ibero-Maghrebian region. Journal of Geophysical Research: *Solid Earth*, **107**(B11), ETG-10.

Neto, M. A. M., and Barbosa Jr, J. R. 2013. A departure-function approach to calculate thermodynamic properties of refrigerant-oil mixtures. *International journal of refrigeration*, **36**(3), 972-979.

Nghiem, L., Sammon, P., Grabenstetter, J. et al. 2004. Modeling CO_2 storage in aquifers with a fully-coupled geochemical EOS compositional simulator. Paper presented at SPE Improved Oil Recovery Conference (pp. SPE-89474).

Nordbotten, J. M., Celia, M. A., and Bachu, S. 2005. Injection and storage of CO_2 in deep saline aquifers: Analytical solution for CO_2 plume evolution during injection. *Transport in Porous media*, **58**(3), 339-360.

Oldenburg, C. M. 2007. Joule-Thomson cooling due to CO_2 injection into natural gas reservoirs. *Energy Conversion and Management*, **48**(6), 1808-1815.

Oldenburg, C. M., Moridis, G. J., Spycher, N. et al. 2004. EOS7C Version 1.0: TOUGH2 Module for Carbon Dioxide or Nitrogen in Natural Gas (Methane) Reservoirs (No. LBNL-56589). Lawrence Berkeley National Lab.(LBNL), Berkeley, CA (United States).

Omar, A. A., Addassi, M., Hoteit, H. et al. 2021. A new enhanced gas recovery scheme using carbonated water and supercritical CO_2. In Proceedings of the 15th Greenhouse Gas Control Technologies Conference (pp. 15-18).

Ostensen, R. W. 1986. The effect of stress-dependent permeability on gas production and well testing. *SPE Formation Evaluation*, *1*(03), 227-235.

Paksoy, H. Ö. 2022. Energy Storage Can Stop Global Warming. Advances in Energy Storage: Latest Developments from RandD to the Market, 761-774.

Palandri, J. L., and Kharaka, Y. K. 2004. A compilation of rate parameters of water-mineral interaction kinetics for application to geochemical modeling. Geological Survey Menlo Park CA.

Pan, L., Oldenburg, C. M., Pruess, K. et al. 2011. Transient CO_2 leakage and injection in wellbore-reservoir systems for geologic carbon sequestration. *Greenhouse Gases: Science and Technology*, **1**(4), 335-350.

Pandey, S. N., Vishal, V., and Chaudhuri, A. 2018. Geothermal reservoir modeling in a coupled thermo-hydro-mechanical-chemical approach: A review. *Earth-Science Reviews*, 185, 1157-1169.

Phillips, S.L., A. Igbene, J.A. Fair, H. Ozbek and M. Tavana. A Technical Databook for Geothermal Energy Utilization, Lawrence Berkeley National Laboratory Report LBL-12810, Berkeley, CA, 46 pp., 1981.

Polak, S., and Grimstad, A. A. 2009. Reservoir simulation study of CO_2 storage and CO_2-EGR in the Atzbach–Schwanenstadt gas field in Austria. *Energy procedia*, **1**(1), 2961-2968.

Pruess, K. 2005. ECO2N: A TOUGH2 fluid property module for mixtures of water, NaCl, and CO_2. eScholarship, University of California.

Pruess, K., and Garcia, J. 2002. Multiphase flow dynamics during CO_2 disposal into saline aquifers. *Environmental Geology*, **42**(2), 282-295.

Pruess, K., and Spycher, N. 2007. ECO2N–A fluid property module for the TOUGH2 code for studies of CO2 storage in saline aquifers. *Energy conversion and management*, **48**(6), 1761-1767.

Pruess, K., Garcia, J., Kovscek, T. et al. 2002. Intercomparison of numerical simulation codes for geologic disposal of CO_2 (No. LBNL-51813). Lawrence Berkeley National Lab.(LBNL), Berkeley, CA (United States).

Pruess, K., Oldenburg, C. M., and Moridis, G. J. 1999. TOUGH2 user's guide version 2 (No. LBNL-43134). Lawrence Berkeley National Lab.(LBNL), Berkeley, CA (United States).

Raad, S. M. J., Lawton, D., Maidment, G. et al. 2021. Transient non-isothermal coupled wellbore-reservoir modeling of CO_2 injection—Application to CO_2 injection tests at the CaMI FRS site, Alberta, Canada. *International Journal of Greenhouse Gas Control*, 111, 103462.

Ranjith, P. G., Perera, M. S. A., and Khan, E. 2013. A study of safe CO_2 storage capacity in saline aquifers: a numerical study. *International Journal of Energy Research*, **37**(3), 189-199.

Rasmusson, K., Tsang, C. F., Tsang, Y. et al. 2015. Distribution of injected CO_2 in a stratified saline reservoir accounting for coupled wellbore-reservoir flow. *Greenhouse Gases: Science and Technology*, **5**(4), 419-436.

Raza, A., and Gholami, R. 2019. Introduction to carbon dioxide capture and storage. In Sustainable Agriculture Reviews **37** (pp. 1-11). Springer, Cham.

Raziperchikolaee, S., and Mishra, S. 2020. Statistical based hydromechanical models to estimate poroelastic effects of CO_2 injection into a closed reservoir. *Greenhouse Gases: Science and Technology*, **10**(1), 176-195.

Rebscher, D., May, F., and Oldenburg, C. M. 2006. Sequestration of CO_2 in the Altmark natural gas field, Germany: Mobility control to extend enhanced gas recovery (No. LBNL-60157). Lawrence Berkeley National Lab.(LBNL), Berkeley, CA (United States).

Rettich, T. R., Handa, Y. P., Battino, R. et al. 1981. Solubility of gases in liquids. 13. High-precision determination of Henry's constants for methane and ethane in liquid water at 275 to 328 K. *The Journal of Physical Chemistry*, **85**(22), 3230-3237

Ritchie, H. "CO_2 emissions dataset: Our sources and methods." 2022

Rutqvist, J., and Tsang, C. F. 2002. A study of caprock hydromechanical changes associated with CO_2-injection into a brine formation. *Environmental Geology*, **42**(2), 296-305.

Rutqvist, J., Birkholzer, J. T., and Tsang, C. F. 2008. Coupled reservoir–geomechanical analysis of the potential for tensile and shear failure associated with CO_2 injection in multilayered

reservoir–caprock systems. *International Journal of Rock Mechanics and Mining Sciences*, **45**(2), 132-143.

Rutqvist, J., Birkholzer, J., Cappa, F. et al. 2007. Estimating maximum sustainable injection pressure during geological sequestration of CO_2 using coupled fluid flow and geomechanical fault-slip analysis. *Energy Conversion and Management*, **48**(6), 1798-1807.

Rutqvist, J., Wu, Y. S., Tsang, C. F. et al. 2002. A modeling approach for analysis of coupled multiphase fluid flow, heat transfer, and deformation in fractured porous rock. *International Journal of Rock Mechanics and Mining Sciences*, **39**(4), 429-442.

Safi, R., Agarwal, R. K., and Banerjee, S. 2016. Numerical simulation and optimization of CO_2 utilization for enhanced oil recovery from depleted reservoirs. *Chemical Engineering Science*, 144, 30-38.

Saripalli, P., and McGrail, P. 2002. Semi-analytical approaches to modeling deep well injection of CO_2 for geological sequestration. *Energy Conversion and Management*, **43**(2), 185-198.

Schlumberger. 2012. ECLIPSE 300 User Manual, Version 2012.1.

Settari, A., and Walters, D. A. 2001. Advances in coupled geomechanical and reservoir modeling with applications to reservoir compaction. *Spe Journal*, **6**(03), 334-342.

Settari, A., Walters, D. A., and Behie, G. A. 1999. Reservoir geomechanics: New approach to reservoir engineering analysis. Presented at Technical Meeting/Petroleum Conference of The South Saskatchewan Section.

Shabani, B., and Vilcáez, J. 2017. Prediction of CO_2-CH_4-H_2S-N_2 gas mixtures solubility in brine using a non-iterative fugacity-activity model relevant to CO_2-MEOR. *Journal of Petroleum Science and Engineering*, 150, 162-179.

Shi, J. Q., and Durucan, S. 2009. A coupled reservoir-geomechanical simulation study of CO_2 storage in a nearly depleted natural gas reservoir. *Energy Procedia*, **1**(1), 3039-3046.

Shi, X., Wang, Z., Liu, B. et al. 2014. Characteristic investigation and control of a modular multilevel converter-based HVDC system under single-line-to-ground fault conditions. *IEEE Transactions on Power Electronics*, **30**(1), 408-421.

Shibue, Y. 2003. Vapor pressures of aqueous NaCl and $CaCl_2$ solutions at elevated temperatures. *Fluid phase equilibria*, **213**(1-2), 39-51.

Shindo, Y., Fujioka, Y., Takeuchi, K. et al. 1995. Kinetics on the dissolution of CO_2 into water from the surface of CO_2 hydrate at high pressure. *International journal of chemical kinetics*, **27**(6), 569-575.

Shukla, R., Ranjith, P., Haque, A. et al. 2010. A review of studies on CO_2 sequestration and caprock integrity. *Fuel*, **89**(10), 2651-2664.

Simo, J. C., and Armero, F. 1992. Geometrically non-linear enhanced strain mixed methods and the method of incompatible modes. *International Journal for Numerical Methods in Engineering*, **33**(7), 1413-1449.

Smith, M. M., Sholokhova, Y., Hao, Y. et al. 2013. Evaporite caprock integrity: An experimental study of reactive mineralogy and pore-scale heterogeneity during brine-CO_2 exposure. *Environmental science and technology*, **47**(1), 262-268.

Søreide, I., and Whitson, C. H. 1992. Peng-Robinson predictions for hydrocarbons, CO_2, N_2, and H_2S with pure water and NaCI brine. *Fluid Phase Equilibria*, 77, 217-240.

Spycher, N., and Pruess, K. 2005. CO_2-H_2O Mixtures in the Geological Sequestration of CO2. II. Partitioning in Chloride Brines at 12–100 C and up to 600 bar. *Geochimica et Cosmochimica Acta*, **69**(13), 3309-3320.

Spycher, N., Pruess, K., and Ennis-King, J. 2003. CO_2-H_2O mixtures in the geological sequestration of CO_2. I. Assessment and calculation of mutual solubilities from 12 to 100 C and up to 600 bar. *Geochimica et cosmochimica acta*, **67**(16), 3015-3031.

Taft Jr, R. W., Purlee, E. L., Riesz, P. et al. 1955. π-Complex and Carbonium Ion Intermediates in Olefin Hydration and E1 Elimination from t-Carbinols. II. Trimethylethylene, Methylenecyclobutane, Triptene and the Effect of Acidity on their Hydration Rate1, 2. *Journal of the American Chemical Society*, **77**(6), 1584-1587.

Taron, J., Elsworth, D., and Min, K. B. 2009. Numerical simulation of thermal-hydrologic-mechanical-chemical processes in deformable, fractured porous media. *International Journal of Rock Mechanics and Mining Sciences*, **46**(5), 842-854.

Terzaghi, K., Peck, R. B., and Mesri, G. 1996. Soil mechanics in engineering practice. John wiley and sons.

Thomas, M. W., Stewart, M., Trotz, M. et al. 2012. Geochemical modeling of CO_2 sequestration in deep, saline, dolomitic-limestone aquifers: Critical evaluation of thermodynamic sub-models. *Chemical Geology*, 306, 29-39.

Tomić, L., Karović-Maričić, V., Danilović, D. et al. 2018. Criteria for CO_2 storage in geological formations. *Podzemni radovi*, (32), 61-74.

Tran, D., Nghiem, L., and Buchanan, L. 2005. Improved iterative coupling of geomechanics with reservoir simulation. Presented at SPE Reservoir Simulation Symposium.

Turta, A. T., Sim, S. S., Singhal, A. K. et al. 2008. Basic investigations on enhanced gas recovery by gas-gas displacement. *Journal of Canadian Petroleum Technology*, ***47***(10).

Underschultz, J., Boreham, C., Dance, T. et al. 2011. CO_2 storage in a depleted gas field: An overview of the CO2CRC Otway Project and initial results. *International Journal of Greenhouse Gas Control*, **5**(4), 922-932.

Van Genuchten, M. T. 1980. A closed-form equation for predicting the hydraulic conductivity of unsaturated soils. *Soil science society of America journal*, ***44***(5), 892-898.

Vilarrasa, V., Bolster, D., Olivella, S. et al. 2010. Coupled hydromechanical modeling of CO_2 sequestration in deep saline aquifers. *International Journal of Greenhouse Gas Control*, **4**(6), 910-919.

Vilarrasa, V., Olivella, S., Carrera, J. et al. 2014. Long term impacts of cold CO_2 injection on the caprock integrity. *International Journal of Greenhouse Gas Control*, 24, 1-13.

Vishal, V., Singh, L., Pradhan, S. P. et al. 2013. Numerical modeling of Gondwana coal seams in India as coalbed methane reservoirs substituted for carbon dioxide sequestration. *Energy*, 49, 384-394.

Voskov, D. V., Henley, H., and Lucia, A. 2017. Fully compositional multi-scale reservoir simulation of various CO_2 sequestration mechanisms. *Computers and Chemical Engineering*, 96, 183-195.

Wang, C., Huang, Z., and Wu, Y. S. 2020. Coupled numerical approach combining X-FEM and the embedded discrete fracture method for the fluid-driven fracture propagation process in porous media. *International Journal of Rock Mechanics and Mining Sciences*, 130, 104315.

Wang, L., Bai, B., Li, X. et al. 2016. An analytical model for assessing stability of pre-existing faults in caprock caused by fluid injection and extraction in a reservoir. *Rock Mechanics and Rock Engineering*, **49**(7), 2845-2863.

Wang, W., Kosakowski, G., and Kolditz, O. 2009. A parallel finite element scheme for thermo-hydro-mechanical (THM) coupled problems in porous media. *Computers and Geosciences*, **35**(8), 1631-1641.

Wang, Y., Li, T., Chen, Y., and Ma, G. 2019. Numerical analysis of heat mining and geological carbon sequestration in supercritical CO_2 circulating enhanced geothermal systems inlayed with complex discrete fracture networks. *Energy*, 173, 92-108.

Webb, S. W., and Pruess, K. 2003. The use of Fick's law for modeling trace gas diffusion in porous media. *Transport in porous media*, **51**(3), 327-341.

Wen, W. Y., and Hung, J. H. 1970. Thermodynamics of hydrocarbon gases in aqueous tetraalkylammonium salt solutions. *The Journal of Physical Chemistry*, **74**(1), 170-180.

White, S. P., Weir, G. J., and Kissling, W. M. 2001. Numerical simulation of CO_2 sequestration in natural CO_2 reservoirs on the Colorado Plateau. Presented at Proceedings of first national conference on carbon sequestration, Washington, DC.

Winterfeld, P. H., and Wu, Y. S. 2012. A novel fully coupled geomechanical model for CO2 sequestration in fractured and porous saline aquifers. Presented at XIX International Conference on Water Resources CMWR (pp. 17-22).

Winterfeld, P. H., and Wu, Y. S. 2013. Users guide for TOUGH2-CSM (TOUGH2-Carbon Sequestration Model)-massively parallel simulation of fully-coupled flow with geomechanics. Energy Modeling Group, Petroleum Engineering Department Colorado School of Mines.

Winterfeld, P. H., and Wu, Y. S. 2016. Simulation of coupled thermal/hydrological/mechanical phenomena in porous media. *Spe Journal*, **21**(03), 1041-1049.

Wishnia, A. 1963. The Hydrophobic Contribution to Micelle Formation: the Solubility of Ethane, Propane, Butane, and Pentane in Sodium Dodecyl Sulfate Solution1. *The Journal of Physical Chemistry*, **67**(10), 2079-2082.

Wu, Z., Zeck, S., and Knapp, H. 1985. Measurements of the Solubility of Carbon Dioxide, Ethylene and Methane in N-Methylpyrrolidone and in its Aqueous Solution. *Berichte der Bunsengesellschaft für physikalische Chemie*, **89**(9), 1009-1013.

Xiao, C., Harris, M. L., Wang, F. et al. 2011. Field Testing and Numerical Simulation of Combined CO2 Enhanced Oil Recovery and Storage in the SACROC Unit. Presented a t Canadian Unconventional Resources Conference.

Xiao, Y., Xu, T., and Pruess, K. 2009. The effects of gas-fluid-rock interactions on CO_2 injection and storage: insights from reactive transport modeling. *Energy Procedia*, **1**(1), 1783-1790.

Xu, T., Apps, J. A., and Pruess, K. 2003. Reactive geochemical transport simulation to study mineral trapping for CO_2 disposal in deep arenaceous formations. *Journal of Geophysical Research: Solid Earth*, **108**(B2).

Xu, T., Apps, J. A., and Pruess, K. 2005. Mineral sequestration of carbon dioxide in a sandstone–shale system. *Chemical geology*, **217**(3-4), 295-318.

Yang, F., Bai, B., Tang, D. et al. 2010. Characteristics of CO_2 sequestration in saline aquifers. Petroleum Science, 7(1), 83-92.

Yin, S., Dusseault, M. B., and Rothenburg, L. 2011. Coupled THMC modeling of CO_2 injection by finite element methods. *Journal of Petroleum Science and Engineering*, **80**(1), 53-60.

Zaydullin, R., Voskov, D. V., James, S. C. et al. 2014. Fully compositional and thermal reservoir simulation. *Computers and Chemical Engineering*, 63, 51-65.

Zerai, B., Saylor, B. Z., and Matisoff, G. 2006. Computer simulation of CO_2 trapped through mineral precipitation in the Rose Run Sandstone, Ohio. *Applied Geochemistry*, **21**(2), 223-240.

Zhang, R. H., Chen, S. N., Hu, S. Y. et al. 2021. Numerical simulation and laboratory experiments of CO_2 sequestration and being as cushion gas in underground natural gas storage reservoirs. *Journal of Natural Gas Science and Engineering*, 85, 103714.

Zhang, R., Winterfeld, P. H., Yin, X. et al. 2015. Sequentially coupled THMC model for CO_2 geological sequestration into a 2D heterogeneous saline aquifer. *Journal of Natural Gas Science and Engineering*, 27, 579-615.

Zhang, Y., Oldenburg, C. M., Finsterle, S. et al. 2007. System-level modeling for economic evaluation of geological CO_2 storage in gas reservoirs. *Energy Conversion and Management*, **48**(6), 1827-1833.

Zheng, L., and Spycher, N. 2018. Modeling the potential impacts of CO_2 sequestration on shallow groundwater: The fate of trace metals and organic compounds before and after leakage stops. *Greenhouse Gases: Science and Technology*, **8**(1), 161-184.

Zheng, L., Apps, J. A., Spycher, N., Birkholzer, J. T. et al. 2012. Geochemical modeling of changes in shallow groundwater chemistry observed during the MSU-ZERT CO_2 injection experiment. *International journal of greenhouse gas control*, 7, 202-217.

Zheng, L., Spycher, N., Birkholzer, J. et al. 2013. On modeling the potential impacts of CO_2 sequestration on shallow groundwater: Transport of organics and co-injected H_2S by

supercritical CO_2 to shallow aquifers. *International Journal of Greenhouse Gas Control*, 14, 113-127.

Zhou, Q., Birkholzer, J. T., Tsang, C. F. et al. 2008. A method for quick assessment of CO_2 storage capacity in closed and semi-closed saline formations. *International Journal of Greenhouse gas control*, **2**(4), 626-639.

Ziabakhshganji, Z., and Kooi, H. 2012. Equation of State for the thermodynamic equilibrium of gas mixtures and brines to allow simulation of the effects of impurities in CO_2 storage. In EGU General Assembly Conference Abstracts (p. 8225).

Zimmerman, R. W. 2000. Coupling in poroelasticity and thermoelasticity. *International Journal of Rock Mechanics and Mining Sciences*, **37**(1-2), 79-87.

Zudkevitch, D., and Joffe, J. 1970. Correlation and prediction of vapor-liquid equilibria with the redlich-kwong equation of state. *AIChE Journal*, **16**(1), 112-119.

Zuloaga-Molero, P., Yu, W., Xu, Y. et al. 2016. Simulation study of CO_2-EOR in tight oil reservoirs with complex fracture geometries. *Scientific reports*, **6**(1), 1-11.